Magnetism, Skyrmions and Magnon-Phonon Coupling in Two-Dimensional Van Der Waals Ferromagnetic Fe_3GeTe_2

Zur Erlangung des Akademischen Grades eines

Doktors der Naturwissenschaften (Dr. rer. nat.)

von der KIT-Fakultät für Physik

des Karlsruher Instituts für Technologie (KIT)

genehmigte

Dissertation

von

M. Sc. Namrata Bansal

aus Indien

Tag der mündlichen Prüfung: 7. Juni 2024

Referent: Prof. Dr. Wulf Wulfhekel

Korreferent: Prof. Dr. Markus Garst

I dedicate this thesis to my loving parents, to my beloved late brother and to my cherished late grandmother (Nani).

Abstract

Fe_3GeTe_2 (FGT) has emerged as a pivotal role among two-dimensional materials, distinguished by its remarkable ferromagnetic characteristics, boasting one of the highest Curie temperatures within the realm of known van der Waals materials, and its potential to host skyrmions. This collaborative experimental and theoretical investigation employs spin-polarized scanning tunneling microscopy in conjunction with atomistic spin-dynamics simulations, incorporating parameters derived from density functional theory calculations. Our study delves into the complexities of magnetic bubble domains and microscopic domain wall profiles, unveiling a subtle magneto-electric effect influencing the domain wall width in response to the electric field within the tunneling junction. Additionally, we pinpoint the critical magnetic field for the collapse of bubble domains. These findings contribute valuable insights into the intricate magnetism exhibited by FGT.

Concurrently, our investigation delves into the dynamic coupling of magnons and phonons in bulk FGT single crystal, using inelastic scanning tunneling spectroscopy (ISTS) facilitated by an ultra-low temperature scanning tunneling microscope. With the help of ISTS, we have shown a strong magnon-phonon coupling, highlighting a strong interaction between magnons and acoustic phonons. This interaction is rooted in avoided level crossings and the hybridization between magnonic and phononic bands in the material. Experimental identification of additional hybridization points is achieved, and their energies are compared with density functional theory calculations. The outcomes of this study not only contribute to the fundamental understanding of FGT's dynamic magnon-phonon coupling but also provide a foundational framework for tailoring such properties in two-dimensional materials.

Contents

Chapter 1

Introduction

In 2004, a seminal breakthrough emerged through the work of Novoselov, Geim and colleagues, unveiling the electric field effect in graphene [1] and setting the stage for a transformative branch in physics. Their exploration of "atomically thin layers of graphite," now recognized as graphene, yielded not only a novel approach to fabrication, ingeniously employing everyday scotch tape, but also illuminated the remarkable properties intrinsic to these materials. This foundational study not only uncovered the unique attributes of graphene [2] but also extended insights into other layered materials [3], revealing phenomena like the massless behavior of electrons in graphene [4] and the thickness-dependent intricacies of the band structure in MoS_2 [5, 6]. The subsequent years witnessed a potential wave of scholarly interest, as evidenced by a prolific surge in papers by 2009 [7]. The pinnacle of this transformative journey was reached in 2010 when A. K. Geim and K. S. Novoselov were honoured with the Nobel Prize in Physics, cementing their pioneering contributions to the isolation and physical exploration of graphene, an atomically thin material exhibiting extension in only two spatial directions [8, 9].

In the wake of the extensive research and exploration surrounding graphene, researchers began exploring other materials that could work together like building blocks in Van der Waals (VdW) heterostructures. This quest led to the exploration of other VdW materials, including hexagonal boron nitride (hBN), an insulator, and molybdenum disulfide (MoS_2), a semiconductor [4]. The discovery of these materials marked the initiation of a new era in physics and applications, unveiling advancements in superconductivity, various many-body phenomena [10–12], a pronounced thickness-dependent behavior in electronic structure [5, 6], and the formation of superlattices through the creation of moiré patterns [13–15]. While opportunities for VdW materials in spintronic applications have been emphasized [16–18], it is noteworthy that magnetic VdW materials

have only recently captured attention [19–22]. This stands in contrast to the extensive research in (opto-)spintronics [23–27] and the widespread use of magnetic materials in everyday devices. The absence of magnetic VdW materials can be attributed, in part, to fundamental limitations in the quest for new, usable VdW materials. Challenges include the decrease in layer thickness leading to reduced melting temperatures, limiting materials retaining their 2D character at room temperature. Additionally, the protective layers naturally formed on most bulk materials, such as oxidation layers, are undesirable for ultra-thin surfaces. Although epitaxial growth methods have been explored, they do not yet match the quality achieved through manual exfoliation using the scotch tape method. Furthermore, the Mermin-Wagner theorem poses a constraint on the spontaneous emergence of ordered magnetic phases in two or fewer dimensions in systems with continuous symmetry, necessitating additional mechanisms, like anisotropy, to break the symmetry and induce an ordered magnetic phase [20]. This thesis delves into these complexities, aiming to unravel the intricacies of magnetic VdW materials and their potential applications.

Subsequently, two-dimensional materials garnered substantial scientific attention, leading to the synthesis of a diverse array of new compounds distinguished by unique chemical and physical properties. Transition-metal dichalcogenides (TMDs) have emerged as particularly intriguing from a physical standpoint, generating significant interest due to their promising applications in semiconductor technologies, such as transistors [28], and battery electrodes [29]. Beyond their electronic properties, TMDs also exhibit noteworthy magnetic characteristics, positioning them as promising candidates for applications in spintronics, magnonics, and magnetic memory devices [30].

To explore the electronic and magnetic properties of materials, scanning tunneling microscopy (STM) proves to be an exceptional method, enabling the atomic resolution of not only topography but also electronic and magnetic structures [31]. Introduced by Binnig and Rohrer in 1981 [32], STM has undergone manifold enhancements over the years. In the investigation of a sample's magnetic properties, spin-polarized scanning tunneling microscopy (SP-STM) has been developed [33]. Utilizing techniques like scanning tunneling spectroscopy (STS) and inelastic scanning tunneling spectroscopy (ISTS), the magnetic domains and quasiparticles, respectively, can be closely scrutinized [34, 35].

This thesis was dedicated to a comprehensive investigation of intrinsic properties within 2D materials, specifically 2D van der Waals ferromagnetic Fe_3GeTe_2 (FGT). The main aim of this work was to investigate the various magnetic properties, magnetic skyrmions, and the magnon-phonon hybridization in this system. The study aimed to elucidate the fundamental magnetic

properties of FGT, including its magnetic ordering, domain structures, and magnetic anisotropy. Furthermore, it sought to uncover the intricate behavior of magnetic skyrmions in FGT, exploring their formation, stability, and manipulation within the material. Additionally, the research delved into the phenomenon of magnon-phonon hybridization in FGT, investigating how the interaction between magnons (quantized spin waves) and phonons (lattice vibrations) influenced the material's magnetic properties.

Through a combination of theoretical modeling, experimental techniques, and advanced characterization methods, this thesis endeavored to provide a comprehensive understanding of the magnetic behavior and phenomena exhibited by 2D van der Waals ferromagnetic materials, with FGT serving as a prominent example. Ultimately, this research contributed to the broader scientific knowledge base, paving the way for advancements in the field of 2D magnetism and its potential applications in future technologies.

The second chapter provides a concise overview of the fundamentals. It introduces the basic principle of the quantum tunneling effect, scanning tunneling microscopy (STM), spin-polarized STM, inelastic excitations, and the concept of 2D materials along with their various types. Additionally, it covers fundamental aspects of skyrmions and delves into the phenomenon of Kondo resonance.

The third chapter provides a concise overview of the experimental facility utilized for this study. It encompasses a detailed description of the ultra-high vacuum (UHV) setup and the refrigeration system employed. Additionally, it outlines the surface cleaning methodology implemented and elucidates the functionality of the magnetic fields utilized in the experiment.

The fourth chapter serves as a gateway to exploring ferromagnetism in 2D van der Waals materials. Our exploration commences with an in-depth investigation of VSe_2, a prominent member of TMDs renowned for its diverse properties. Specifically, our focus is on monolayers (ML) of VSe_2 and their growth on highly oriented pyrolytic graphite (HOPG) substrates (ML VSe_2/HOPG) achieved through the Molecular Beam Epitaxy (MBE) technique. This exploration aims to unravel the intricate interplay of magnetic phenomena within this intriguing material system.

The fifth chapter marks the beginning of a thorough examination of the surface properties of FGT. Our investigation encompasses several key aspects, such as the crystal growth process via the chemical vapor transport (CVT) method, elemental characterization using energy-dispersive X-ray spectroscopy (EDX), and the analysis of magnetic properties utilizing the Quantum Design Magnetic Property Measurement System (QD-MPMS).

In the sixth chapter, we undertake a detailed exploration of FGT properties. Specifically, we delve into topographical analysis using STM and investigate magnetic domains, skyrmions, and related properties using SP-STM equipped with antiferromagnetic tips. By combining SP-STM measurements with density functional theory (DFT) calculations, we aim to elucidate the spin-polarized density of states.

In the seventh chapter, we delve into investigating the dip near the Fermi level observed in DOS spectra. Our main goal is to uncover the underlying cause of this dip, particularly by exploring the potential contribution of inelastic excitations. We focus on examining the coupling between magnons and acoustic phonons in the 2D ferromagnetic van der Waals material FGT.

In the final chapter, we consolidate the key concepts and findings presented in this study. We offer an in-depth summary of the main ideas and results, emphasizing their significance and implications within the broader context of the field. Furthermore, we outline potential directions for future research, suggesting avenues for further exploration and investigation into the studied systems. By doing so, we aim to provide a comprehensive overview of the current state of research and offer valuable insights that can guide future endeavors in this area.

Chapter 2

Theoretical framework

This chapter serves as an introductory exploration into scanning tunneling microscopy (STM) and its associated techniques for sample investigation. We will delve into the core principles of STM theory and provide a comprehensive overview of tunneling magneto resistance (TMR), spin-polarized STM (SP-STM), and inelastic electron tunneling spectroscopy (IETS). Additionally, we will explore the fundamentals of two-dimensional (2D) materials, with a particular focus on transition-metal dichalcogenides (TMDs) and 2D magnetic materials. The discussion will extend to cover the basics of magnetic skyrmions, including their formation, as well as the exploration of quasi-particles such as phonons and magnons, along with their respective couplings.

2.1 Scanning Tunneling Microscopy

The scanning tunneling microscopy (STM) stands as a renowned method for probing surfaces at the nanometer scale [36]. Its exceptional precision hinges on the exponential relationship between the tunneling current and the distance separating two electrodes in vacuum: namely, an atomically sharp tip and a conductive sample under investigation. During its initial stages, tunneling spectroscopy was primarily confined to junctions featuring a thin insulating oxide layer as a barrier. The demonstration of vacuum tunneling between two metal electrodes was achieved by Young et al. (1971) and Teague (1978) [37]. However, it was G. Binnig and H. Rohrer who, in 1982 [38], revolutionized the field by integrating the concept of bringing a metal tip into close proximity with a sample, thereby initiating a tunneling current, with the ability to scan this tip across the sample surface to obtain an atomic-scale image. For their invention of the scanning tunneling microscope Binnig and Rohrer were awarded the Nobel Prize in 1987.

2.1.1 Principle of STM

Conceptually, electron tunneling in the STM can be elucidated by envisioning a plane wave navigating a potential barrier, as depicted in Figure 2.1. Upon encountering the barrier, the wave undergoes partial reflection and partial transmission, with exponential decay occurring within the barrier. The barrier's transmission coefficient, denoted as $T = |D|^2$, is derived from stitching together the wavefunction and its derivatives across different regions of the potential.

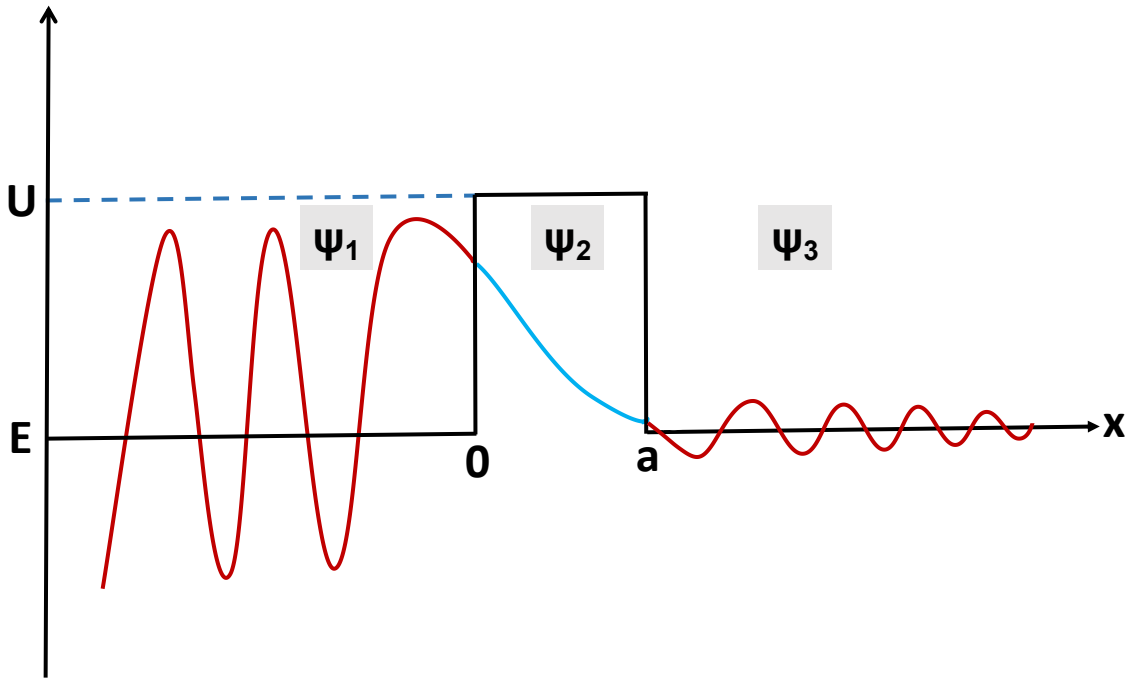

Figure 2.1: Tunneling effect: The electron's wave function ψ_1 is depicted across three regions. In region 1, the wave propagates freely, while in region 2, it exponentially decays. Finally, in region 3, the wave continues to propagate with a non-zero amplitude.

$$\psi_1(x) = Ae^{ikx} + A_0e^{-ikx} \tag{2.1}$$

$$\psi_2(x) = Be^{\kappa x} + B_0e^{-\kappa x} \tag{2.2}$$

$$\psi_3(x) = Ce^{ikx} \tag{2.3}$$

The wave functions ψ_1, ψ_2, and ψ_3 represent the electron's state before, within, and after encountering the potential barrier, respectively. Here, $k = \sqrt{\frac{2mE}{\hbar}}$ and $\kappa = \sqrt{\frac{2m(U-E)}{\hbar}}$. To ensure smooth

transition across the barrier, these functions and their derivatives must maintain continuity at $x = 0$ and $x = a$. The probability of the electron traversing the barrier is determined by the transmission coefficient [39]:

$$T = \frac{|C|^2}{|A|^2} = \frac{4E(U-E)}{4E(U-E) + U^2 \sinh^2(a\kappa)} \tag{2.4}$$

The tunneling current I is directly proportional to the transmission coefficient. In the context of STM, when $e^{\kappa a} \ll 1$, the following simplification arises from the aforementioned equation:

$$I \propto T \approx \frac{16k^2\kappa^2}{(k^2+\kappa^2)^2} e^{-2\kappa a} \tag{2.5}$$

As evident from this equation, the current exhibits exponential decay as the size of the barrier increases. In the scenario of STM, where κ is approximately 1 Å^{-1}, a mere 3 Å increase in barrier width (typical for the difference between two atomic layers) would result in a thousandfold decrease in current.

While the provided model oversimplifies real conditions, it offers insight into how tunneling current can be utilized to precisely probe surface topography with sub-angstrom precision. Despite being a 1D model without consideration of system geometry or electrode band structure, it fails to explain key features of STM. To address this, Bardeen introduced a more refined model in 1961[40]. This model treats the full system Hamiltonian and can be expressed as:

$$H\psi(\mathbf{r},t) = -\frac{\hbar^2}{2m}\Delta\psi(\mathbf{r},t) + V(\mathbf{r})\psi(\mathbf{r},t) \tag{2.6}$$

To simplify the problem, this Hamiltonian can be viewed as two independent Hamiltonians, one for each electrode:

$$H_\alpha = \frac{p^2}{2m} + V_\alpha(\mathbf{r}) \tag{2.7}$$

where α denotes either the tip or the sample. Eigenstates of H_α can then be treated independently, enabling the use of Fermi's golden rule to compute transition probabilities between the tip (μ) and the sample (ν), and vice versa, to calculate the tunneling current I:

$$I = \frac{2\pi e^2}{\hbar} \sum_{\mu,\nu} f(E_\mu)[1 - f(E_\nu + eV)]|M_{\mu,\nu}|^2 \delta(E_\nu - E_F) \tag{2.8}$$

Here, f represents the Fermi distribution, $M_{\mu,\nu} = -\frac{\hbar}{2m}\int(\psi^*_\mu \nabla\psi_\nu - \psi^*_\nu \nabla\psi_\mu)dS$ is the transition matrix element, e is the electron charge, and V is the applied bias voltage. The matrix element can be computed under certain assumptions.

Tersoff and Hamann initially described an approach to the STM geometry, they modeled it with a tip featuring a spherical apex and an s-type wave function decaying exponentially in vacuum [41, 42]. Under small bias and temperature conditions, the equation transforms to:

$$I \propto \int_{E_F}^{E_F+eV} \rho_\mu(E - eV)\rho_\nu(E)T(z, E, eV)dE \tag{2.9}$$

In this context, the current is directly related to the density of states (DOS) of both the tip ρ_μ and the sample ρ_ν, integrated across energy levels. Under the assumption that the tip's DOS remains relatively constant near the Fermi energy, particularly applicable when utilizing a tungsten tip, the resulting current predominantly reflects variations in the sample's DOS. This characteristic enables the exploration of the local density of states (LDOS) in scanning tunneling spectroscopy (STS).

2.1.2 Basics of STM Experimentation

The concept behind STM revolves around employing an extremely sharp metallic tip to explore the surface topography and electronic characteristics of a sample [38, 42]. This tip is delicately positioned near, but not in contact with the surface, as illustrated in Figure 2.2. Initially, in the absence of any external intervention, the tip-sample system remains in thermal equilibrium, resulting in an equal probability of electron tunneling from the tip to the sample and vice versa. Consequently, no detectable current is observed. However, by applying a voltage difference between the electrodes, the chemical potential of one electrode is biased, promoting electron tunneling in a specific direction. This leads to the flow of electrons through the junction, generating what is known as a tunneling current. Notably, this current undergoes significant variations in response to changes in applied bias or tip-surface distance, facilitating precise probing of surface properties.

To delve deeper into surface properties and topography, the fundamental approach of STM, as depicted in Figure 2.2, involves moving the tip parallel to the surface (in the x-y directions) while monitoring variations in the tunneling current. Given the strong dependence of the tunneling current on the tip-surface distance, a feedback loop is employed to sustain a constant current during

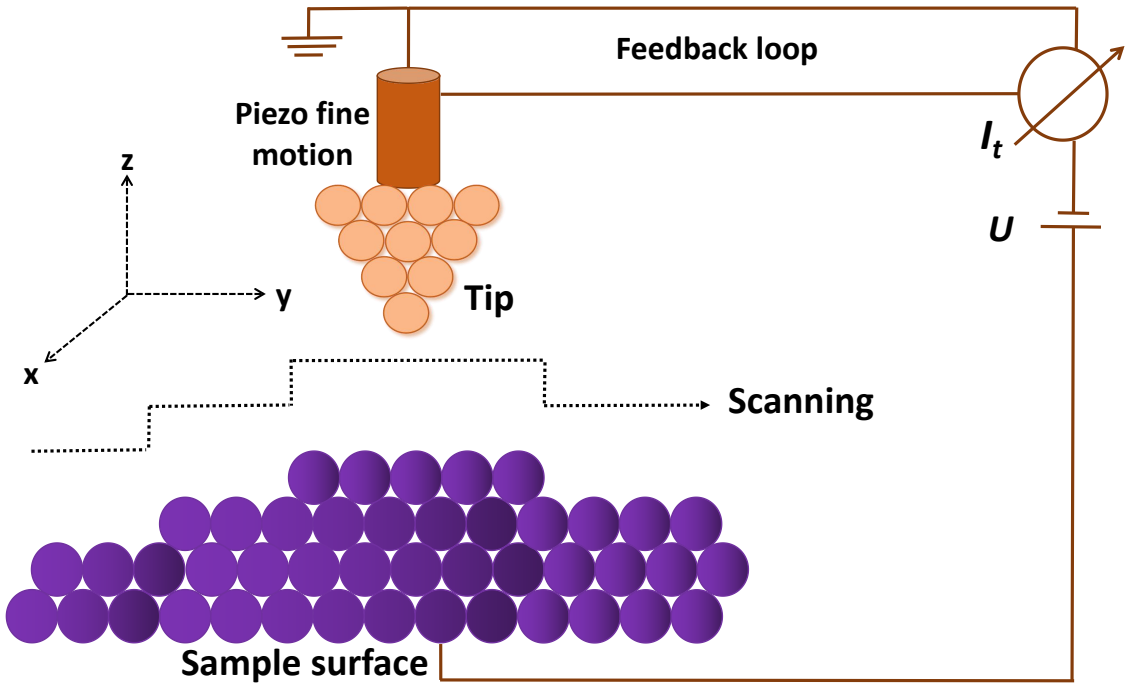

Figure 2.2: Basic principle of STM: A bias voltage U is applied to the sample, facilitating the flow of electrons either from the tip to the sample or vice versa. A feedback loop continuously monitors the difference between the flowing current and the preset current (controlled by software in conjunction with a real-time controller) as the tip moves. It then adjusts the voltage applied to the piezo fine motion to modulate the height of the tip (the trajectory of the tip is indicated by the dashed arrow).

displacement, thereby enabling accurate vertical tip positioning (in the z direction). Throughout this study, unless explicitly stated otherwise, all images were captured using this method. Achieving sub-nanometer precision in displacement necessitates the use of piezoelectric elements to facilitate movement in the x-y-z space. These elements exhibit contraction or extension in specified directions when subjected to voltage [43]. By mounting the tip on a piezoelectric tube and controlling the applied voltage, precise motion of the tip in all three directions can be attained.

2.2 Scanning Tunneling Spectroscopy

Scanning Tunneling Spectroscopy (STS) stands as a pivotal technique within the realm of nanotechnology and condensed matter physics, offering unparalleled insights into the electronic properties of materials at the atomic level. By applying a bias voltage across this gap, an electric field is established, facilitating the tunneling of electrons from the tip to the sample. The fundamental measurement in STS revolves around the detection of the tunneling current between the tip and the sample. This tunneling current is exquisitely sensitive to the local electronic density of states

(DOS) at the surface, providing a window into the electronic structure material.

STS finds broad-ranging applications across diverse disciplines, from materials science to surface physics and nanotechnology. Its versatility has been harnessed for the study of various systems, including semiconductors, metals, insulators, and even individual molecules. Particularly noteworthy is the utility of STS in characterizing novel materials and nanostructures, where conventional techniques may delay due to limitations in resolution or sensitivity.

2.2.1 Differential Conductance Analysis

STS furnishes spectroscopic insights into the energy-dependent DOS of the material under investigation. By modulating the bias voltage applied between the tip and the sample, STS can systematically measure the tunneling current as a function of energy. This feature enables to delve into energy-related phenomena such as band structure, electronic states, and the presence of impurities or defects within the material. When delving into the characteristics of a sample, it is often the Local Density of States (LDOS) that unveils intriguing phenomena. This LDOS is crucial as the tunneling current depends on its integrated value under specific assumptions. To directly investigate the LDOS, one typically examines the derivative of the current with respect to energy:

$$\left.\frac{dI}{dU}\right|_{U=U_0} \propto \rho_{\text{sample}}(U_0) \tag{2.10}$$

However, this method can be limiting, focused, and may yield less-than-ideal signal-to-noise ratios. To overcome these challenges, employing a lock-in amplifier proves beneficial. By introducing a small AC voltage to the applied bias, the tunneling current undergoes fluctuations that are then demodulated at the modulation frequency. This demodulated signal provides a direct measurement of the differential conductance, offering insights into the LDOS. Notably, this technique offers several advantages: it eliminates the need for bias sweeping, enabling focused examination of electronic properties at specific energy levels. Additionally, signal-to-noise ratios often improve with this approach, due to the lock-in amplifier's sensitivity to the modulation frequency. Furthermore, employing this method over multiple periods effectively suppresses much of the white noise in the signal [44].

2.3 Spin Polarized Scanning Tunneling Microscopy

Spin-polarized scanning tunneling microscopy (SP-STM) stands at the forefront of modern nanomagnetism research, offering novel insights into the magnetic properties of surfaces and nanos-

tructures. By combining the principles of STM with spin-polarized detection techniques, SP-STM enables the direct visualization and manipulation of local magnetic moments with exceptional spatial resolution. This helps in unraveling the information of spin textures, magnetic domains, and spin-dependent transport properties at the nanoscale. This powerful technique has revolutionized our understanding of magnetic phenomena, allowing to explore phenomena such as tunneling magnetoresistance (TMR) and tunneling anisotropic magnetoresistance (TAMR) with unparalleled precision, which we discuss below.

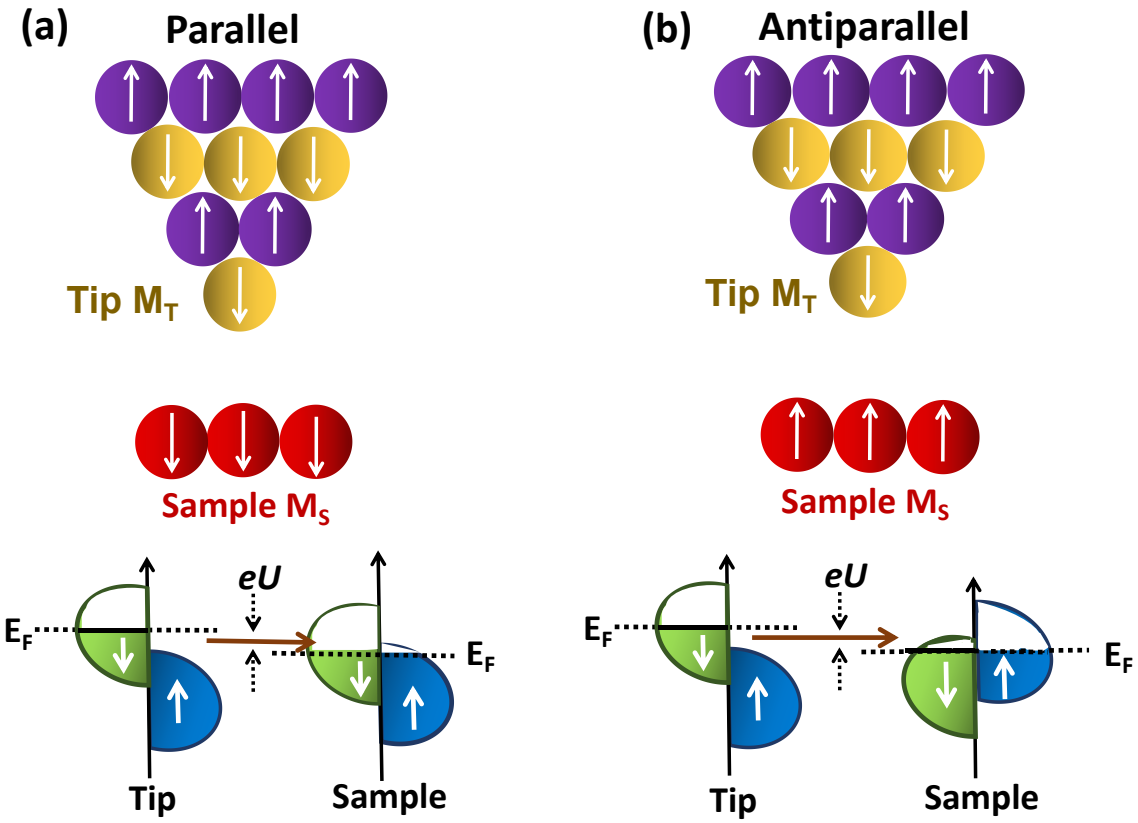

Figure 2.3: Principle of spin-polarized STM: (a) Parallel and (b) anti-parallel spin configurations between the tip and sample, respectively. Spin-polarized tunneling current flows between a magnetic tip and a magnetic sample. The tunneling magnetoresistance (TMR) effect results in higher differential conductance when the spin states are in parallel alignment compared to anti-parallel alignment. Arrows indicate the spin orientations.

2.3.1 Principle of SP-STM

SP-STM serves as a powerful technique for unraveling the intricate spin-dependent electronic properties of materials at the nanoscale. One of its primary functions lies in experienced the degree of spin polarization exhibited by electrons tunneling between STM tip and the sample surface. This characterization of spin polarization is pivotal in understanding the material's

magnetic behavior. The tunneling current was found to be proportional to the LDOS in the vacuum at the corresponding tip position [45].

The model discussed in the above section lacks the capability to estimate the spin polarization of the density of states (DOS), a crucial factor that markedly affects the tunneling current in magnetic tip-sample configurations. When the magnetizations of the tip and sample are aligned, it becomes possible to distinctly separate the spin channels, under the assumption that the electron's spin remains unaltered during tunneling, as illustrated in Figure 2.3. Consequently, in a parallel configuration, spin-up electrons from the tip tunnel into spin-up states of the sample, and vice versa, resulting in expressions like:

$$I_{\uparrow\uparrow} \propto \rho_{\tau}^{\uparrow}\rho_{\sigma}^{\uparrow} + \rho_{\tau}^{\downarrow}\rho_{\sigma}^{\downarrow} \tag{2.11}$$

However, in an antiparallel configuration, this scenario reverses, where spin-up electrons tunnel to spin-down states, yielding:

$$I_{\uparrow\downarrow} \propto \rho_{\tau}^{\uparrow}\rho_{\sigma}^{\downarrow} + \rho_{\tau}^{\uparrow}\rho_{\sigma}^{\downarrow} \tag{2.12}$$

For an arbitrary angle Θ between the magnetizations, spin-up electrons can tunnel into both spin-up and spin-down states with probabilities of $\cos^2(\Theta/2)$ and $\sin^2(\Theta/2)$, respectively. This results in a general formula:

$$I(\Theta) = I_0\left(1 + P_{\tau}P_{\sigma}\cos\Theta\right) \tag{2.13}$$

Here, $P = \frac{\rho^{\uparrow}-\rho^{\downarrow}}{\rho^{\uparrow}+\rho^{\downarrow}}$ defines the spin polarization of the density of states.

2.3.2 Tunneling Magnetoresistance Effect

Exploring the magnetic properties of a sample's surface can be achieved through the utilization of tunneling magnetoresistance (TMR) effect. This technique offer insights into the spatial dependency of magnetic structures, which presenting unique advantages and drawbacks. SP-STM stands as a prominent method for such investigations, capitalizing on the TMR effect [46]. In this mechanism, the conductance at the tunneling junction varies depending on the alignment of magnetic moments beneath the tip, as shown in Figure 2.4. While SP-STM offers direct insight into spin

direction and orientation, its implementation can be challenging and may introduce interactions with the sample due to the magnetic stray field generated by the tip.

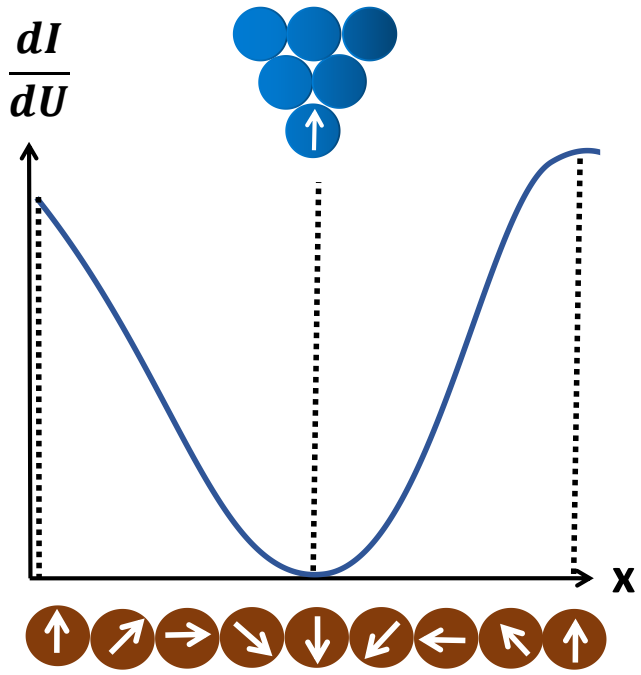

Figure 2.4: TMR effect: (a) Schematic representation of the dI/dU signal acquired through TMR for identical spin textures. Arrows indicate the spin orientations.

2.4 Inelastic Electron Tunneling Spectroscopy

The exploration of inelastic electron tunneling traces back to 1966, when R. C. Jaklevic and J. Lambe [47], pioneered its study by examining planar Al-oxide-Pb junctions. Their use of the second derivative technique revealed minute features in electrical properties, revealing as peaks indicating changes in conductance of about 1% at specific voltages correlated with molecular vibrational frequencies within the barrier. This seminal work led to the identification of these features as outcomes of inelastic electron-molecule interactions during tunneling, giving rise to the term inelastic electron tunneling spectroscopy (IETS or ITS).

Consider E_{in} as the energy required for an inelastic process. When the bias voltage is below $\frac{E_{in}}{e}$ and the temperature is low, all electron tunneling occurs elastically. This is because there are no available empty states at $E_F + eU - E_{in}$ for the scattered electron to occupy. However, once the bias exceeds $\frac{E_{in}}{e}$, a second channel for inelastic tunneling opens up. This leads to the emergence of additional final states and an increase in the overall density of states ($\rho = \rho_{\text{elastic}} + \rho_{\text{inelastic}}$). Consequently, the current-voltage ($I(U)$) curve exhibits a noticeable change, as depicted in Figure 2.5(a). Since the cross-section for inelastic interaction is typically modest, it's often more significant

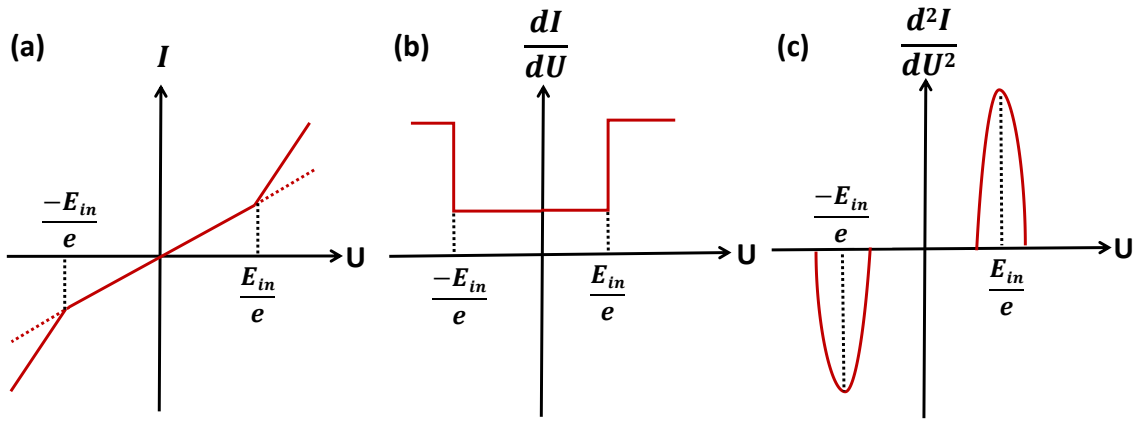

Figure 2.5: Influence of inelastic tunneling on (a) I-U, (b) dI/dU-U, and (c) d^2I/dU^2-U curves: (a) Inelastic tunneling of electrons results in an increase in tunneling current I, leading to a distinct knee in the current curve at a defined bias E$_{in}$, beyond which the slope changes. (b) The effect of inelastic tunneling is evident in the dI/dU-U graph, marked by a sudden increase and decrease at E$_{in}$ and - E$_{in}$ respectively. This elevated dI/dU corresponds to the density of states (DOS) of the inelastic electrons. (c) The d^2I/dU^2-U graph reveals inelastic tunneling as a peak and dip at E$_{in}$ and -E$_{in}$, respectively.

in the first or second derivative of the current with respect to voltage (dI/dU or d^2I/dU^2). In dI/dU, a distinct step appears as shown in Figure 2.5(b), while d^2I/dU^2 shows a peak at $\frac{E_{in}}{e}$ [48] as illustrated in Figure 2.5(c). When the inelastic excitation can occur independently of the tunneling direction, spectral features are observed at both $U = +\frac{E_{in}}{e}$ and $U = -\frac{E_{in}}{e}$, with the inelastic feature at negative bias displaying as a dip. When excitations exhibit a dispersion $\varepsilon(\vec{k})$ and a density of states $\rho_{in}(\varepsilon)$, the scenario becomes more intricate. In such cases, the excitation's cross-section $\Sigma(\varepsilon)$ may also vary with energy. Consequently, the probability $p(\varepsilon)$ of an inelastic process occurring at energy ε, and thus the profile of d^2I/dU^2, can be expressed as:

$$p(\varepsilon) = \rho_{in}(\varepsilon) \cdot \Sigma(\varepsilon) \tag{2.14}$$

If the interaction potential $\phi(\vec{r})$ of the hot electron with the sample or tip is known, the cross-section can be computed using the Born approximation:

$$\Sigma(q) = |\Phi(q)|^2 \tag{2.15}$$

where $\Phi(q)$ represents the Fourier transform of $\phi(\vec{r})$. Translating this into energy space yields:

$$p(\varepsilon) = \rho_{in}(\varepsilon) \cdot |\Phi(q(\varepsilon))|^2 \tag{2.16}$$

One can utilize this approach to study various excitations within the sample, encompassing phonons [49, 50], plasmons [50], and magnons [51]. However, discerning between different types of excitations presents a challenge, as the resulting spectral features tend to be nearly independent of the specific excitation. One potential method involves analyzing the range of excitation energies, which can vary significantly across different excitation types. Another criterion involves examining the cross-section of the excitation process, as the proportion of the inelastic contribution is readily observable in the dI/dU, characterized by the relationship between the step height $\rho_{\text{inelastic}}$ and the total DOS. Over time, this spectroscopic capability found extensive application, becoming a staple in the realm of STM. Its versatility spans from vibrational spectroscopy of single molecules on surfaces [52] to probing magnetic excitations of individual atoms or clusters [53–55]. While studies on collective phenomena like spin waves (magnons) [56, 57] and phonons [50] in graphite and exploration of phonons in superconducting materials [58] are documented. The fundamental principle of IETS, illustrated in Figure 2.5, delineates the intricate interplay between electron tunneling and sample excitations. By analyzing the second derivative of tunneling current with respect to voltage, characteristic peaks emerge, delineating the energies of excitations [59]. The distinctive dip-peak pair, symmetrically flanking U = 0, stands as a symbol of inelastic tunneling processes, underscoring the method's effectiveness in unraveling material intricacies.

2.4.1 Phonon Excitation by IETS

Phonons are quanta of vibrational energy in a crystal lattice, representing the collective motion of atoms. These vibrational modes play a crucial role in determining various properties of materials, such as thermal conductivity, electrical conductivity, and mechanical properties. When an electron interacts with these lattice vibrations, it can exchange energy with the phonon, resulting in a change in the electron's energy level. This interaction between electrons and phonons is known as electron-phonon interaction.

Electron-Phonon Interaction

IETS is used to study electron-phonon interactions at the nanoscale. In this method, when an electron tunnels between the tip and the sample, it can exchange energy with the phonons in the sample, leading to inelastic scattering. This results in a change in the tunneling current, which can be measured as a function of voltage. By analyzing the changes in the tunneling current

with respect to voltage, characteristic peaks emerge in the IETS spectrum, corresponding to the energies of the phonons involved in the electron-phonon interaction. These peaks provide valuable information about the vibrational properties of the material, such as the frequencies and strengths of the phonon modes. Additionally, the shape and intensity of these peaks can reveal details about the electron-phonon coupling strength and the electronic structure of the material.

2.4.2 Magnon Excitation by IETS

Magnons are quasiparticles representing collective excitations of spins in a magnetic material. In a magnetically ordered system, neighboring magnetic moments interact with each other through exchange interactions, causing them to precess collectively around their equilibrium orientations. These collective oscillations of spins, analogous to phonons in crystal lattices, are called magnons [60]. Magnons play a crucial role in determining various magnetic properties of materials, such as magnetic ordering, magnetic phase transitions, and magnetic excitations.

Selection Rules for Magnon

These quasiparticles are distinguished by their energy and wavevector, possessing a spin of -$\hbar$, signifying that the creation of a magnon reduces the total spin by 1$\hbar$. To begin our exploration, we delve into the identification of hot electrons capable of inducing magnons through the application of quantum mechanical selection rules for magnon creation. Our focus centers on a solitary ferromagnetic electrode subjected to a tunneling current from a nonmagnetic counterpart, providing clarity to our discussion. Moreover, we assume a minimal spin-orbit interaction within the ferromagnet, ensuring the preservation of total spin. Finally, we posit that the magnetization of the ferromagnet predominantly stems from the spin moments of electrons within its Fermi sea, a pragmatic assumption particularly relevant to the itinerant ferromagnets under scrutiny in this context.

Firstly, we delve into the identification of hot electrons capable of inelastically generating magnons by applying quantum mechanical selection rules for magnon creation. When a positive sample bias U is imposed on the ferromagnetic electrode, electrons tunnel into the ferromagnet, elevating them to hot electron states above the Fermi level E_F (refer to Figure 2.6(a)). These hot electrons undergo thermalization within the electrode, typically through interactions with lattice defects, phonons, or other electrons. If these processes preserve the spin of the hot electron, no angular momentum transfer occurs between the current and the magnetization, and no inelastic spin transfer torque (STT) is generated. However, if a minority hot electron experiences a spin-flip scattering

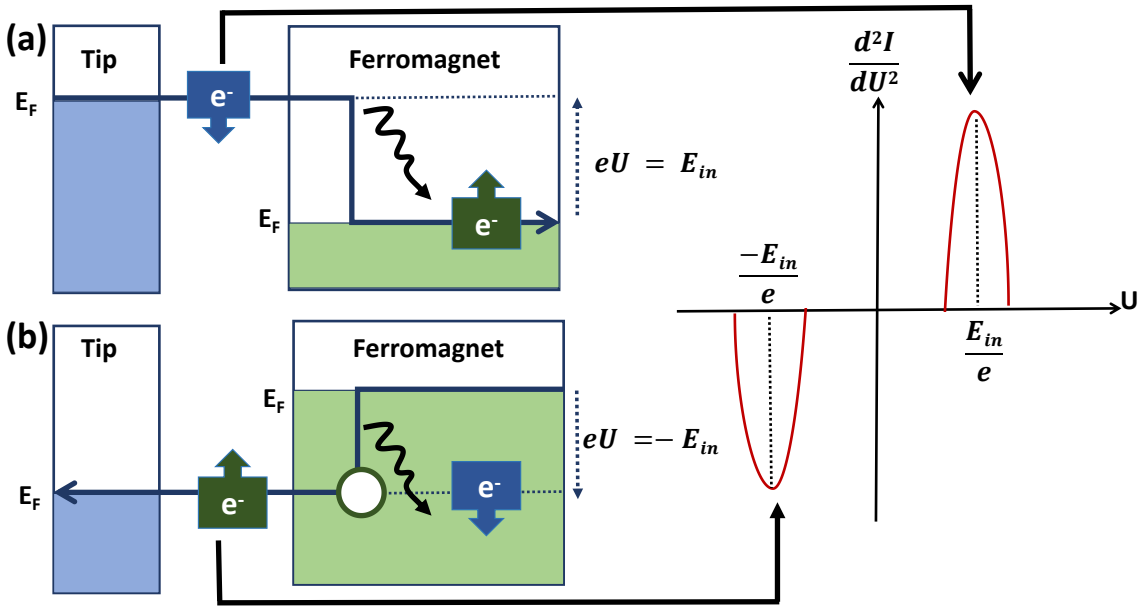

Figure 2.6: Magnon creation process illustrated for tunneling: (a) influx into, and (b) efflux out of a ferromagnetic electrode (on the right). The neighboring electrode (on the left) remains nonmagnetic. Within the ferromagnet, magnons are generated by minority electrons tunneling in, while majority electrons tunnel out.

event with an electron from the Fermi sea, angular momentum is exchanged between the current and the magnetization. This conservation of total spin manifests as a spin increase of 1 $\hbar$ in the current and a corresponding decrease of 1 $\hbar$ in the Fermi sea of the magnet, effectively creating a magnon (Figure2.6(a)). Consequently, the spins of individual ferromagnet particles deviate transversely from their ground-state orientation and precess around the local effective field, akin to the effect observed with a negative damping term in Slonczewski's model. Conversely, the spin flip of a majority current electron to a minority electron corresponds to either magnon annihilation or increased damping of precession according to Slonczewski's depiction. Notably, in our investigation, magnons can only be generated by minority electrons tunneling into the ferromagnet for positive U. Conversely, for negative U, electrons tunnel out of the ferromagnet, creating holes. Conservation of total spin dictates that only majority electrons tunneling out of the ferromagnet can induce magnons and drive magnetization precession. These tunneling events leave behind majority holes, which can be filled by minority electrons from the electron sea through spin flips. This process, known as the filling of minority holes with majority electrons, is tantamount to magnon annihilation. In essence, for negative U, magnons arise exclusively from majority electrons tunneling out of the ferromagnet (see Figure2.6(b)). This momentum transfer between the current and the magnetization constitutes the essence of inelastic STT.

Spin-Magnon Coupling

Strong spin-magnon coupling refers to the interaction between the spins of electrons and the collective excitations of spins (magnons) in a magnetic material. When an electron tunnels between the tip and the sample in a magnetic junction, it can exchange energy and angular momentum with the magnons in the sample. This interaction results in inelastic scattering of the tunneling electron, leading to changes in the tunneling current.

IETS can be used to study spin-magnon coupling at the nanoscale. In IETS, when an electron tunnels between the tip and the sample, it can exchange energy and angular momentum with the magnons in the sample, leading to inelastic scattering. By measuring the changes in the tunneling current as a function of voltage, characteristic peaks emerge in the IETS spectrum, corresponding to the energies of the magnons involved in the electron-magnon interaction. These peaks provide valuable information about the magnetic properties of the material, such as the magnon dispersion relation, the strength of the spin-magnon coupling, and the magnetic ordering of the material.

2.5 Two dimensional (2D) materials

In recent years, the exploration of two-dimensional (2D) van der Waals (vdW) materials has become increasingly prominent, driven by their unique electronic structures and the opportunity they present for constructing complex stacks through exfoliation. The realm of 2D materials [4] has seen a remarkable expansion since the groundbreaking isolation of graphene [1]. With each new addition to this family, anticipation and intrigue mount, fueled by the distinct properties these materials exhibit compared to their three-dimensional counterparts.

A particularly exciting development has been the discovery of 2D magnetism in vdW materials containing $3d$ transition-metal atoms, which has expanded the potential applications of vdW materials in spintronics [62–64]. Depending on the specific metal ions and stacking configurations, these materials exhibit a range of intra- and interlayer magnetic interactions, including ferromagnetic, antiferromagnetic, or frustrated interactions, alongside metallic or insulating band structures. This versatility opens up routes for spin injection and detection, electrical manipulation of magnetism, spin-orbit driven magnetic topology, and novel fields such as spin-valleytronics [64]. This study delves deeply into the intricate physics exhibited by 2D materials, aiming to elucidate their potential properties. Our discussion primarily centers around two key classes: transition metal dichalcogenides (TMDs) and 2D magnetic materials, which will be explored in detail in the upcoming session.

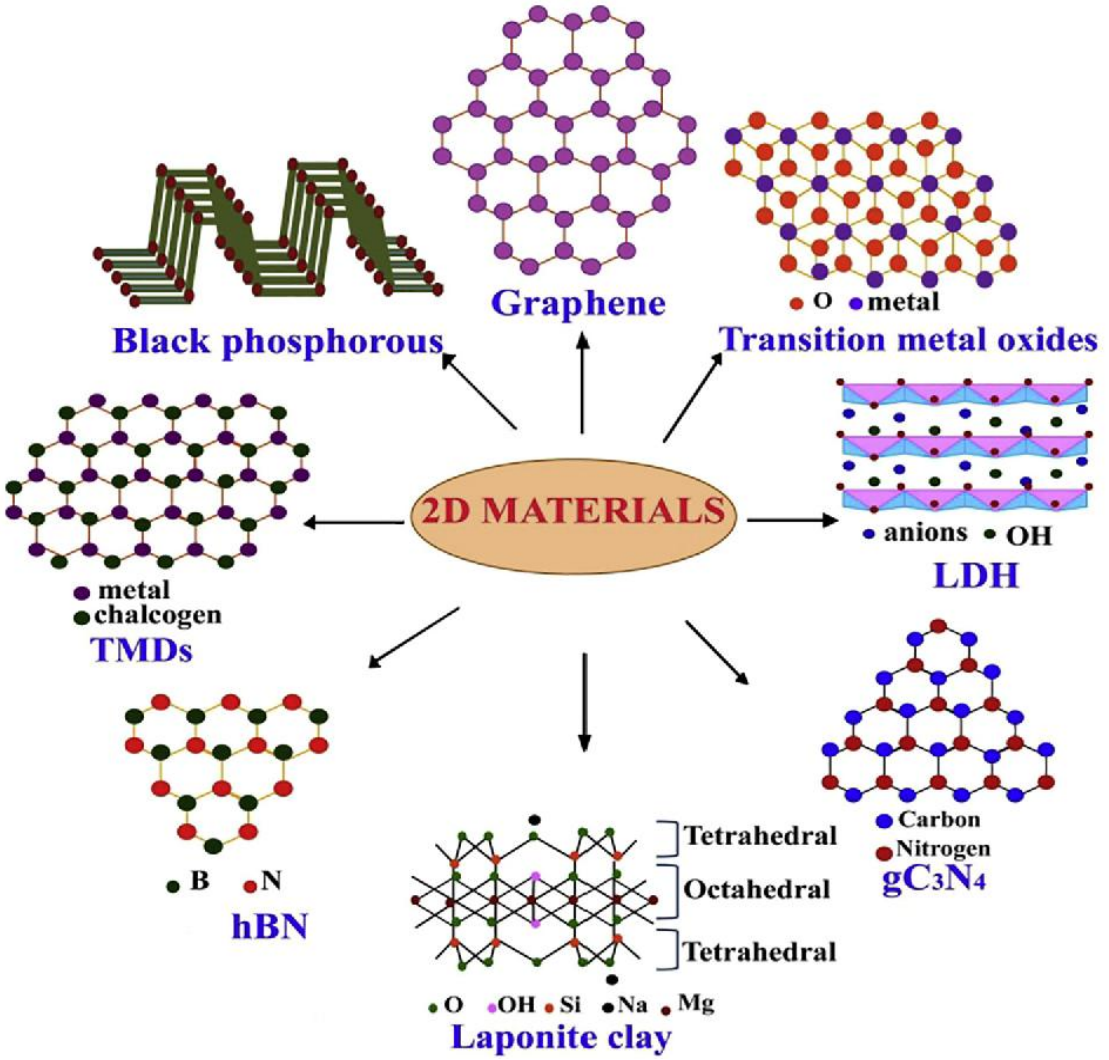

Figure 2.7: Structural representation of various 2D materials: graphene, transition metal dichalcogenides, layered double hydroxides, gC_3N_4, laponite clay, hBN, transition metal dichalcogenides, and black phosphorous, adapted from [61].

2.5.1 Transition-Metal Dichalcogenides

Transition metal dichalcogenides (TMDCs / TMDs), characterized by the formula MX_2 where M represents a transition metal and X denotes a chalcogen, encompass a diverse array of electronic properties. These properties span the spectrum from insulating or semiconducting, exemplified by Ti, Hf, Zr, Mo, and W dichalcogenides, to metallic or semimetallic, as observed in V, Nb, and Ta dichalcogenides. This wide range of electronic behavior arises from the gradual filling of the nonbonding *d* bands by the electrons of the transition metal.

TMDs boast a rich and extensive history, date back to Linus Pauling's determination of their structure in 1923 [65]. By the late 1960s, approximately 60 TMDCs were identified, with around

40 exhibiting a layered structure [66]. The utilization of adhesive tapes to produce ultrathin MoS_2 layers, pioneered by Robert Frindt in 1963, marked an important milestone [67]. Subsequently, in 1986, the first successful production of monolayer MoS_2 suspensions was achieved [68].

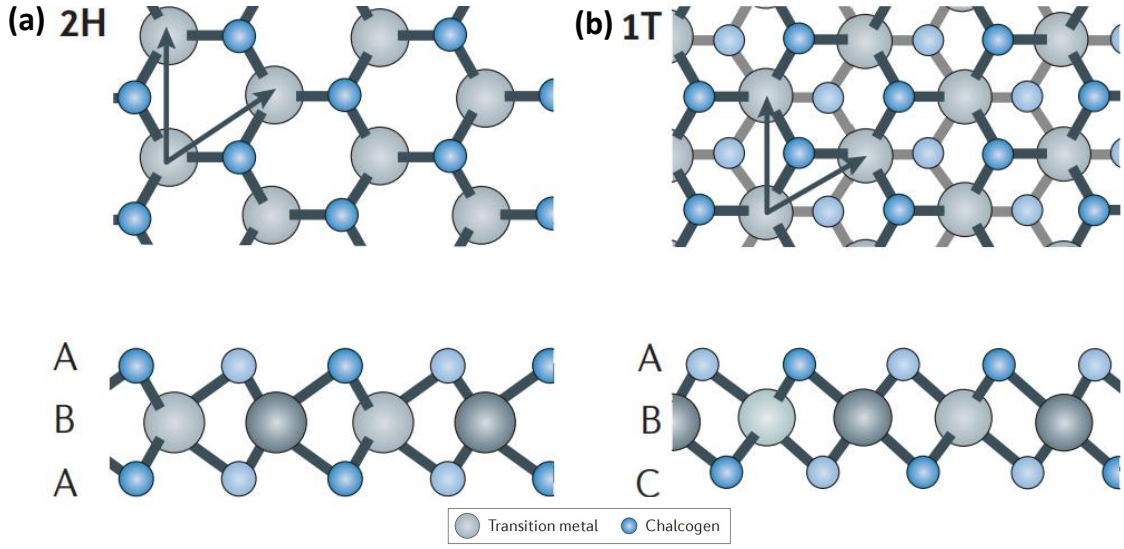

Figure 2.8: Atomic arrangement of single layers of transition metal dichalcogenides (TMDCs) in their (a) trigonal prismatic (2H) and (b) distorted octahedral (1T) phases, figure adapted from [18]

The exponential growth of graphene-related research in 2004 catalyzed the development of techniques tailored for working with layered materials, thereby facilitating renewed investigations into TMDs, particularly their ultrathin films. TMDs exhibit various structural phases, primarily characterized by either trigonal prismatic (2H) or octahedral (1T) coordination of metal atoms, as illustrated in Figure 2.8. These structural phases also evident in different stacking orders of the atomic planes forming the layers. The thermodynamic stability of the 2H or 1T phase depends on the specific combination of transition metal and chalcogen elements. While the 2H phase is typically thermodynamically stable for many TMDs, the 1T phase can often be obtained as a metastable phase.

All TMDs share a common hexagonal crystal structure, where each monolayer consists of three stacked layers arranged as X-M-X. The two predominant polytypes observed in TMDC monolayers are trigonal prismatic, exemplified by materials like MoS_2, VSe_2 and WS_2, and octahedral, represented by TiS_2. These terms describe the coordination environment around the transition metal atom within the monolayer. In the trigonal prismatic polytype, inversion symmetry is broken, resulting in unique properties such as piezoelectricity. This symmetry breaking has significant implications for the electronic structure of the material, influencing its behavior in electronic devices and applications.

Understanding the structural trace of TMDs is crucial for elucidating their electronic, optical, and mechanical properties and for harnessing their potential in various technological applications, ranging from nanoelectronics to energy storage and conversion. Continued research into these materials promises to unveil new insights and opportunities for innovation in the field of materials science and engineering.

2.5.2 Two Dimensional Magnetic Materials

The exploration of magnetism in two dimensions has been a focal point of extensive theoretical [69–74], experimental [75], and technological endeavors, driving advancements in fields such as topology, phase generation driven by fluctuations, and electrical manipulation and detection of spin. A particularly promising avenue within 2D magnetism lies in the rapid fabrication of diverse 2D heterostructures, engineered with tailored levels of strain, chemistry, optical, and electrical properties [12, 76–78]. Much like the transformative impact of graphene and TMDs on condensed matter and materials engineering, the emergence of a new class of 2D atomic crystals known as magnetic vdW materials is anticipated to guide in a multitude of opportunities for both applications and fundamental research. These materials offer a fresh perspective for studying 2D magnetism, where spin fluctuations are anticipated to be significantly enhanced.

The inherent flexibility of 2D atomic crystals, featuring varied elements and structures, presents an avenue for straightforward tuning of magnetic anisotropy. This tunability is crucial for modulating spin fluctuations and thereby controlling various forms of order. The field of magnetic 2D atomic crystals is progressing swiftly, with numerous instances of novel systems showcasing 2D magnetism realized through techniques as simple as adhesive tape, chemical vapor deposition, or molecular beam epitaxy, related to the pioneering methods employed in the fabrication of graphene.

In recent years, several noteworthy examples of magnetic order have emerged within single atomic layers of materials such as $FePS_3$, CrI_3, $Cr_2Ge_2Te_6$, VSe_2, and $MnSe_2$, underscoring the emergent exploration and discovery within the realm of magnetic 2D atomic crystals. Van der Waals (vdW) magnetic materials have assembled increasing attention due to their special two-dimensional ferromagnetic properties, offering exciting prospects for practical spintronic applications [79–88].

The recent surge in the exploration of two-dimensional (2D) van der Waal (vdW) magnets has extended the realms of magnonics and spintronics into the 2D domain [19, 89–97]. In these materials, the elementary bosonic excitations, including magnons and phonons, inherit the strong symmetry breaking characteristic of 2D materials, such as anisotropic dispersion [98–102] and chirality [103, 104]. The magnetic properties of 2D materials, particularly in magnetic 2D materi-

als, are highly sensitive to strain engineering [105–110] due to the large uniaxial anisotropy and the local interactions of magnetic moments with the crystal field. This sensitivity potentially results in a remarkably high dynamic coupling between magnetic and lattice degrees of freedom in two dimensions, significantly impacting the dynamical properties of 2D magnets. Despite the significant potential, little is currently known about the nature and properties of elementary magnetic and lattice excitations in 2D magnetic materials, necessitating exploration using various techniques.

2.6 Magnetic Skyrmions

In 1962, Tony Skyrme introduced Skyrmions as quasi-particles within the realm of particle physics [111]. In the domain of solid-state physics, magnetic skyrmions represent the condensed matter counterpart of these quasi-particles [112]. They are two-dimensional entities formed by projecting a 'hairy ball,' where the 'hair' denote specific spin orientations-resembling a hedgehog or a combed hedgehog configured sphere-onto a plane. The topological charge of a given spin configuration on the plane, also referred to as the winding number, is determined by [113, 114].

$$S = \frac{1}{4\pi} \iint \mathbf{m} \left(\frac{\partial \mathbf{m}}{\partial x} \times \frac{\partial \mathbf{m}}{\partial y} \right) d^2 r \tag{2.17}$$

For a simple skyrmion, the winding number is $n = 1$ as shown in Fig 2.9, but skyrmions with higher winding numbers are also possible. Given that magnetic skyrmions exist as planar entities, they can be observed utilizing STM techniques. However, due to their magnetic nature, it is necessary to employ techniques like TMR or TAMR for imaging.

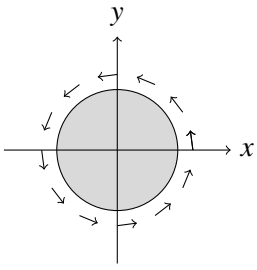

Figure 2.9: Skyrmion with winding number 1

Magnetic skyrmions emerge as distinct, localized entities within magnetic materials, boasting topological protection. These formations adopt a unique configuration wherein the magnetization field encircles a central core, creating a vortex-like structure. This particular arrangement prevents any continuous transformation into a simpler, uniformly magnetized ferromagnetic state [115–117]. The stability of skyrmions stems from the peculiar rotation of magnetization, driven by the

chiral Dzyaloshinskii-Moriya interaction (DMI). This interaction reveals in materials with broken structural inversion symmetry and spin-orbit coupling [118].

Two distinct types of skyrmions are schematically depicted in the Figure 2.10. The first category consists of Bloch-type skyrmions found in chiral magnets, where the spins lie within the tangential plane, as illustrated in Figure 2.10(a). Conversely, the second class comprises Néel-type skyrmions observed in polar magnets, with spins lying within a radial plane, as shown in Figure 2.10(b).

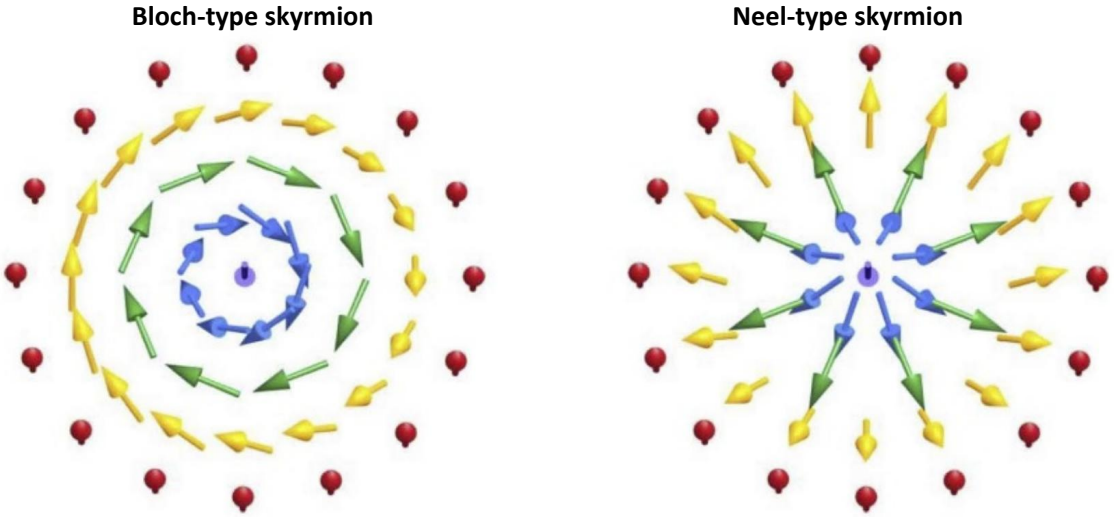

Figure 2.10: Diagram illustrating different types of skyrmions: (a) Bloch-type skyrmion (on left), with spins lying predominantly within the tangential plane, and (b) Néel-type skyrmion (on right), with spins primarily oriented within a radial plane, figure adapted from [119]

In essence, skyrmions represent a captivating frontier in magnetic research, promising advancements in next-generation information storage and processing technologies. Their topological resilience and potential as efficient information carriers underscore their significance in propelling the field of spintronics forward [114, 120–125].

2.7 Kondo Resonance

The Kondo resonance [126] refers to a phenomenon observed in systems with magnetic impurities, particularly in metals, where the electronic density of states exhibits a sharp peak at the Fermi level. This peak arises due to the interaction between the spins of the magnetic impurities and the conduction electrons in the material. In the absence of magnetic impurities, the density of states near the Fermi level typically follows a smooth, continuous distribution. However, when magnetic impurities are introduced into the system, the spins of the impurities interact with the spins of the conduction electrons. This interaction can lead to the formation of a many-body bound state

known as a Kondo state. The Kondo state is characterized by a resonance peak in the density of states at the Fermi level. This peak arises due to the hybridization of the impurity spin states with the conduction electron states near the Fermi level. As a result, electrons with energies close to the Fermi level are strongly scattered by the impurities, leading to the formation of the resonance peak. Kondo resonance plays a crucial role in various physical phenomena, including the Kondo effect, which is characterized by an increase in electrical resistance at low temperatures due to the formation of Kondo states. Additionally, Kondo resonance has important implications for the electronic and magnetic properties of materials, as well as for applications in spintronics and quantum information processing.

Chapter 3

Experimental Setup and Methods

In this chapter, we delve into the experimental setup utilized for our study. We'll provide a comprehensive overview of the measurement facility, offering insights into the system layout and detailing the preparation methods employed. Our STM measurements were conducted within the controlled confines of an ultra-high vacuum (UHV) environment, maintaining a pressure of approximately 1×10^{-10} mbar. We operated two distinct setups: one operated at 700 mK based on the Joule-Thomson (JT) principle, while the other functioned at 40 mK utilizing a dilution refrigerator. Hence, we will briefly explore the operational principles underlying Joule-Thomson and dilution refrigerators to shed light on the underlying principles that shaped our experimental approach.

3.1 Ultra High Vacuum System

This chapter delineates the ultra-high vacuum (UHV) system utilized in our experiments, consisting of three distinct chambers: a load-lock, a preparation chamber, and an STM chamber, each isolated by gate valves. These chambers facilitate sample transfer, preparation, and measurement without altering pressure conditions in adjacent areas. The load-lock chamber maintains a base pressure of P = 4.0×10^{-8} mbar, serving solely for sample transfer, while both the preparation and STM chambers sustain a base pressure of P = 1.0×10^{-10} mbar, crucial for surface studies to minimize contamination. Within the STM chamber, UHV conditions allow effective thermal decoupling of the cryostat, enabling sample cooling to sub-kelvin temperatures. Manipulators enable *in-situ* sample manipulation, preserving sample integrity throughout experiments. Turbo molecular pumps (TMPs) maintain UHV conditions in each chamber, with an ion-getter pump in the preparation and STM chambers for inactive TMPs. The preparation chamber also features

a titanium sublimation pump for enhanced low-pressure conditions, while the STM chamber incorporates a passive sorption pump (SAES pump). Various devices in the preparation chamber facilitate diverse sample preparation techniques, including an ion gun for gas introduction, a coupled low-energy electron diffraction (LEED) and Auger electron spectroscopy (AES) unit for preliminary analyses, and a quadrupole mass spectrometer for gas purity monitoring. The manipulator in the preparation chamber features a replaceable filament for sample heating, with provisions for active cooling. Evaporators in both the preparation and STM chambers enable material deposition, with a four-pockets evaporator in the STM chamber allowing precise single-atom deposition onto cold surfaces.

3.2 Low Temperature Setup

3.2.1 Cryostat Setup

The cryostat system comprises three integral components designed to insulate the STM from external influences and facilitate cooling to cryogenic temperatures.

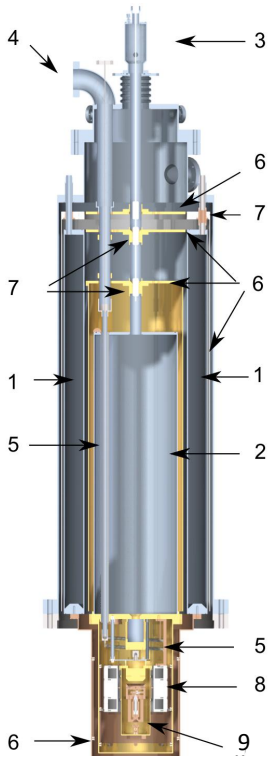

Figure 3.1: Diagram illustrating the components of the cryostat. (1) Liquid nitrogen tank, (2) Liquid helium tank, (3) Inlet and outlet of liquid helium, (4) Inlet and outlet of ^{3}He, (5) Countercurrent heat exchanger for ^{3}He, (6) Radiation shield, (7) Heat exchangers connected with cryogenic gas, (8) Superconducting coil, (9) Microscope head. Figure adapted from [127].

Illustrated in Figure 3.1, these components include the liquid nitrogen (LN_2) tank, the liquid helium (LHe) tank, and a series of thermal shields. The LN_2 tank, positioned at the outermost layer of the cryostat, serves multiple functions. Not only does it store LN_2 for approximately 60 hours, but it also acts as a pre-cooling mechanism for various system components and the dilution stage. Additionally, it offers protection against thermal radiation for the LHe tank, enhancing overall system efficiency.

Beneath the LN_2 tank lies the LHe tank, housed within a thermal shield maintained at 77 K. The LHe tank serves as the primary cooling source for the JT-STM as well as for dilution STM system, delivering the necessary cooling power. Furthermore, it is connected to a radiation shield, providing an additional layer of protection for both the dilution system and the STM body against thermal radiation.

3.2.2 Joule-Thomson STM

The JT-STM setup (as shown in Figure 3.2) achieves a base temperature below 800 mK through the utilization of a Joule-Thomson stage. This system is integrated within a liquid helium bath cryostat, augmented by a surrounding tank containing liquid nitrogen. The presence of liquid nitrogen extends the helium's standing time to over one week, ensuring sustained low temperatures.

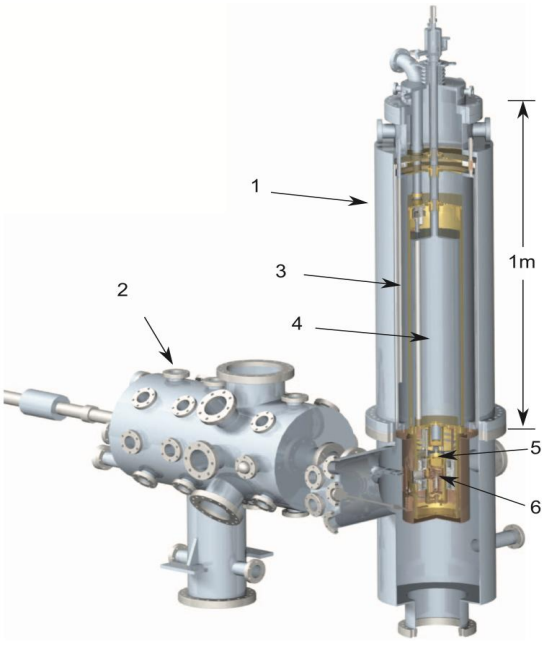

Figure 3.2: Layout of the Joule-Thomson STM machine featuring (1) the cryostat chamber, (2) the preparation chamber, (3) liquid nitrogen bath cryostat, (4) liquid helium bath cryostat, (5) Joule-Thomson cryostat, and (6) microscope head. Figure reference [127].

To maintain atmosphere below 4 K, the cryostat incorporates a reservoir with a capacity of 10 ml, which is connected to a closed cycle facilitating the circulation of ^{3}He. A thin capillary, with an inner diameter of 90 μm, separates the high-pressure side from the low-pressure side just before the reservoir [127]. Within the reservoir, the mixture condenses as a liquid, resulting in a reduction of vapor pressure to below 1 mbar and a corresponding boiling temperature of approximately 800 mK [128]. Directly connected to this reservoir pot, the STM body is thermally anchored to ensure precise temperature control. Temperature regulation is achieved by monitoring the resistance of a commercial ceramic zirconium oxynitride (CERNOX) temperature sensor, strategically positioned at the STM body [128]. However, one significant challenge in low-temperature STM experiments is the time required for the sample to reach the equilibrium base temperature, which can take several hours. Furthermore, the thermal contraction experienced during the cool-down phase induces strong thermal drift, limiting the feasibility of STM measurements until equilibrium is attained.

3.2.3 Dilution STM

To achieve ultra-low temperatures necessary for our experiments, we employ a BlueFors dilution refrigerator. This sophisticated device enables us to cool the sample down to 30 mK [128–130], crucial for enhancing the energy resolution of tunneling spectroscopy and investigating superconducting samples with low transition temperatures (T_c).

Figure 3.3 provide a schematic view of the dilution refrigerator of the ^{3}He / ^{4}He mixture, respectively, offering insight into its operational principles. The working principle begins with a mixture of ^{3}He / ^{4}He gases stored in a tank outside the STM room. By controlling pneumatic valves, we regulate the flow of this mixture into the system. Initially, the mixture undergoes precooling through heat exchange with the LN_2 tank, the LHe tank, and the still, the outlet portion of the cooling system. At the JT expansion stage, the inlet pressure is reduced to approximately 2 bar, causing the mixture to condense and further cool down.

As more mixture condenses, it fills the still, which can be pumped. By continuously pumping the still and allowing for mixture evaporation, the temperature can be lowered to around 800 mK, while the pumped mixture is recirculated in the line. In the temperature range of 2.17 K > T > 870 mK, a phase transition occurs where ^{4}He becomes superfluid and forms a mixture with ^{3}He, which remains in a Fermi liquid state. Subsequently, when the temperature drops below 870 mK, another phase transition occurs, resulting in phase separation.

During phase separation, the ^{3}He-rich phase (concentrated phase) and the ^{4}He-rich phase (diluted phase) form distinct layers, with the ^{3}He-rich phase positioned above the ^{4}He-rich phase. By

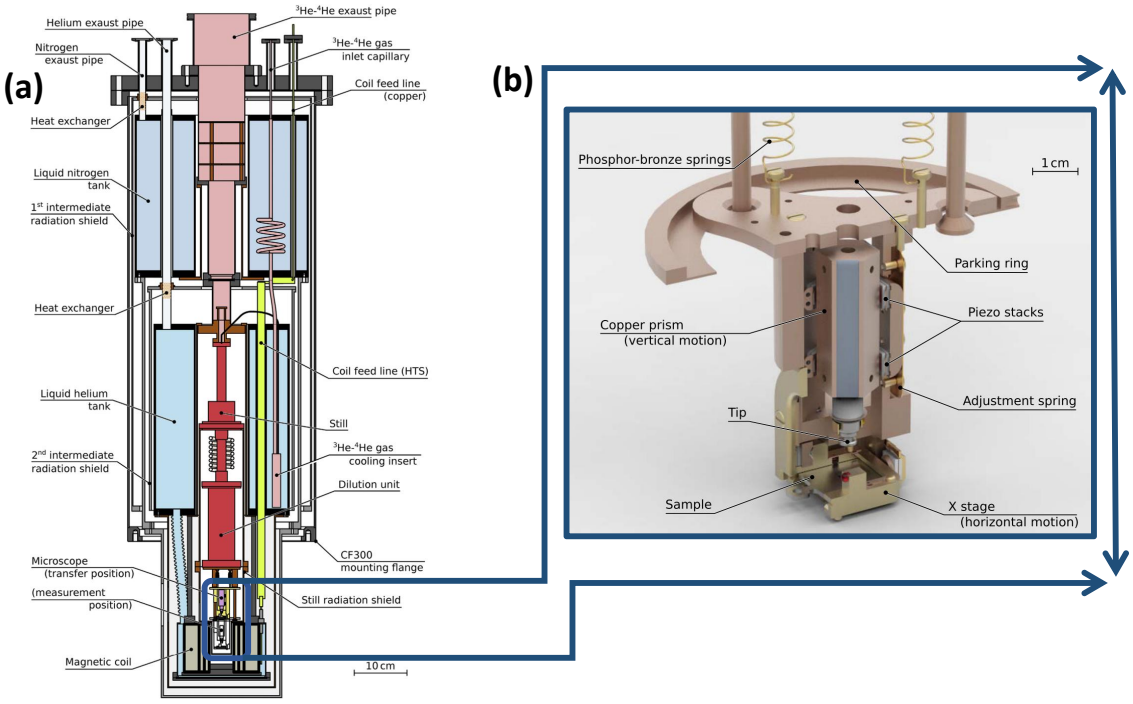

Figure 3.3: (a) Simplified diagram of the cryostat showcasing the liquid nitrogen and helium tanks (blue), the dilution insert (red), the gas circulation system (pink), the scanning tunneling microscope (STM), and the superconducting magnet. The current supply lines are indicated in green. (b) Close-up view of the section highlighted in the blue box in (a), presenting a 3D rendering (cross-section) of the STM and components of the suspension system. The copper ring is utilized to elevate the STM to the parked position without making contact during measurements. The diameter of the STM body is 30 mm. Figure adapted from [131].

pumping the still during this phase, the lower vapor pressure of ^{4}He results in the pumping out of ^{3}He from the diluted phase, creating a non-equilibrium situation at the interface between the two phases. This process, known as endothermic phase separation, effectively extracts energy from the environment, further cooling it down. By coupling the STM body to the mixer, its temperature can be reduced to the base temperature, enabling precise measurements at ultra-low temperatures.

3.3 Magnetic Field Setup

In addition to the STM setup, a magnetic coil is incorporated to facilitate the application of magnetic fields to the experimental systems. Positioned around the STM body during experiments, the coil is designed to envelop the sample area effectively, as shown in Figure 3.4.

In the JT-STM, the system was equipped with a superconducting magnet, capable of generating magnetic fields perpendicular to the sample surface, reaching up to 4 T. While in the Dilution STM

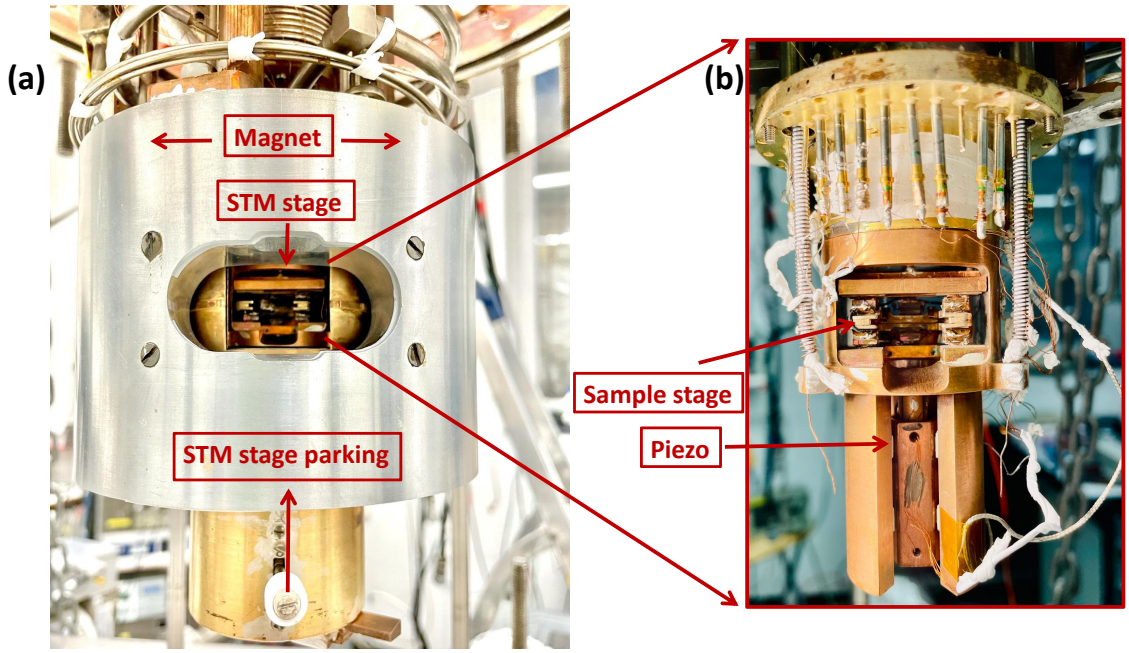

Figure 3.4: (a) STM stage surrounded by magnet. (b) Zoomed-in view of STM stage.

system, it can reach up to 7.5 T. The current flowing through the coil is meticulously controlled by a commercial controller supplied by Oxford Instruments, enabling precise regulation of the applied magnetic field intensity as well as the rate at which it ramps up or down. This setup allows for the controlled manipulation of magnetic parameters during experimental investigations, offering insights into the magnetic behavior of the samples under study.

3.4 In-Situ Sample and Tips Preparation Facilities

3.4.1 Molecular Beam Epitaxy

Molecular Beam Epitaxy (MBE) is a sophisticated technique used to grow thin films with atomic precision. In MBE, materials are deposited onto a substrate, allowing for precise control over the composition, thickness, and structure of the thin film. The process involves evaporating solid materials, typically in the form of elemental sources or molecular beams, in ultra-high vacuum conditions. These evaporated materials then travel in the form of molecular or atomic beams to a heated substrate where they condense and form a thin film. The substrate is typically heated to a specific temperature to facilitate the adsorption and diffusion of the incoming atoms or molecules.

One of the key advantages of MBE is its ability to produce epitaxial films, meaning the deposited atoms or molecules align with the underlying crystal lattice of the substrate, leading to high-quality and defect-free thin films. This precise control over the growth process allows researchers to

engineer materials with tailored electronic, optical, and magnetic properties for various applications in electronics, photonics, and spintronics. MBE is widely used in both academic and industrial research laboratories to fabricate a wide range of materials, including semiconductors, metals, oxides, and heterostructures. It has played a crucial role in advancing our understanding of fundamental material properties and in the development of novel electronic and optoelectronic devices.

3.4.2 Sputtering and Annealing Method

To ensure clean surfaces suitable for STM measurements, single crystal samples undergo a rigorous cleaning process within the preparation chamber. This involves a standard procedure involving Ar^+ sputtering followed by high-temperature annealing [132]. Within this chamber, various devices and facilities are available to facilitate sample cleaning and surface quality assessment.

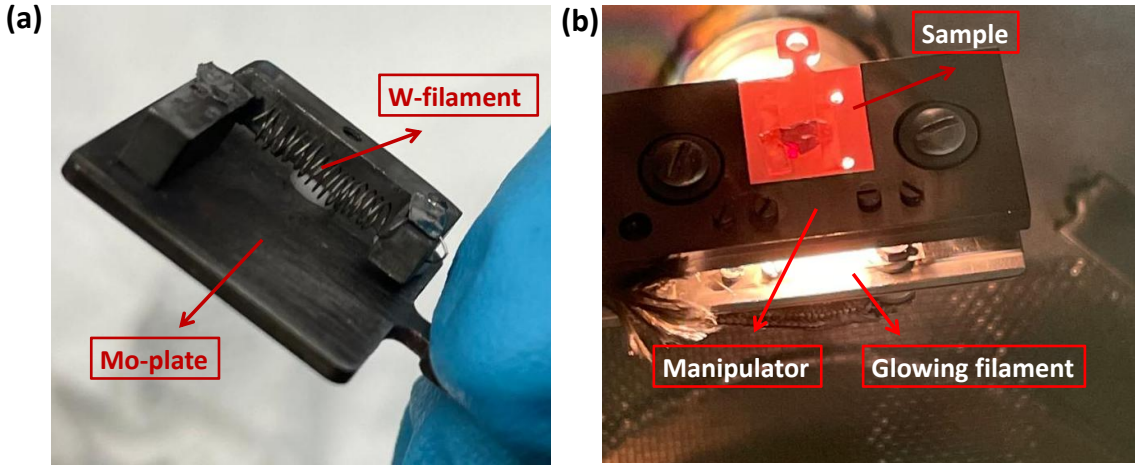

Figure 3.5: (a) W-Filament mounted on a Mo plate. (b) Operational principle of the sample annealing process employing the filament.

Ar^+ ions are directed onto the sample surface using a sputter gun, where they impact with a kinetic energy exceeding 1 kV. The ions are aimed at an incidental angle of 45°, effectively removing surface layers over approximately half an hour. Following sputtering, any resulting surface roughness is mitigated through annealing. During this step, the sample is heated from the rear using electron bombardment. A filament within the manipulator's head, as shown in Figure 3.5, emits thermal electrons, which are accelerated towards the sample by applying a voltage of up to 1000 V. The temperature during heating is monitored using single-band or more advanced two-color ratio pyrometers, tailored to the desired temperature range. For samples exposed to air, multiple cleaning cycles may be required to achieve optimal surface cleanliness. However, if the sample has been stored in vacuum, a single cleaning cycle may suffice.

3.4.3 STM Tips preparation

Tungstun (W) Tip

The STM tip, shown in Figure 3.6(a), undergo initial etching in air using electrochemical etching with a 5% NaOH solution from 300 μm thick tungsten wire. The estimated radius of the tip apex post-etching is approximately 10 nm. Subsequently, the tips are transferred into a vacuum environment and degassed. They are then subjected to sputtering with Ar^+ ions for 50 minutes, followed by electron beam heating from a filament located on the transfer tip holder approximately 0.5 mm away from the tip. The tip experiences flashes with acceleration potentials ranging from 500 V to 1200 V. During the first cycle, the beam current is elevated to achieve a slight melting of the tip apex. Subsequent treatments are conducted with just enough harshness to remove adsorbates from the tip. Once cleaned, the tip is transferred to the STM chamber to perform measurements, as illustrated in Figure 3.6(b).

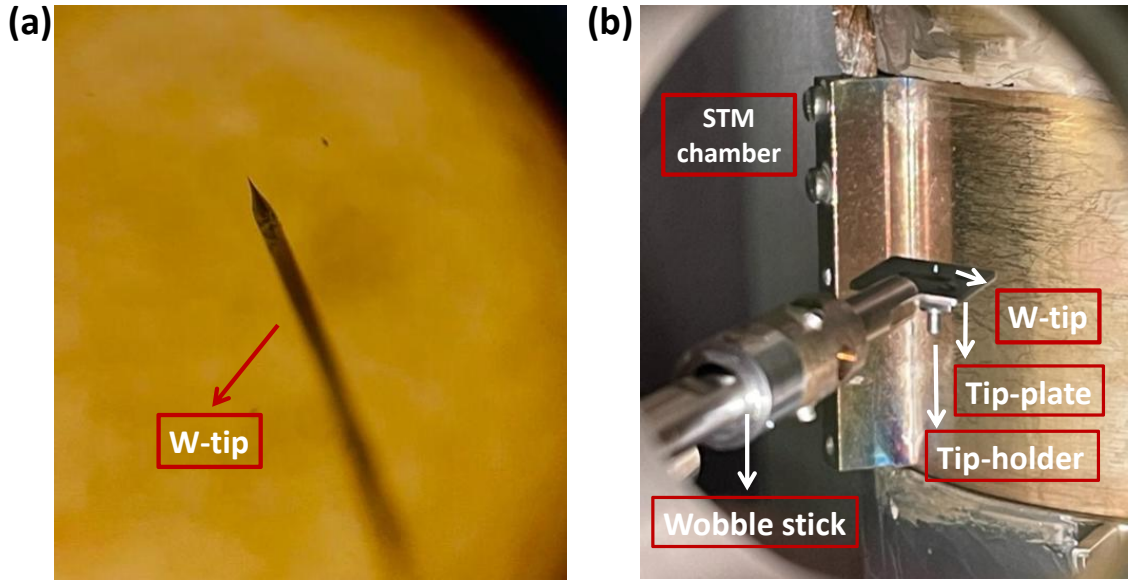

Figure 3.6: (a) Microscopic view of a freshly prepared W-tip using the electro-chemical etching process. (b) Transfer mechanism of the tip into the STM stage under UHV conditions.

Spin-Polarized Tip

To explore various magnetic properties, magnetic tips were employed. Following the preparation of tungsten (W) tips as previously described, the tip underwent a coating process with magnetic material (chromium in this case) by evaporating around 50 ML of chromium atoms from the evaporator within the preparation chamber. Subsequently, the chromium-coated tip underwent gentle annealing for 2 minutes to eliminate any contaminants or residual materials that may have

adhered to the tip during the coating process. This annealing process served to smoothen the surface of the coated material on the tip and stabilize its magnetic properties. Overall, annealing the STM tip subsequent to the coating with magnetic material was a pivotal step in its preparation for magnetic STM measurements, ensuring cleanliness, smoothness, and stability for precise and dependable imaging and measurements.

3.4.4 Sample Preparation

Ag(111) crystal

To assess the tip's condition, we utilized reference samples to examine their surfaces, aiding in the determination and potential improvement of the tip's condition. In this work, we employed an Ag(111) crystal as our reference sample. The Ag(111) crystal was initially introduced into the machine via a loadlock system. Subsequently, the sample underwent degassing in the high vacuum stage of the loadlock until an appropriate pressure level was achieved. It was then transferred to the preparation chamber for further processing. Within the preparation chamber, the sample underwent multiple cycles of sputtering and annealing. Sputtering was carried out using 4 keV Ar^+ ions for a duration of 50 minutes to eliminate surface contaminants. Following each sputtering cycle, the sample was subjected to annealing using an electron beam emitted from a filament positioned behind the sample on the sample holder. This annealing process aided in the removal of residual Ar atoms and promoted surface smoothing. The annealing temperature was maintained at approximately 550 °C, carefully controlled to remain below the sample's melting point. During the initial cycles, the annealing temperature was deliberately kept low to prevent the diffusion of surface adsorbates into the sample.

FGT Bulk Crystal

The FGT crystal, depicted in Figure 3.7(a), was initially mounted on a copper plate using epoxy glue (a permanent conducting glue). Subsequently, the cleaving process was carried out using kapton tape in a normal atmospheric environment to eliminate any surface contamination before transferring the crystal to the preparation chamber (refer to Figure 3.7(b)).

Following this, the pristine crystal underwent *in-situ* exfoliation under a base pressure of approximately 1×10^{-9} mbar. This process involved affixing one end of UHV-compatible kapton tape to the bulk FGT sample, while the other end was attached to the sample rack in the load lock. As the load lock was evacuated to reach base pressure, the sample was extracted from the rack using a wobble stick, facilitating smooth exfoliation of the sample surface, as illustrated in Figure 3.7(c).

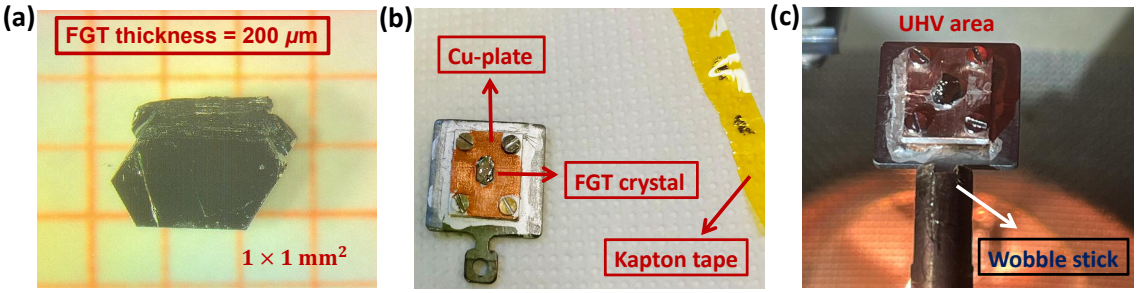

Figure 3.7: ((a) FGT bulk crystal. (b) Cleaving process of the FGT surface using kapton tape. (c) In-situ cleaving of the FGT crystal surface under ultra-high vacuum (UHV) conditions.

Consequently, this procedure resulted in the thinning of the bulk sample and the creation of a fresh, flat surface conducive to STM investigation.

Chapter 4

Study of monolayers of VSe_2 grown on HOPG

This chapter serves as a catalyst for delving into the realm of ferromagnetism within two-dimensional (2D) van der Waals materials. Our journey begins with a deep dive into VSe_2, a prominent member of transition-metal dichalcogenides (TMDs), renowned for its multifaceted properties. Here, our attention is specifically directed towards the monolayers (ML) of VSe_2 and their growth on highly oriented pyrolytic graphite (HOPG) substrates (ML VSe_2/HOPG), accomplished through the Molecular Beam Epitaxy (MBE) technique. Through this endeavor, we aim to unravel the intricate interplay of magnetic phenomena within this fascinating material system.

4.1 Introduction

VSe_2 belongs to the family of TMDs, which are layered materials composed of transition metal atoms sandwiched between two layers of chalcogen atoms. In the case of VSe_2, the crystal structure is typically described as a hexagonal lattice with two layers of selenium atoms (Se) forming the top and bottom layers, and a layer of vanadium (V) atoms located between them. Each vanadium atom binds to six selenium atoms, forming a trigonal prismatic coordination geometry.

The unit cell of VSe_2 is hexagonal in shape, consisting of three crystallographic axes: two in-plane axes (a_1 and a_2) and one perpendicular axis (c). The lattice parameters of the unit cell define the dimensions of these axes and the angles between them. Within the unit cell, there are three atoms: one vanadium atom and two selenium atoms. The vanadium atom occupies a position in the center of the unit cell as shown in Figure 4.1, while the selenium atoms are located above and below the

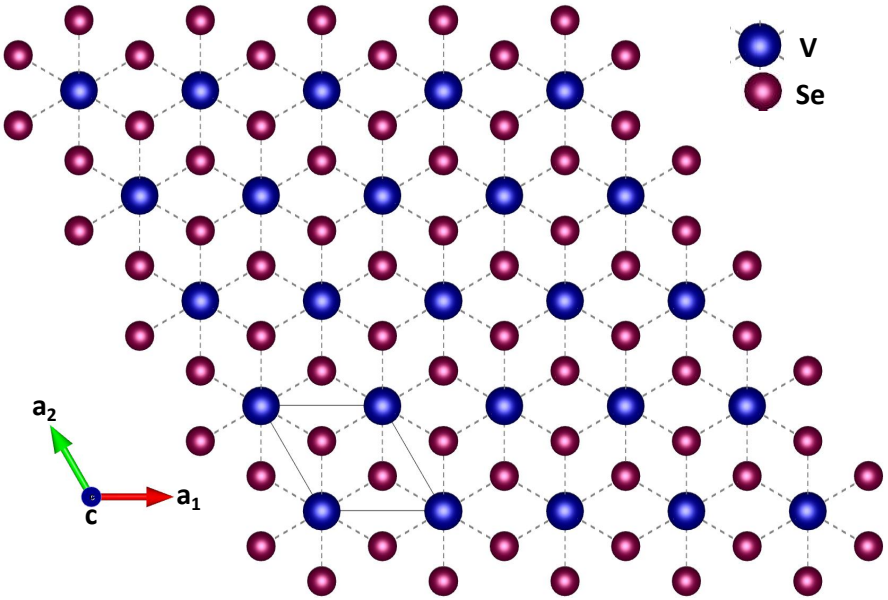

Figure 4.1: Top view: Atomic arrangement and unit cell of VSe_2.

vanadium atom, forming a V-Se-V sandwich structure. The arrangement of atoms within the unit cell of VSe_2 gives rise to the material's unique electronic and optical properties. For example, the layered structure of VSe_2 leads to weak interlayer interactions, resulting in the material's anisotropic properties and the ability to be exfoliated into thin flakes with distinct electronic behavior.

The ferromagnetic characteristics of monolayer VSe_2 have sparked considerable debate within the scientific community, with conflicting findings complicating our understanding. While some studies have asserted the presence of ferromagnetism in VSe_2 monolayers [133–135], others have reported no compelling evidence to support such claims [136, 137]. In an effort to resolve this ongoing dispute and shed light on the true nature of ferromagnetism in VSe_2 monolayers, our investigation turns to the application of the STS technique. Through meticulous analysis and experimentation, we aim to elucidate the ferromagnetic properties of VSe_2 monolayers and contribute to the broader understanding of magnetism in two-dimensional materials.

4.2 Sample Preparation

4.2.1 Molecular Beam Epitaxy

Molecular Beam Epitaxy (MBE) stands as a highly advanced method employed in fabricating thin films with atomic-level accuracy. With MBE, materials are meticulously layered onto a substrate, adding one atomic sheet at a time. This meticulous process grants exacting control over the thin film's composition, thickness, and arrangement. The sample preparation involved the growth of

mono- to few-layer VSe_2 on HOPG substrate using MBE within an UHV condition, maintaining a base pressure of 2×10^{-10} mbar. The HOPG substrate underwent cleavage and annealing within the UHV chamber.

The process began with degassing the Se-evaporator to eliminate any unwanted contamination and stabilize the evaporation process, achieving a base pressure of 2×10^{-9} mbar and an initial temperature of 28 °C. The current was gradually increased to 1 A once stability was attained. Subsequently, the voltage of the Se-evaporator was raised to 1.4 V, elevating the temperature to 45°C and increasing the pressure to 6.5×10^{-9} mbar. Similarly, the V-evaporator was degassed at 2.5 A. Following the degassing procedure, Selenium atoms were evaporated from a Knudsen cell, while vanadium atoms were evaporated from an electron-beam evaporator and deposited onto the substrate. The coverage of ML VSe_2 was modulated by adjusting the growth time and the fluxes of atoms. We employed a much higher Se flux than necessary for the growth of VSe_2. The excess Se has been observed to evaporate from the hot surface, resulting in the growth of stoichiometric VSe_2, analogous to the growth of FeSe [138, 139].

4.2.2 Vacuum Suitcase for Sample Transfer

A vacuum suitcase is designed to uphold a low-pressure environment essential during experiments. It features designated slots for securely housing samples or STM tips within a controlled vacuum, effectively shielding them from external influences like air molecules, dust, or humidity. By maintaining this vacuum environment, the stability of both the sample and the probe tip is ensured, minimizing potential disruptions and preserving measurement accuracy.

Following the completion of sample growth via MBE technique, we utilized a vacuum suitcase to transfer the freshly grown sample from the MBE chamber to the JT-STM machine, which is situated in separate laboratory, for subsequent STM measurements. The vacuum suitcase maintains a pressure level of approximately 10^{-7} to 10^{-8} mbar. It was connected via the load lock region in the STM machine and adequately pumped to facilitate the transfer to the preparation chamber. This chamber operates under ultra-high vacuum (UHV) conditions, with a base pressure of 10^{-10} mbar, ensuring a pristine environment for further experimental procedures.

4.2.3 Post-Annealing Process

Following sample growth, a post-annealing procedure was implemented to cleanse and refine the surface of the sample. The annealing process was conducted gently for a short duration to avoid any adverse effects on the sample. Prolonged annealing sessions were avoided to prevent the inadvertent

removal of monolayers of VSe_2 deposited on the HOPG substrate. This careful approach ensured that the sample surface remained intact while effectively removing any impurities or irregularities that may have been present post-growth. After this process, the sample was directly transferred to the STM chamber for the STM measurements.

4.3 Scanning Tunneling Microscopy Measurements

4.3.1 Surface Analysis

To investigate the surface morphology of MLs of VSe_2/HOPG, we conducted scanning tunneling microscopy (STM) measurements under UHV condition at low temperature of 700 mK. Initially, we performed a large-scale topographic scan covering an area of 2×2 μm^2, as depicted in Figure 4.2(a). This scan revealed numerous VSe_2 islands exhibiting various shapes and thicknesses. The hexagonal structure of VSe_2, however, is reflected in the shape of the islands.

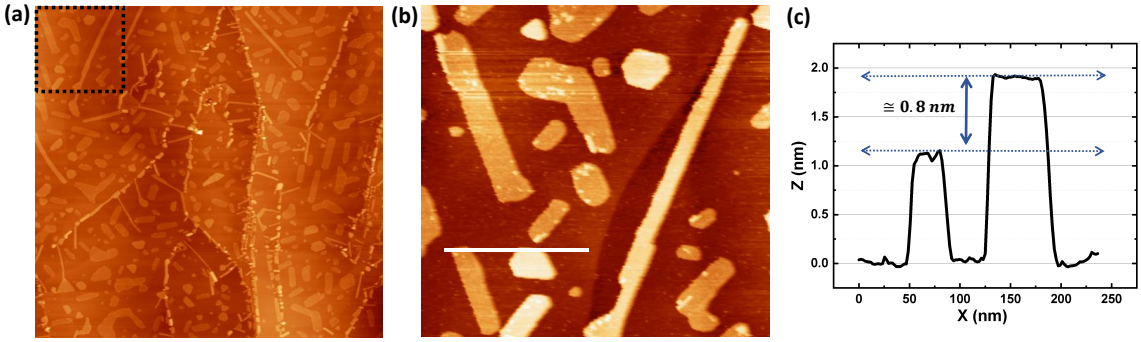

Figure 4.2: (a) Large-scale STM topographic scan showing monolayers of VSe_2 on HOPG substrate (2×2 μm^2 at -100 mV, 10 pA). (b) Zoom-in to black square box shown in (a) revealing high-resolution images of monolayer and bilayer VSe_2 islands with diverse shapes (500×500 nm^2 -100 mV, 5 pA,). (c) Line profile analysis confirming the atomic layer distance between two islands (1ML ≈0.8nm).

To gain deeper insights into these islands, we focused on a specific region specified by the black square box in Figure 4.2(a) and conducted a higher resolution scan. Figure 4.2(b) presents the resulting high-resolution images, showcasing both monolayer and bilayer VSe_2 islands. To verify the thickness of these islands, we conducted line profile analysis between two distinct islands, as indicated by the white line in Figure 4.2(b). The line profile, depicted in Figure 4.2(c), revealed that the distance between these islands corresponds to the atomic layer distance. This analysis conclusively confirmed the successful growth of both monolayer and bilayer of VSe_2/HOPG, as revealed by the STM topographic measurements.

4.3.2 Charge Density Wave

To delve deeper into the surface characteristics, we conducted zoom-in STM scans, showcased in Figure 4.3(a) for topography and in Figure 4.3(b) for the derivative topography of the same scan which used to enhance contrast and highlight subtle surface features. Within this scan, we discerned faint stripe-like features, notably visible within the black square box in Figure 4.3(b).

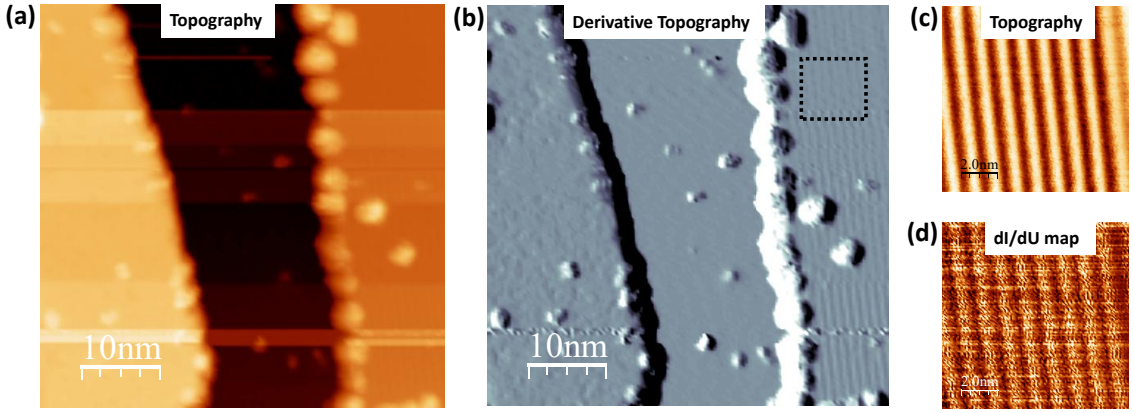

Figure 4.3: STM scans on VSe_2/HOPG surface: (a) Zoom-in topography at 1 V, 50 pA (50×50 nm^2), (b) Derivative topography, highlighting faint stripe-like features, (c) High-resolution scan of CDW taken on the boxed area in (b) (10×10 nm^2), (d) Corresponding differential conductance map of CDW at 0.2 V and 50 pA.

To gain a clearer understanding of these features, we further narrowed our focus by zooming into the area depicted by the black box. Figure 4.3(c) exhibits the resultant high-resolution topographic scan, providing enhanced detail of the stripe-like features. Corresponding to this topography, we generated a differential conductance map, presented in Figure 4.3(d). These complementary image and map allowed us to scrutinize the structural and electronic properties of the observed features with greater precision, aiding in the comprehensive characterization of the surface morphology and its associated behavior.

The stripe pattern observed on the monolayers of VSe_2/HOPG refers to a recurring pattern of alternating regions with higher and lower charge densities across the surface of the material. This stripe pattern is attributed to the phenomenon known as the "charge density wave" (CDW). The CDW is a collective electronic state that occurs in certain materials, characterized by periodic modulations in the distribution of charge carriers. In the context of monolayers of VSe_2/HOPG, the CDW reveals as a periodic rearrangement of electrons within the material. It generally comes with the formation of a gap in the band structure near the Fermi energy. Moreover, the CDW state suppresses the ferromagnetic ground state. Ferromagnetic order has only seem predicted in VSe_2

in the absence of CDW states.

4.4 Scanning Tunneling Spectroscopy

4.4.1 STS Assessments Across Various Regions

We conducted scanning tunneling spectroscopy (STS) measurements on three distinct regions: the HOPG surface (depicted in black), a monolayer (1 ML) of VSe_2 (shown in red), and a bilayer (2 ML) of VSe_2 (displayed in blue), as depicted in the topographic scan of Figure 4.4(a). In the STS spectra presented in Figure 4.4(b), a clear minimum was observed at the Fermi level taken from the VSe_2 regions. In contrast, this minimum was not as prominently visible in the STS spectra obtained from the HOPG surface. This observation solidifies the notion that the observed minimum at the Fermi level is a characteristic trait of VSe_2 rather than HOPG.

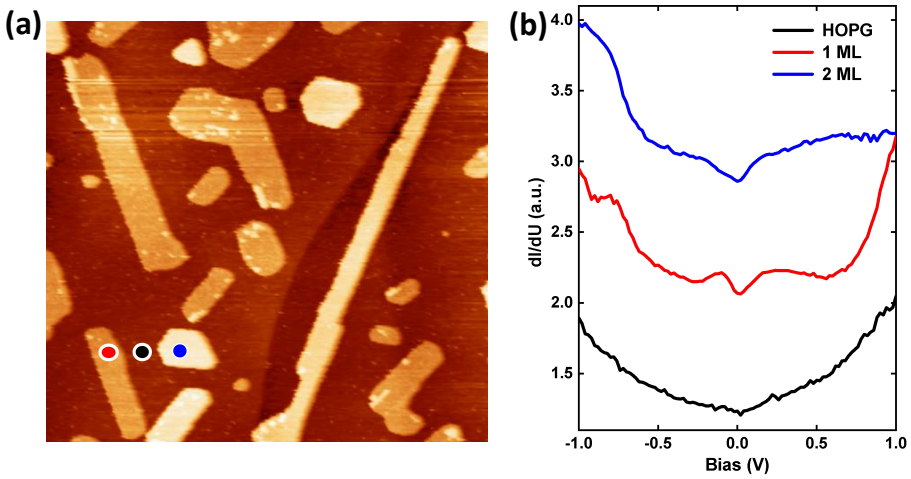

Figure 4.4: (b) Scanning tunneling spectroscopy (STS) measurements taken at three distinct points, corresponding to the topographic scan shown in (a). HOPG (in black), 1 ML (in red), and 2 ML (in blue) of VSe_2.

This minimum indicated the presence of an energy gap, which arose due to the formation of a CDW. In materials like ML and DL VSe_2, the CDW formation led to the opening of an energy gap near the Fermi level. This gap signified a lack of electronic states available for tunneling at that particular energy, resulting in a reduced tunneling current and thus a distinct minimum in the STS spectra. The observation of this minimum across both monolayer and bilayer VSe_2 regions confirmed the presence and consistency of the CDW phenomenon in these materials. This insight into the electronic structure and CDW behavior can explain the conflicting results regarding magnetism in VSe_2. The CDW state is non-magnetic and can potentially be suppressed by disorder favouring the magnetic ground state instead.

4.4.2 STS of CDW Patterns Under Magnetic Field

We conducted STS measurements to analyze the CDW patterns (referred in Figure 4.3(c)) observed along the designated line, as illustrated in the inset of Figure 4.5. The spectra were acquired utilizing a modulation voltage of 10 mV with a frequency of 913 Hz, while traversing a stripe defect region.

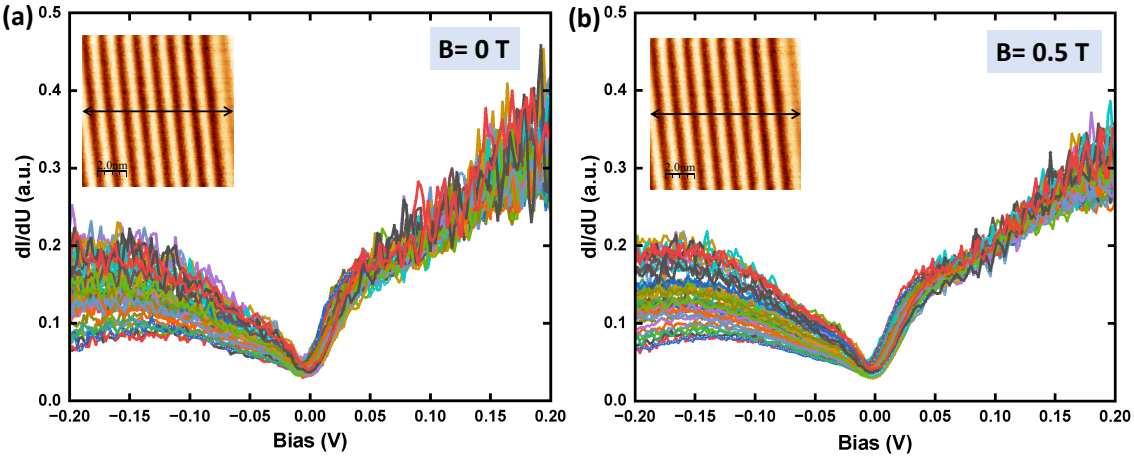

Figure 4.5: Scanning tunneling spectroscopy measurements conducted along the designated line across CDW pattern, as depicted in the insets of both (a) at 0 T and (b) at 0.5 T. Tunneling conditions: V_t= 200 mV, I_t= 50 pA, $\pm U_{mod}^{rms}$= 10 mV, at 913 Hz.

In order to explore potential magnetic influences or detect magnetic characteristics, we performed STS measurements under an external out-of-plane magnetic field of 0.5 T, depicted in Figure 4.5(b), within the same spatial region. A comparison with Figure 4.5(a), captured under 0 T, reveals practically no clear evidence, confirming the non-magnetic nature of the films.

4.5 Summary

In this study, we grew high quality monolayers of VSe_2 on HOPG substrates using MBE technique. STM measurements provided clear evidence of the presence of monolayer VSe_2 islands, confirming the effectiveness of our growth technique. Furthermore, our investigation shed light on the formation of CDW patterns on these monolayers, enhancing our understanding of their structural characteristics.

STS measurements conducted on these islands revealed a distinct minimum near the Fermi level for both monolayer (ML) and bilayer (DL) VSe_2, indicative of the energy gap associated with CDW formation. Conversely, no such minima were observed for HOPG, suggesting that the observed minimum solely originates from VSe_2. Furthermore, STS analysis on CDW patterns confirmed the appearance of the minimum at the Fermi level, independent of external magnetic field influence.

In conclusion, we speculate that the presence of the CDW state in high-quality samples may suppress magnetism, shedding light on the interplay between CDW formation and magnetic properties in VSe_2 monolayers grown on HOPG substrates.

Chapter 5

Study of Fe_3GeTe_2: Crystal Growth, Elemental Analysis, and Magnetic Properties

Expanding on the discoveries outlined in the previous chapter, which revealed the absence of ferromagnetism in the 2D TMD monolayer of VSe_2 on HOPG - a pivotal discovery within the context of this thesis- we now turn our focus to notable 2D van der Waals ferromagnetic material: Fe_3GeTe_2 (FGT).This chapter initiates on a comprehensive exploration of the surface properties of FGT. The investigation surrounds various aspects, including the crystal growth process by chemical vapor transport (CVT) method, elemental characterization utilizing energy-dispersive X-ray spectroscopy (EDX) and analysis of magnetic properties employing the Quantum Design Magnetic Property Measurement System (QD-MPMS).

5.1 Introduction

Magnetism has been confirmed in various 2D vdW materials, including CrI_3 (T_C = 45 K), $Cr_2Ge_2Te_6$ (T_C = 30 K), and Fe_3GeTe_2 (FGT), among others [89, 90, 140–145]. For a comprehensive overview of over sixty different magnetic vdW materials, please refer to reference [92]. Among these materials, FGT has assembled significant attention due to its high ferromagnetic transition temperature of 150-220 K [143] and its purported semi-metallic nature [144].

FGT is a well known pseudo-2D transient ferromagnetic (FM) metal [146, 147]. Its unit cell comprises two Fe_3Ge layers sandwiched between two Te layers, adhering to the $P6_3/mmc$ space

group (a = 3.991 Å, c = 16.33 Å). Within this structure, two distinct Wyckoff positions are occupied by Fe atoms labeled Fe_α and Fe_β (see Figure 5.1). The Fe_α atoms reside within a hexagonal network within a layer solely composed of Fe atoms, while Fe_β and Ge atoms form covalent bonds in an adjacent layer. The Fe_3Ge layers are separated by van der Waals-gapped Te double layers.

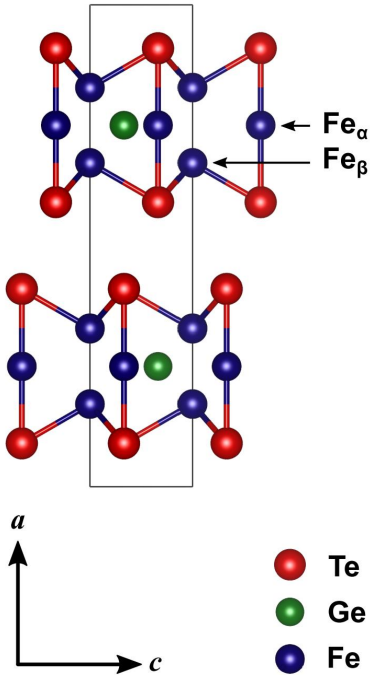

Figure 5.1: Crystal structure of Fe_3GeTe_2.

5.2 Experimental Details and Observations

5.2.1 Sample Preparation and Growth

The crystal growth process for $Fe_{3-\delta}GeTe_2$ ($\delta \approx 0.04$) was a collaborative effort led by Prof. Dr. Matthieu Le Tacon, Dr. Amir-Abbas Haghighirad and Dr. Kaushik Sen. Utilizing the chemical vapor transport method with I_2 and $TeCl_4$ as transport agents, high-quality single crystals were successfully synthesized, as illustrated in Figure 5.2. The synthesis involved combining high-purity Fe (Alfa Aesar, 99.999%), Ge (Merck, 99.999%), and Te (G-Materials, 99.999%) in a molar ratio of 3.1:1:2, respectively. The resulting mixture was loaded into a fused silica tube, evacuated, and sealed. Subsequently, the sealed ampule underwent a temperature gradient ranging from 750 °C to 670 °C in a zone furnace for a duration of 10 days. This process facilitated the growth of single crystals, characterized by a hexagonal sheet-like morphology observed in the low-temperature region of the ampule.

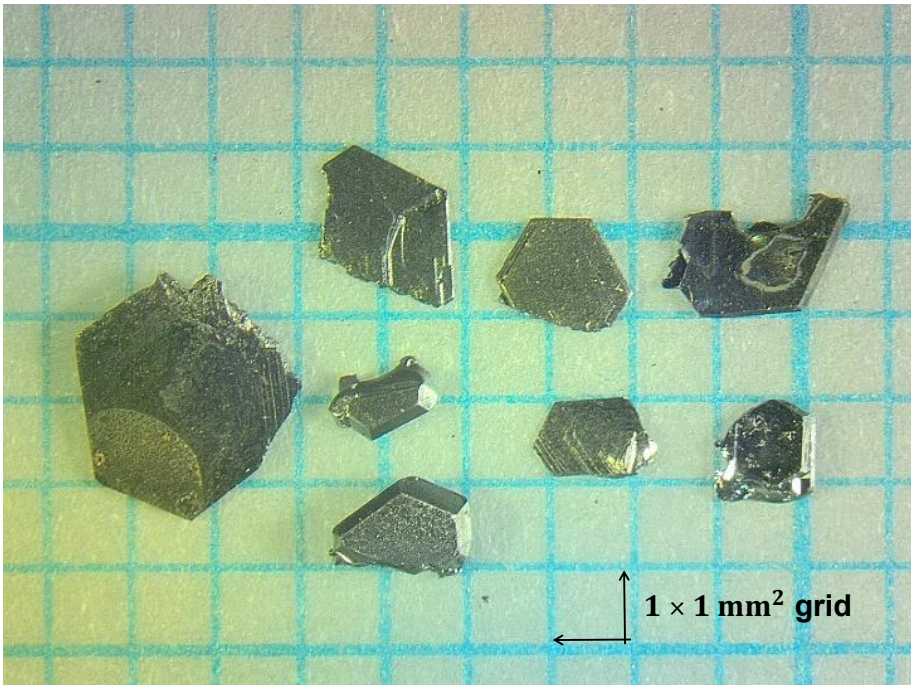

Figure 5.2: Fe_3GeTe_2 crystals.

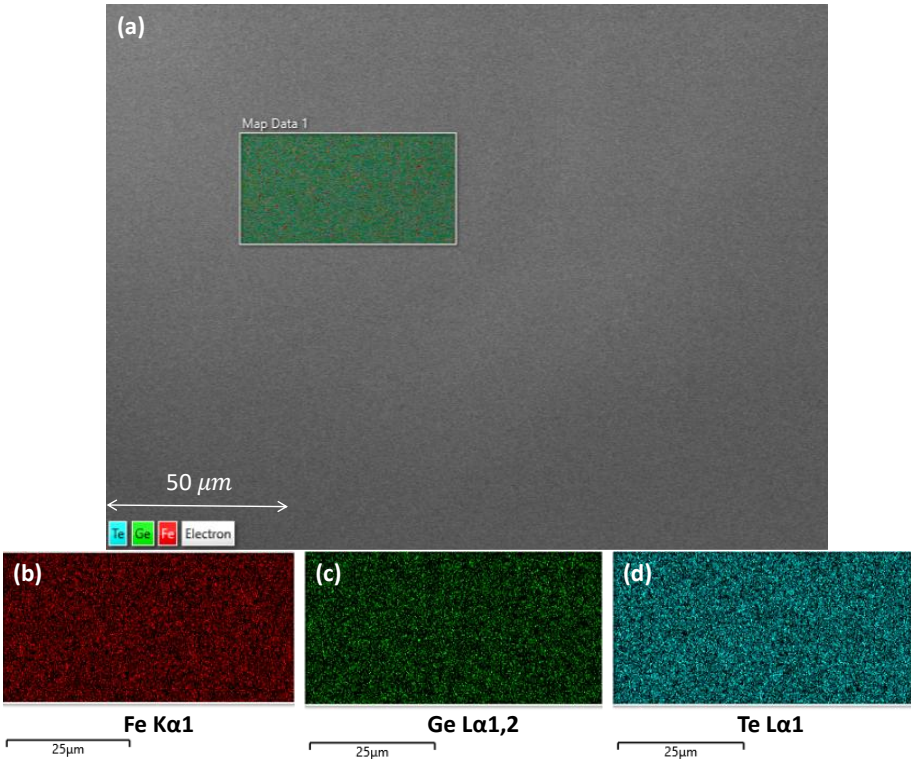

Figure 5.3: (a) Energy-dispersive X-ray spectroscopy (EDX) on freshly cleaved Fe_3GeTe_2 surface. EDX elemental mapping for (b) Fe, (c) Ge and (d) Te, respectively, showing a homogeneous distribution of these three elements in Fe_3GeTe_2.

5.2.2 Chemical Composition Characterization

The chemical composition of the crystals was analysed using energy-dispersive X-ray spectroscopy (EDX), which was performed with a Coxem EM-30^N benchtop scanning electron microscope (SEM) equipped with an Oxford Instruments detection system. A freshly cleaved FGT crystal was subjected to EDX scanning, covering an area indicated by the white box in Figure 5.3(a). EDX mapping was conducted at room temperature (RT, 300 K), yielding maps for Fe, Ge, and Te, shown in Figures 5.3(b), 5.3(c), and 5.3(d) respectively, indicating a uniform distribution of Fe, Ge, and Te throughout the crystal.

In Figure 5.3(b), "Fe Kα1" in EDX mapping denotes the primary X-ray emission line associated with the transition of an electron from the K shell to the L shell in iron (Fe) atoms. In X-ray spectroscopy, when elements are excited by an external energy source like an electron beam, they emit characteristic X-rays that are specific to each element. This specific emission can be used to identify and quantify the elemental composition of a sample. The "Kα1" notation signifies that this emission line is the first in the K series of X-ray emissions for iron.

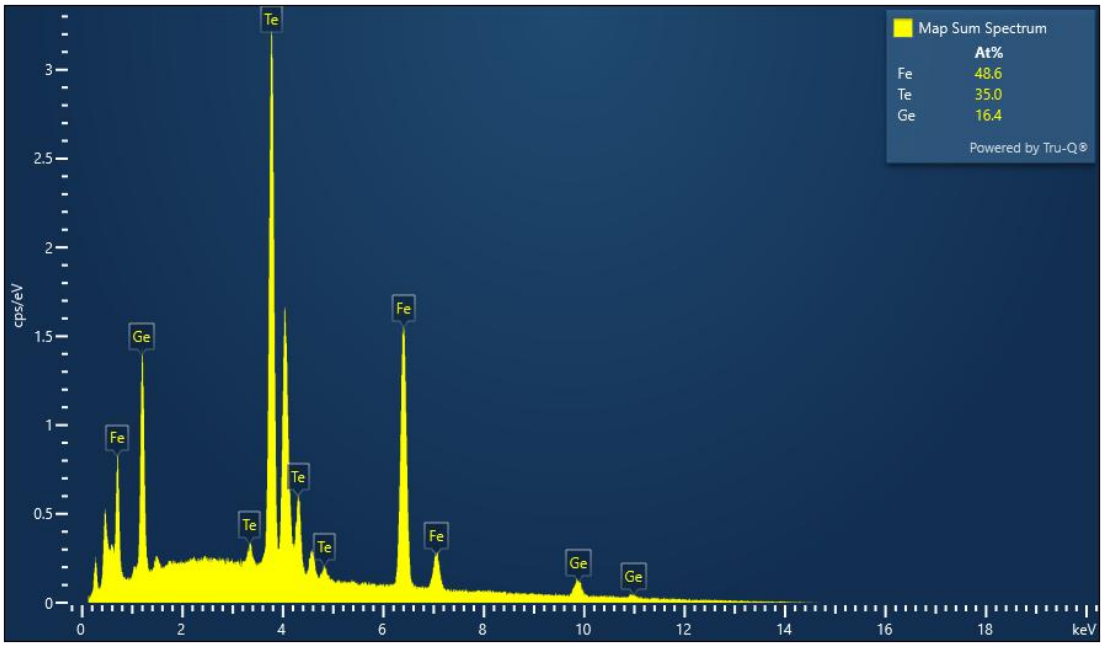

Figure 5.4: EDX spectrum of Fe_3GeTe_2.

In Figure 5.3(c), "Ge Lα1,2" refers to the characteristic X-ray emission lines associated with the transitions of electrons within the L shell of germanium (Ge) atoms. Specifically, the Lα1 line corresponds to the transition from the L3 to the L1 subshell, while the Lα2 line corresponds to the transition from the L3 to the L2 subshell. These emissions can be utilized to identify and quantify the presence of germanium in a sample.

Lastly, in Figure 5.3(d), "Te Lα1" designates the primary X-ray emission line associated with the transition of an electron within the L shell of tellurium (Te) atoms. This emission line can be employed to identify and quantify the presence of tellurium in a sample using techniques such as energy-dispersive X-ray spectroscopy (EDX).

The EDX spectrum [Figure 5.4] was obtained to determine the elemental composition of the FGT bulk crystal, which was found to be- for Fe (48.6%), for Ge (16.4%) and for Te (35%) which is approximately $Fe_{2.96}GeTe_{2.13}$. The iron (Fe) deficiency (δ = 0.04) from the stoichiometric composition of FGT was calculated to be 4%.

5.2.3 Magnetic Characterization

Our collaborators utilized a Quantum Design Magnetic Property Measurement System (QD-MPMS) to study magnetism in FGT bulk system. From the batch, they selected a well-formed plate-like FGT crystal, where the magnetic field (H) was applied both along the ab-plane and the c-axis of the sample. Initially, measurements were conducted with the field aligned along the ab-plane. The mass of the sample was determined to be 1.03 mg. However, during the repositioning of the sample for measurements with the field along the c-axis, a portion of the sample was unintentionally lost, likely due to exfoliation on Kapton tape. As a result, the sample mass was reduced to 0.76 mg.

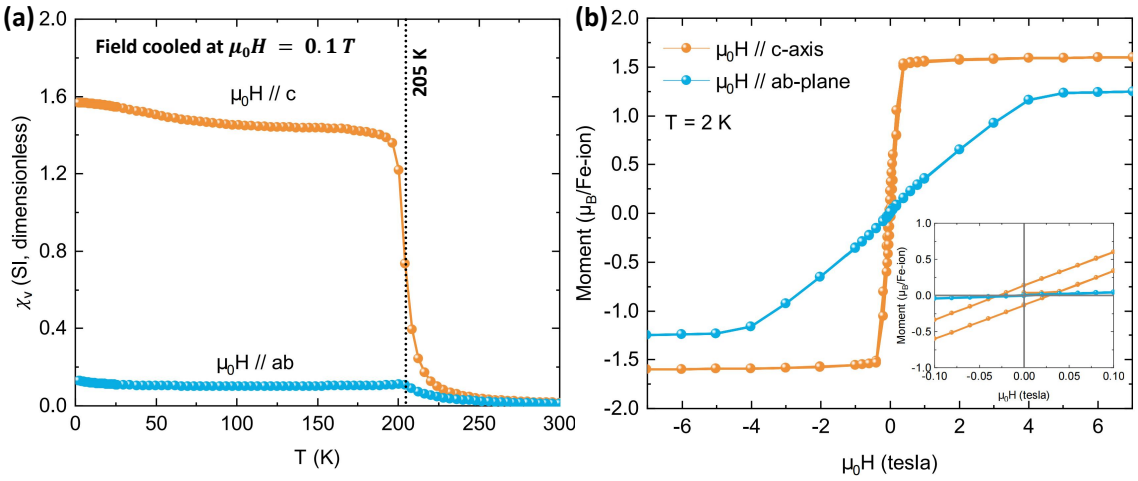

Figure 5.5: (a) Magnetic volume susceptibility(χ_v) as a function temperature measured in field-cooled condition (0.1 T). (b) Squid measurement displaying magnetic moment plotted as a function of applied magnetic field taken at 2 K, obtained along the c-axis (orange curve) and the ab-plane (blue curve).

In Figure 5.5(a), the magnetic volume susceptibility (χ_v) is plotted against temperature (T) for both

H || c and H || ab orientations. The χ_v-vs-T curve unequivocally confirms FGT's ferromagnetic nature, with a critical temperature (T_c) of 205 K. Notably, χ_v exhibits anisotropy depending on the direction of the applied magnetic field. Specifically, χ_v is 15 times larger when H is aligned along the c-axis compared to the ab-plane, indicating that the magnetic easy axis aligns along the c-axis, consistent with Fe-moments preferring alignment along this axis. This observation is further supported by the M-H loops measured at 2 K, as depicted in Figure 5.5(b). While saturation magnetization requires a substantial field of $H \geq 4$ tesla when H || ab, saturation is achieved at a mere 0.5 T when H || c. Additionally, the ferromagnetic coercivity is approximately 0.03 T, and the average ferromagnetic moment is found to be M_s = 1.58 μ_B/Fe-ion. Fitting the high-temperature region (265 K to 300 K) of the χ_v-vs-T curve with the Curie-Weiss law yields an effective moment of m_{eff} = 2.85 μ_B/Fe-ion, indicating a degree of itinerancy in FGT of m_{eff}/M_s = 1.8. Below 50 K, anomalies are observed in the χ_v-vs-T curves for both H || c and H || ab orientations (see Figure 5.6(a) and 5.6(b)).

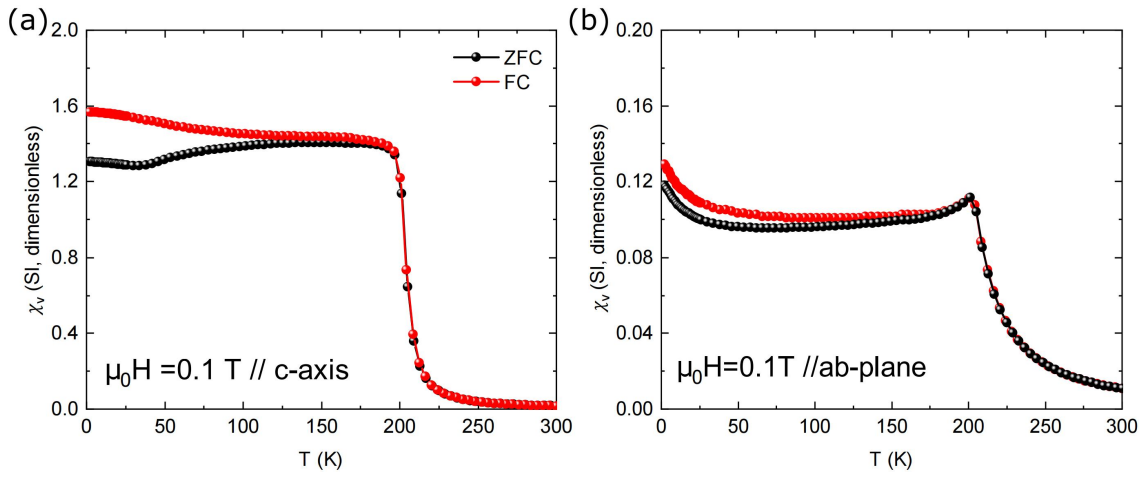

Figure 5.6: (a) χ_v-vs-T in zero-field-cooled (ZFC) and field-cooled (FC) conditions at H || c. (b) The corresponding plot at H || ab.

These anomalies may suggest either a secondary magnetic transition within FGT or the presence of Fe vacancies in the system. Intriguingly, χ_v exhibits a slight decrease just below the ferromagnetic transition at 200 K when the field is applied along the ab-plane. a unique characteristic for a ferromagnet that likely arises from the interplay between the orientations of ferromagnetic domains and the direction of the applied field.

The disparity between zero field cooled (ZFC) magnetic volume susceptibility (χ_v) and field cooled (FC) χ_v becomes more pronounced below 125 K, particularly evident when H || c is applied, as illustrated in Figure 5.6(a). This phenomenon can be attributed to the blocking of ferromagnetic (FM) domains, lacking a preferred orientation, during ZFC measurements at low temperatures,

owing to diminished thermal fluctuations. However, as temperatures rise, these domains gradually become unpinned.

Above measurements indicate the alignment of the crystal's easy axis is along c-axis. This suggests that the bulk FGT crystal exhibits uniaxial magnetization, potentially leading to the formation of stripe or maze domains [148, 149]. To verify the formation of these domains, we performed SP-STM measurements, which we discuss in the next chapter 6. Additionally, they calculated the magnetocrystalline anisotropy (K) from the magnetization loops along the hard axis of the samples, yielding a value of 1.46×10^{6} J/m^{3}.

5.3 Summary

In summary, this chapter has provided insights into the properties of high-quality FGT samples grown via the chemical vapor transport method. Elemental composition analysis through EDX revealed a uniform distribution of elements within the crystal. Subsequently, the magnetic properties of FGT were thoroughly characterized using a QD-MPMS. The obtained magnetic volume susceptibility (χ_v) versus temperature (T) clearly confirmed FGT as a ferromagnetic material with a critical temperature (T_c) of 205 K. Furthermore, the dependence of χ_v on the direction of the applied magnetic field (H) was investigated. Notably, our collaborators observed that χ_v is 15 times larger when H is parallel to the c-axis compared to when it is parallel to the ab-plane, indicating that the magnetic easy axis aligns along the c-axis, highlighting the preference of Fe moments to orient along this direction.

Chapter 6

Study of Fe_3GeTe_2: Topography, Magnetic domains and Magnetic Skyrmions

Building upon the discussions regarding the growth, structural, chemical, and magnetic characterizations of Fe_3GeTe_2 (FGT) in the previous chapter 5, this chapter motivates to delve deeper into the explanation of its properties. Specifically, we aim to explore the intricate details of FGT through topographical examination via scanning tunneling microscopy (STM), as well as the investigation of magnetic domains, skyrmions and related properties utilizing spin-polarized scanning tunneling microscopy (SP-STM) equipped with antiferromagnetic tips.

By combining SP-STM measurements with density functional theory (DFT) calculations, we aim to resolve the spin-polarized density of states. Moreover, employing SP-STM enables us to achieve sub-nanometer resolution in measuring the domain-wall width and exchange stiffness of the sample. Subsequently, we integrate our experimental findings with atomistic spin-dynamics simulations grounded on exchange parameters derived from DFT computations. This comprehensive approach promises to provide a detailed understanding of the intricate properties of FGT at the nanoscale level.

6.1 Introduction

FGT, as an exceptional van der Waals (vdW) magnet, stands out for its diverse array of physical phenomena. Notably, bulk FGT showcases itinerant ferromagnetism characterized by a notably

high Curie temperature ($T_C \approx 230$ K) and a pronounced out-of-plane magnetic anisotropy [147, 150]. Research into electronic band theories and experimental investigations have shed light on the influence of strong electron correlations [151] and the fascinating physics of topological nodal lines [152] in bulk FGT. Particularly, measurements of electrical transport have revealed the presence of significantly large anomalous Hall currents [152] and topological Hall effects in FGT atomic layers [153]. These unique characteristics observed in FGT have ignited extensive interest and extensive research efforts focused on exploring their specific spin textures.

Recent studies have delved into the magnetic domains of FGT through the use of magnetic force microscopy (MFM), revealing the presence of "stripe-like bulk domains" and bubble-like domains at low temperatures [154, 155]. However, despite these insights, a comprehensive understanding of the microscopic domain structure, particularly the interrelation between different domain types, remains an area requiring further exploration. Various reports have documented a range of magnetic domain structures, including stripe domains, bubble domains, and skyrmions, all observed below the Curie temperature (T_c), with these observations facilitated by employing diverse techniques such as Lorentz transmission electron microscopy (Lorentz TEM) and scanning tunneling microscopy (STM) [142, 144, 145, 154, 156–159]. This highlights FGT as an optimal platform for investigating spin textures in two dimensions. In this chapter, we aim to delve into the observed results in bulk FGT crystal using SP-STM measurements.

6.2 Experimental Details and Observations

6.2.1 Scanning Tunneling Microscopy Measurements

In this section, we delve into the STM measurements conducted on FGT. Our measurements include observing various topographies and conducting scanning tunneling spectroscopy (STS) to analyze the density of states (DOS) of the sample. The STM measurements were carried out utilizing a home-built low-temperature STM operating at 0.7 K, controlled by a Nanonis system, within an ultra-high vacuum (UHV) environment of approximately 1×10^{-10} mbar. Subsequently, all captured STM images underwent processing using Nanotech WSxM [160].

FGT Bulk Crystal

Figure 6.1, shows different types of topographies that we have observed during STM scans. Figure 6.1 (a) depicts the presence of steps observed during STM scan. These steps exhibit a height of approximately half unit cell, equivalent to ≈ 0.8 nm (2×a). The appearance of step edges or

terraces on the surface of the material is a consequence of the arrangement of atoms in the crystal lattice. Figure 6.1 (b) representing atomic steps on the surface of FGT. Figure 6.1 (c) represents the flat region with some defects.

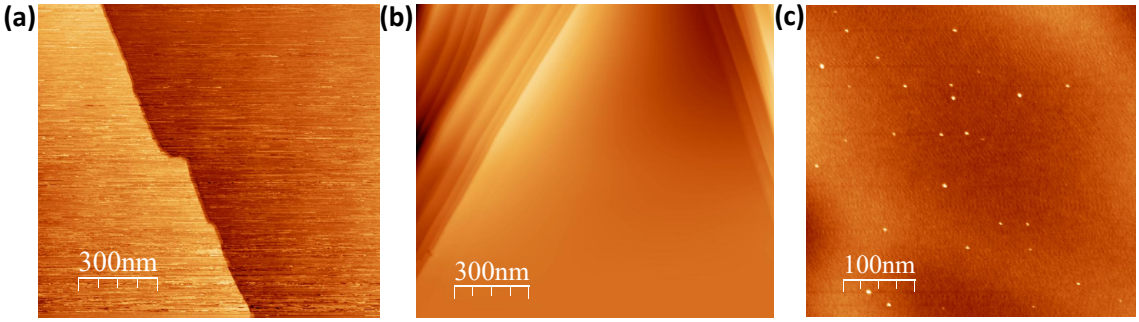

Figure 6.1: FGT topography showcasing (a) stepped regions (1.5 μm × 1.5 μm) (comprising half unit cell with step height (z) ≈ 0.8 nm), (b) region with atomic steps (1.5 μm × 1.2 μm), and (c) a flat surface (500 nm × 500 nm).

Atomic Resolution of FGT Surface

To investigate the atomic resolution of FGT, we conducted scans on small regions, as depicted in Figure 6.2. In Figure 6.2(a), we observed a flat region, with some areas displaying an atomic lattice, while others exhibited a rough surface likely due to irregular atomic arrangements or defects. After this initial scan, we focused on an area featuring prominent atomic lattice and performed a zoomed-in scan, as illustrated in Figure 6.2(b). Here, we observed the lattice arrangements of atoms. Subsequently, we revisited the same area and conducted a slow scan to confirm the presence of atoms, alongside the observation of some defects, as shown in Figure 6.2(c).

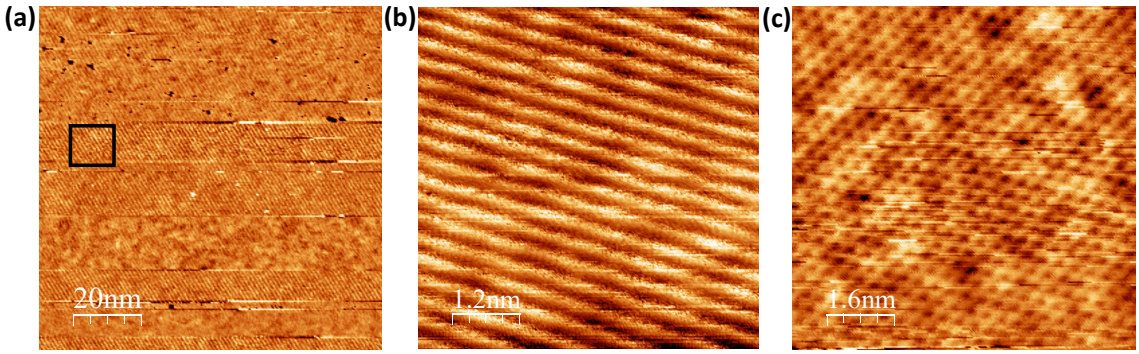

Figure 6.2: FGT topography displaying (a) a flat region with atomic lattice stripes (100 nm × 100 nm), (b) a zoomed-in view of the atomic lattice (6 nm × 6 nm) as depicted in the square box of (a), and (c) Atomically resolved image of FGT surface with some corrugations originate from the Fe deficiency (8 nm × 8 nm), covering the same area as (b) and obtained with a very slow scan.

Buckled Structures in FGT

During several scans of FGT, we observed stripes and ripples on the surface, indicative of a buckled structure, where the material's atomic layers deviate from a flat, planar arrangement due to strain, curvature, or other external factors. Buckling can occur in various 2D materials [161], such as graphene [162, 163] and transition metal dichalcogenides (TMDs) [164, 165], often induced by factors like thermal expansion mismatch, substrate interactions, or mechanical deformation. These structures significantly influence electronic, optical, and mechanical properties, crucial for diverse applications [166–168]. Understanding and controlling the 2D buckling mode are crucial for designing nanoscale devices. Surface roughness, atomic steps, defects, and adsorbates contribute to stripes and ripples observed in STM topography. Unevenness, atomic steps, and structural defects introduce variations, while adsorbates or contaminants induce distinct patterns.

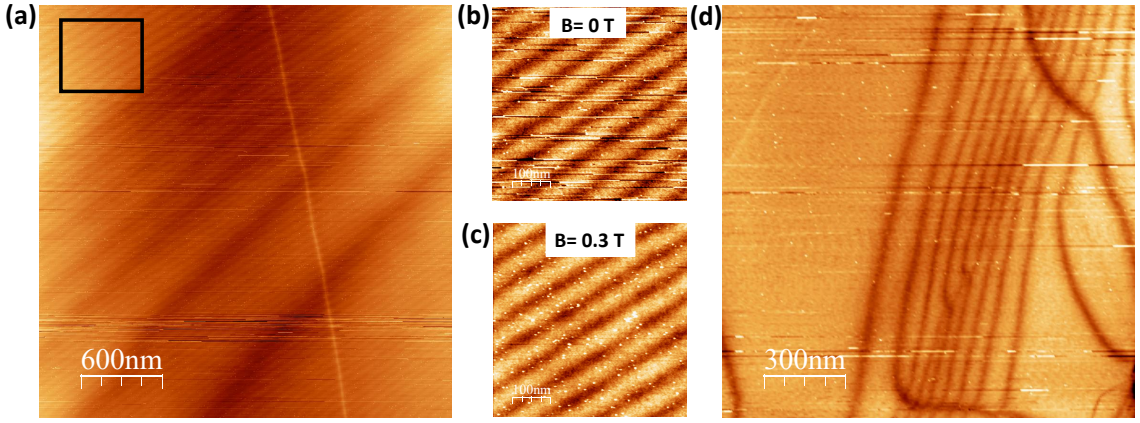

Figure 6.3: (a) Parallel stripes alongside ripples observed on the surface of FGT (3 μm $\times$ 3 μm). The stripes are depicted in a magnified rectangular box, as shown in (a), under an applied magnetic field of (b) 0 T (500 nm $\times$ 500 nm) and (c) 0.3 T (500 nm $\times$ 500 nm) perpendicular to the sample surface. (d) Scan demonstrating the presence of a flat region accompanied by periodic stripe and ripple formations (1.5 μm $\times$ 1.5 μm).

In Figure 6.3(a), periodic stripes along with ripples are observed. To investigate whether these stripes originate from magnetic effects or are solely topographical in nature, we selected a small region outlined by a black box. Subsequently, we conducted scans on this zoomed-in area, as depicted in Figure 6.3(b), both without any applied magnetic field and with a magnetic field of 0.3 T, as shown in Figure 6.3(c). Interestingly, we observed that these stripes remained unaffected by the magnetic field, indicating their origin as buckled structures rather than magnetic in nature. Additionally, we conducted scans on another area, illustrated in Figure 6.3(d), which revealed the coexistence of ripples and stripes alongside a flat surface, further confirming the presence of

buckled structures.

6.2.2 Scanning Tunneling Spectroscopy

In STM measurements, the dI/dU spectra provide information about the local density of electronic states (LDOS) at the sample surface. By measuring the tunneling current as a function of bias voltage, dI/dU spectra reveal the energy-dependent electronic structure of the surface, including features such as energy levels, bandgaps, and localized electronic states. This information helps characterize the electronic properties and surface morphology of the sample under investigation.Tunneling spectra were obtained employing a standard lock-in technique with root-mean-square bias voltage modulation (U^{rms}_{mosd}) set at 10 mV at 1.08 kHz.

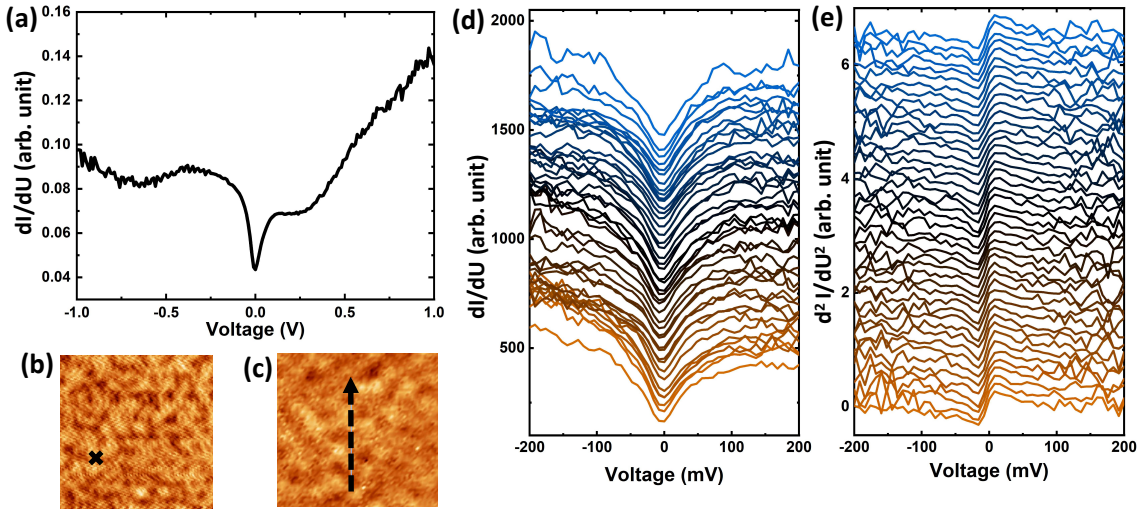

Figure 6.4: (a) dI/dU tunneling spectra acquired at a cross point highlighted within the scan area (20×20 nm^2) as depicted in (b), recorded at 1 V, 1 nA, and U^{rms}_{mod}=10 mV. (d) dI/dU spectra and (e) d^2I/dU^2 spectra measured simultaneously along the line illustrated in (c) topographic scan (10×10 nm^2) at 200 mV, 1 nA and U^{rms}_{mod} = 10 mV.

Figure 6.4 illustrates the outcomes of STS measurements conducted within this study. In Figure 6.4(a), dI/dU tunneling spectra are depicted, averaged over 50 sweeps, acquired at a single point situated on a small flat area of the sample, as illustrated in Figure 6.4(b). These spectra reveal a dip at the Fermi level, a characteristic feature often associated with inelastic tunneling events when tunneling into ferromagnets, involving the excitation of spin-waves or magnons [51, 56, 57, 169]. To delve deeper into this phenomenon, additional spectra were obtained along a line on the flat surface, as depicted in Figure 6.4(c), with each spectrum averaged over 50 sweeps. Figure 6.4(d) exhibits the dI/dU spectra, while Figure 6.4(e) showcases the corresponding d^2I/dU^2 spectra acquired simultaneously. Notably, Figure 6.4(d) unveils distinct steps and dips at the Fermi level,

whereas Figure 6.4(e) portrays peak-dip pairs, providing convincing evidence of inelastic events. Subsequent measurements with a spin-polarized tip will be conducted in the upcoming section to further verify the presence of these dips.

6.2.3 Spin Polarized-STM Measurements

SP-Maps at Different Magnetic Fields

In the initial phase of our investigation, we directed our attention towards examining the magnetic contrast and spin polarization characteristics of states existing above the surface. Utilizing spin-polarized scanning tunneling microscopy (SP-STM) with a Cr-coated W tip possessing out-of-plane sensitivity at a Cr coverage below 50 monolayers [170], we mapped the magnetic domains at the FGT surface. Figure 6.6(b) illustrates topographic SP-STM images revealing subtle domains on the FGT surface, attributed to the tunneling magnetoresistance (TMR) effect [171] which slightly alters the tunneling probability, impacting the z-position in the constant current feedback mode [172, 173].

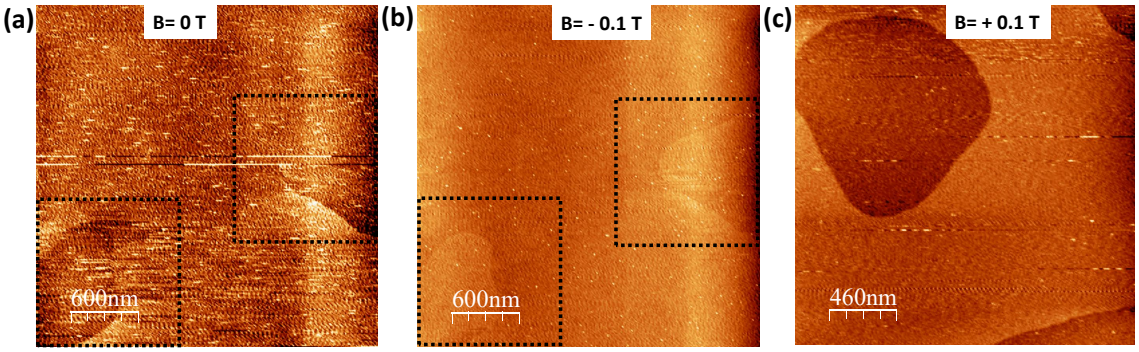

Figure 6.5: SP-STM images depicting FGT topography of magnetic domains captured at (a) 0 T, (b) −0.1 T, and (c) 0.1 T. The scale bar represents 600 nm for (a) and (b) while 460 nm for image (c). Imaging conditions: sample bias voltage (U) set to 200 mV, tunneling current (I) maintained at 50 pA.

Figure 6.5 presents the initial findings of SP-measurements, showcasing features suggestive of magnetic domains, as highlighted in the square boxes in Figure 6.5(a) acquired under zero magnetic field. To validate their magnetic nature, a magnetic field of -0.1 T was applied, resulting in the observed shrinkage of these features from their original size, as depicted in the square boxes in Figure 6.5(b), providing evidence of their magnetic origin. Furthermore, to assess the response of these features to the opposite direction of the magnetic field (+0.1 T), particular attention was paid to the bottom left feature as a reference point. Notably, a remarkable expansion in size of this feature was observed, as depicted in Figure 6.5(c), providing conclusive evidence that these

features indeed correspond to magnetic domains. Additionally, we achieved successful preparation of the spin-polarized tip with out-of-plane magnetization.

Upon confirming the magnetic nature of these domains, we proceeded to optimize the imaging parameters to enhance the contrast of these features. Through various examinations, we determined that the domains exhibited the most distinct contrast at bias voltage values of -500 mV and +500 mV. Consequently, all subsequent mappings were conducted at a bias voltage of -500 mV. With the bias voltage value fixed, our focus shifted towards conducting differential conductance mapping of these magnetic domains.

Differential conductance (dI/dU) mapping of magnetic domains provides valuable insights into the electronic properties of the material within these domains. By analyzing the variations in conductance across different regions of the sample, we can elucidate the local density of electronic states (LDOS) associated with the magnetic domains. This technique allows for the visualization and characterization of spatial variations in electronic structure, offering crucial information about the distribution and behavior of electrons within the material. dI/dU mapping can also reveal important details about the energy levels, band structure, and magnetic properties of the sample, providing a deeper understanding of its electronic behavior and facilitating the investigation of phenomena such as spin polarization, magnetic ordering, and quantum confinement effects. To record dI/dU maps, we utilized a lock-in amplifier and adjusted the modulation voltages at a specific frequency to obtain the most prominent contrast of these domains. Following careful adjustments and optimizations of all parameters, we conducted our primary measurements.

We utilized Figure 6.5(c) as a baseline reference image of the magnetic domains and conducted various optimizations to enhance the contrast in dI/dU mapping, although at the expense of sacrificing the topographic resolution of these domains. The uppermost images in Figure 6.6(a) and (b) depict a faint signal in the STM topography and the maximum contrast achieved in the dI/dU mapping, respectively, obtained at a magnetic field strength of +0.1 T. Following this optimization, we commenced our measurements by gradually decreasing the magnetic field strength from 0.1 T to 0 T. The resultant topography and dI/dU maps, showcased in the middle images of Figure 6.6(a) and (b), reveal a reduction in the size of dark domains and an expansion in the size of bright domains. Subsequently, we further decreased the magnetic field from 0 T to -0.1 T, yielding the corresponding topography and dI/dU maps depicted in the bottom images of Figure 6.6(a) and (b). Notably, these images exhibit a further reduction in the size of dark domains and an enlargement in the size of bright domains.

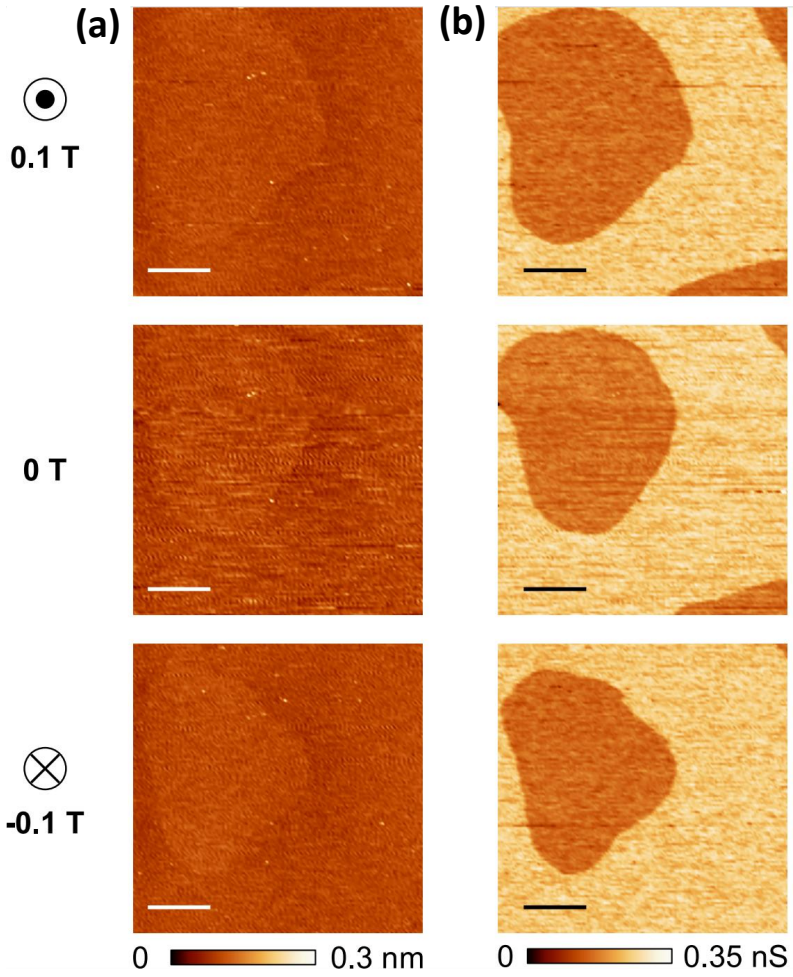

Figure 6.6: (a) STM images of FGT at 0.1 T (upper), 0 T (middle), and −0.1 T (lower panel). (b) dI/dU maps taken simultaneously with (a). Scale bar indicates 500 nm. Imaging conditions: sample bias voltage (U) : −500 mV, tunneling current (I) : 50 pA, and modulation voltage (U_{mod}^{rms}) : 80 mV.

Moreover, upon analyzing the three images obtained under different perpendicular magnetic fields (0.1 T, 0 T, and −0.1 T), a significant alteration in the domain size was observed, affirming that the observed contrast indeed stems from magnetic effects. The corresponding differential conductance (dI/dU) maps in Figure 6.6(b) depict a more pronounced Tunneling Magnetoresistance (TMR), directly reflecting the differential conductance. A binary contrast, represented as dark and bright orange, emerges, elucidating the out-of-plane easy axis of the material. This results in up and down magnetized domains of approximately 1 μm size, visualized using the out-of-plane sensitive Cr-coated W tips.

Analogous to the topographic image of the domains, the contrast in differential conductivity

provides a clearer depiction of the magnetic field's impact on the domains. Dark domains, magnetized upwards, contract, while bright domains expand when the magnetic field is ramped to negative values. Notably, the spin contrast remains consistent between two opposite magnetic field polarities, suggesting that the applied magnetic field does not influence the tip spin-polarization [174] or the sample magnetization axis. In essence, the local easy axis of magnetization is confirmed to be perpendicular to the FGT surface.

6.2.4 Spin-Polarized Scanning Tunneling Spectroscopy

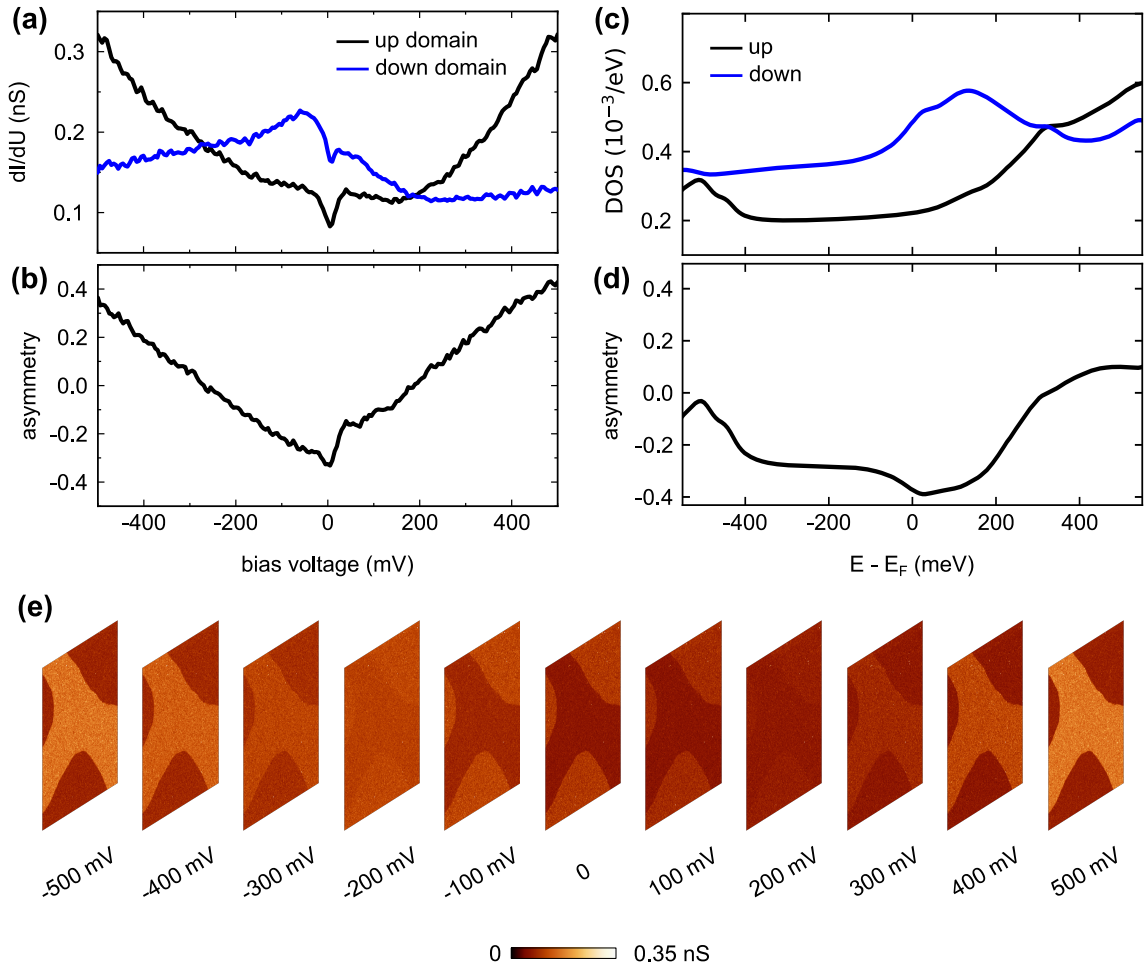

Figure 6.7: (a) Tunneling spectra of spin-up (black) and -down (blue) domains. (b) Asymmetry derived from (a). (c) Vacuum density of states calculated from DFT for a distance of 4.28 Å above the surface Te atoms. (d) Asymmetry derived from (c). (e) dI/dU maps acquired using spectroscopic imaging from −500 to 500 mV with an increment of 100 mV. Image size: 2.3×2.3 μm^2. Measuring conditions: (a, b) $B = -0.29$ T, $U = -500$ mV, $I = 50$ pA, and $U_{mod}^{rms} = 10$ mV, (c) $B = 0.15$ T, $U = -500$ mV, $I = 100$ pA, and $U_{mod}^{rms} = 40$ mV.

Spin-Polarized Spectra of Magnetic Domains

In Figure 6.7(a), spin-polarized tunneling spectra taken at the spin-up and spin-down domains are represented by black and blue curves, respectively. Within a central bias voltage range of approximately −250 meV to +200 meV, the down domain exhibits higher differential conductivity compared to the up domain. The calculated asymmetry, derived from the difference in the dI/dU signal for up and down domains divided by their sum, is presented in Figure 6.7(b), revealing a negative asymmetry within the mentioned bias regime and sign changes at voltages below and above.

Comparisons were made between the measured asymmetry and LDOS calculated from first principles, done by our theoretician collaborators Prof. Dr. Yuriy Mokrousov along with their group members Philipp Rüßmann, Markus Hoffmann and Dongwook Go, as illustrated in Figure 6.7(c). The density functional theory (DFT)-calculated LDOS, considering the exchange-correlation functional within the local density approximation (LDA) and the experimental lattice constant [146], showed agreement with the SP-STS results. The spin-up LDOS exhibited a minimum around the Fermi level (E_F), while the down spin channel displayed a peak close to E_F. Figure 6.7(d) depicts the corresponding asymmetry, demonstrating a similar overall dependence on bias voltage but systematically shifted to more negative values.

Experimental spectra obtained from both spin-up and spin-down domains exhibited a distinct local minimum precisely at the Fermi energy, a phenomenon also observed in non-spin-polarized measurements, as previously discussed. This dip formation at the Fermi level suggests the occurrence of inelastic events within the material. However, it is noteworthy that these inelastic effects were absent in the corresponding Density Functional Theory (DFT) calculations. A more comprehensive analysis and detailed discussion of these spectral features will be presented in the subsequent chapter 7. Moreover, Figure 6.7(e) illustrates the domain contrast in dI/dU at various bias voltages, which correlates with the asymmetry observed in the Spin-Polarized Scanning Tunneling Spectroscopy (SP-STS) measurements, exhibiting a reversal at bias voltages of $U = 200$ mV and $U = -250$ mV.

Complementary to the STM measurements, our study of FGT DFT calculations, focusing on both thin film and bulk crystal scenarios. The results, summarized in Table 6.1, highlight the impact of varying exchange correlation function parametrizations (generalized gradient (PBE) and local density approximations (LDA)) and lattice parameters on the average spin moment of Fe atoms. The decrease in the average Fe moment with LDA usage and lattice compression is consistent

with previous data and aligns with experimentally observed values. This decrease, attributed to the typical underestimation of the lattice parameter for the LDA functional, corresponds with prior calculations [175].

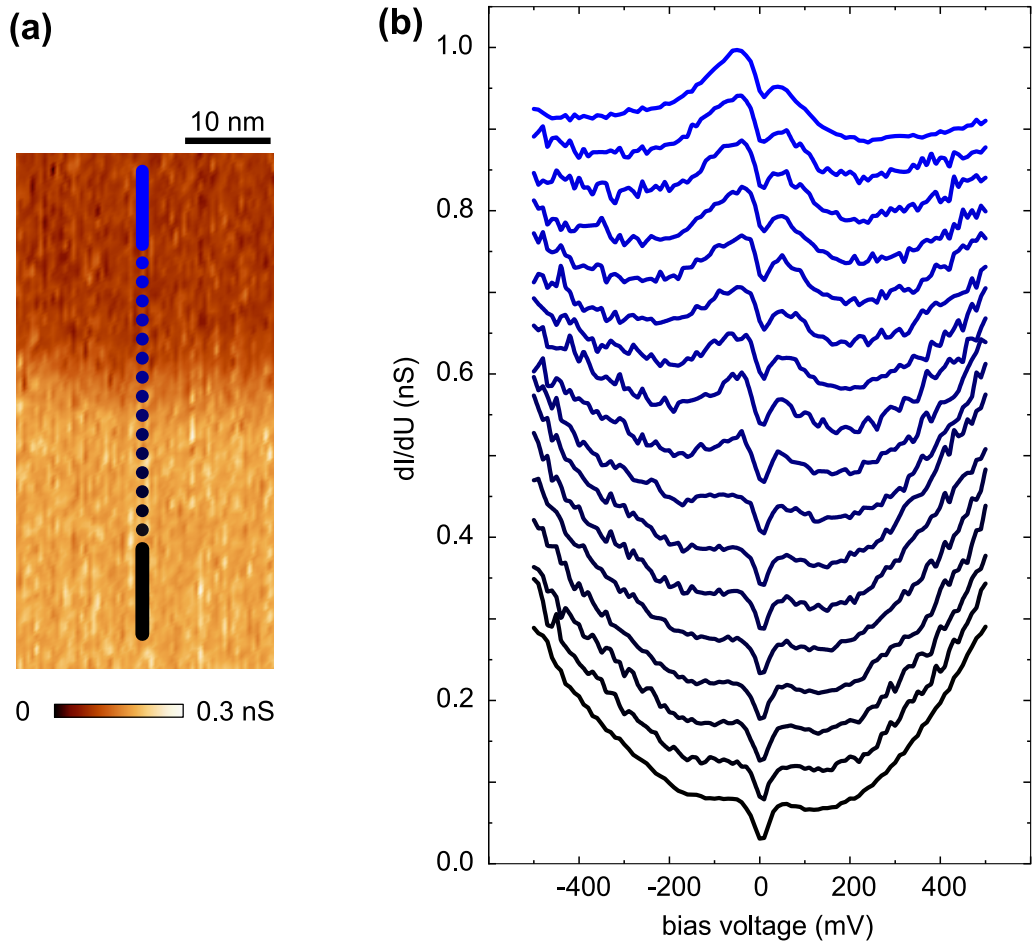

Figure 6.8: (a) Tunneling spectra of spin-up (black) and -down (blue) domains. (b) Asymmetry derived from (a). (c) Vacuum density of states calculated from DFT for a distance of 4.28 Å above the surface Te atoms. (d) Asymmetry derived from (c). (e) dI/dU maps acquired using spectroscopic imaging from −500 to 500 mV with an increment of 100 mV. Image size: 2.3×2.3 μ m^2. Measuring conditions: (a, b) B = −0.29 T, U = −500 mV, I = 50 pA, and U_{mod}^{rms} = 10 mV, (c) B = 0.15 T, U = −500 mV, I = 100 pA, and U_{mod}^{rms} = 40 mV.

Spin-polarized Spectra Across Magnetic Domain Wall Boundary

Our focus now shifts to the examination of the domain wall structure. In Figure 6.8(a), a detailed image of a magnetic domain boundary is presented, showcasing a smooth variation in spin contrast between the saturated signals in the adjacent domains. The dotted line denotes the positions where spectra in Figure 6.8(b) were acquired, with vertically offset spectra for clarity. The elongated lines at both ends of the dotted line trace the areas for the averaged spectra of the dark (first curve from the

top) and bright (last curve at the bottom) domains. In the transition region between the spin-down and spin-up domains, the spectra smoothly evolve without the emergence of additional features inside the domain wall. This observation suggests that as magnetization smoothly rotates between the domains, no additional electronic states are generated within the domain wall. Consequently, there exists a flawless transition in the electronic structure with opposite magnetization directions, indicating the absence of edge states.

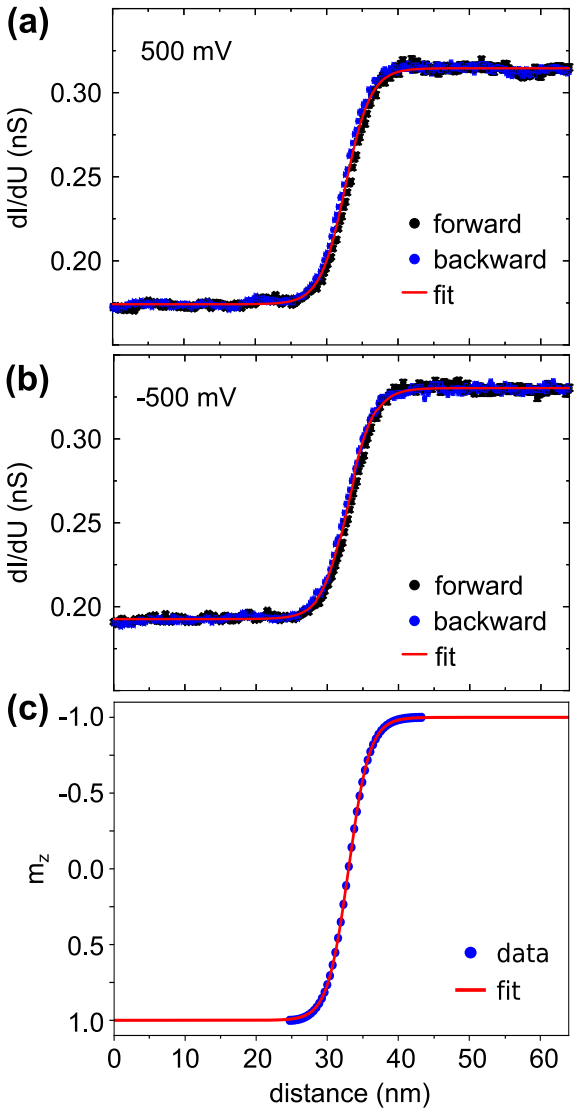

Figure 6.9: Averaged dI/dU line scans of the domain wall at zero magnetic field at voltages of (a) 500 mV and (b) −500 mV. Black and blue data corresponds to forward and backward scans respectively. The red curves present the fitted results. Measuring conditions: I = 100 pA, and U_{mod}^{rms} = 100 mV. (c) Domain-wall profile from atomistic spin-dynamics simulations using DFT-calculated exchange parameters.

6.2.5 Domain Wall Width Calculations

The magnetic domain wall width refers to the spatial extent over which the orientation of magnetic moments transitions from one direction to another within a magnetic domain wall. It represents the region where the magnetization direction undergoes a gradual change, typically ranging from nanometers to micrometers in width, depending on the material and external conditions. The study of domain wall width contributes to our understanding of magnetic stability and dynamics. It is a crucial parameter in understanding the magnetic properties of materials and plays a significant role in various magnetic phenomena and applications.

The precise measurement of the domain wall profile is facilitated by the relatively low noise in the differential conductance and the use of an antiferromagnetic tip. Figure 6.9(a) and 6.9(b) exhibit fully resolved wall profiles at $U = 500$ mV and -500 mV, respectively. Forward and backward scans (black and blue curves, respectively) show no significant differences, emphasizing the absence of magnetic interaction between the tip and the wall that could potentially influence the scanning process. The averaged profile, fitted with a hyperbolic tangent function (red curves), aligns with the micromagnetic description of a domain-wall profile for Bloch walls in bulk materials with uniaxial anisotropy [148]. The fitting equation is expressed as follows:

$$\frac{\mathrm{d}I}{\mathrm{d}U}(x) \propto \tanh \frac{2x}{w}, \tag{6.1}$$

Here, x represents the profile distance, and w denotes the domain-wall width. The fitted curves faithfully reproduce the shape of the domain wall, indicating that at the surface, the wall profile adheres to that of a conventional Bloch wall, and no Néel-caps are present at the surface. The absence of Néel-caps is crucial, as their presence would result in asymmetric wall profiles significantly deviating from the simple analytic wall shape [176, 177]. From the fitted curves, we extract a domain width of 7.11 ± 0.03 nm and 7.32 ± 0.02 nm for $U = 500$ mV and -500 mV, respectively.

Domain Wall Width as a Function of Magnetic Field and Electric Field

The calculation of w initially carried under a zero magnetic field condition. Subsequently, we calculated and examined w values across a range of magnetic field strengths, from 0.2 T to -0.2 T, incrementing or decrementing in intervals of 0.1 T. These evaluations were conducted under two distinct bias voltage conditions: 500 mV and -500 mV, respectively. Figure 6.10 depicts the variation of w under different magnetic field strengths. These data points are derived from the calculated averaged values obtained through forward and backward scans of the differential

conductance mapping of the domain wall profile, acquired at bias voltages of 500 mV and -500 mV, respectively.

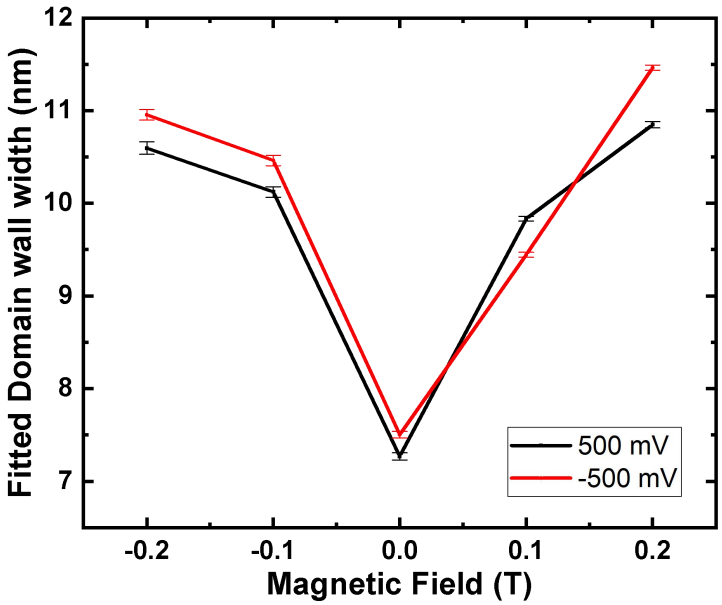

Figure 6.10: Averaged domain wall width at various ranges of magnetic field taken at 500 mV and −500 mV.

In the case of 500 mV, the black curve illustrates that w strongly depends on the magnetic field as it increases with the rise in applied magnetic field strength in both directions. Similarly, for -500 mV, the red curve demonstrates a similar trend of increment as observed at 500 mV. Although there are slight differences in the values between the two bias voltages, there is no significant divergence noted under different electric field conditions.

6.2.6 Exchange Stiffness (A) Calculations

The exchange stiffness coefficient (A), quantifies the intensity of direct exchange interactions among neighboring spins. This parameter plays a crucial role in shaping various magnetic phenomena, including the formation of skyrmions, behavior of magnetic vortices, width of magnetic domain walls, and the exchange length. To obtain these crucial insights, we have calculated the value of A. Furthermore, for comparison, we have included the A value derived from neutron scattering measurements, and additionally computed A using parameters obtained from DFT calculations.

Calculation of A from STM Data

The domain-wall width w provides insights into the exchange stiffness A and the uniaxial anisotropy constant K, expressing a relationship as follows:

$$w = 2\sqrt{\left|\frac{A}{K}\right|}. \tag{6.2}$$

By substituting the domain wall width (w) value, approximately 7 nm as discussed in the preceding section, and the uniaxial anisotropy, calculated as 1.46×10^6 J/m^3 from the SQUID measurements, into the above relation, we computed the value of A to be 18.4 pJ/m.

Calculation of A from Neutron Scattering Data

To compare the values of A obtained from our STM measurements with those from neutron scattering measurements [98], we utilized relation (6.3), substituting the spin wave D value from [98] and the saturation magnetization M_S value from [154].

$$A = \frac{\pi^2 M_s D}{2g\mu_B} \tag{6.3}$$

This calculation yielded a value of A equal to 11.8 pJ/m, which closely aligns with our experimentally derived value of 18.4 pJ/m. This demonstrates a strong agreement between the data obtained from STM and neutron scattering techniques.

6.3 DFT and Spin-Dynamics Calculations

Our collaborative team led by Prof. Dr. Yuriy Mokrousov, along with group members Philipp Rüssmann, Markus Hoffmann, and Dongwook Go performed DFT calculations for a thin film of FGT consisting of three FGT layers using the experimental lattice constant [178]. They perform the calculations with the JuKKR code [179] that implements the full-potential relativistic Korringa-Kohn-Rostoker Green function method (KKR) [180] with an exact description of the shape of the atomic cell [181, 182]. We use an angular momentum cutoff of $\ell_{\max} = 3$ and the local density (LDA) and generalized gradient approximations (GGA) to the exchange-correlation potential [183, 184]. Their calculations of the exchange coupling constants for the extended Heisenberg Hamiltonian are based on the method of infinitesimal rotations [185, 186].

Based on the DFT calculations, various parameters for the extended classical Heisenberg Hamiltonian describing the interaction of spins $\vec{S}_i = \vec{M}_i/\mu_i$ ($\mu_i = |\vec{M}_i|$) located at lattice sites i were computed.

$$
\begin{aligned}
H = & - \sum_{\langle ij \rangle} J_{ij} \left(\vec{S}_i \cdot \vec{S}_j \right) - \sum_{\langle ij \rangle} \vec{D}_{ij} \cdot \left(\vec{S}_i \times \vec{S}_j \right) \\
& - \sum_i K (\vec{S}_i \cdot \hat{\vec{e}}_z)^2 - \sum_i \mu_i \vec{B} \cdot \vec{S}_i \\
& - \frac{\mu_0}{8\pi} \sum_{i \neq j} \frac{3 \left(\vec{S}_i \cdot \hat{\vec{r}}_{ij} \right) \left(\vec{S}_j \cdot \hat{\vec{r}}_{ij} \right) - \vec{S}_i \cdot \vec{S}_j}{r_{ij}^3} ,
\end{aligned} \tag{6.4}
$$

The terms J_{ij} and $\vec{D}_{ij}$ represent the isotropic and antisymmetric exchange interactions, respectively, also known as the Dzyaloshinskii-Moriya interaction. The third and fourth terms incorporate contributions originating from on-site anisotropy K, the Zeeman energy induced by an external magnetic field $\vec{B}$, and the dipolar contribution.

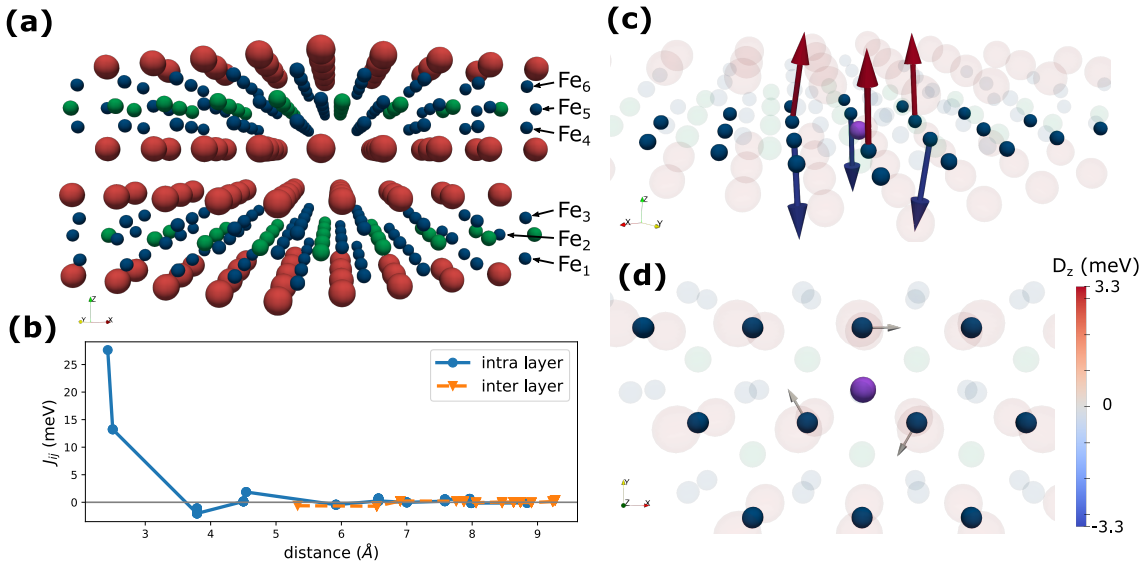

Figure 6.11: (a) Crystal structure of Fe_3GeTe_2 where the six different Fe layers in the unit cell are marked with labels "Fe_1" to "Fe_6". (b) Exchange coupling constants J_{ij} vs. distance between the Fe atoms (intra-layer coupling only between Fe_1, Fe_2 and Fe_3, inter-layer coupling for $i \in [1, 2, 3]$ and $j \in [4, 5, 6]$). (c) $\vec{D}_{ij}$ for pairs of Fe_1-Fe_1 and (d) for Fe_1-Fe_2 where the DMI vector is shown at the position of atom j and atom i is highlighted by the purple sphere.

Figure 6.11(a) show the alternating layers of the FGT lattice where the six different Fe atom layers are labelled Fe_1 to Fe_6. The calculated exchange interactions (J_{ij}) are shown as a function of the distance between the Fe atoms in figure 6.11(b). The data is shown for the smallest lattice constant (5% compressed compared to the experimental lattice constant) where the computed average Fe moment is smallest and agrees best with the experiment (cf. Tab. 6.1). The large spread in the experimental values of the average magnetic moment could be the result of varying Fe

content and increasing c/a ratio in different samples [187]. They find strong ferromagnetic inter-layer couplings at small distances which decay with additional sign changes to antiferromagnetic ($J_{ij} < 0$) coupling at larger Fe-Fe distances. The Dzyaloshinskii-Moriya interactions (DMI) are only significant for inter-layer couplings. As shown in figure 6.11(c), the largest DMI is found for nearest neighbor Fe_1-Fe_1 pairs, with vectors mainly pointing in the direction perpendicular to the FGT film and alternating in the sign for adjacent neighbors. The pairs in the Fe_3-Fe_3 layer are related by mirror symmetry and the DMI therefore exactly cancels the contributions from Fe_1-Fe_1. The second-largest contribution comes from nearest neighbors between Fe_1 and Fe_2 atoms (or the symmetry equivalent Fe_3-Fe_2 pairs) as shown in figure 6.11(d). All other DMI pairs are smaller by at least an order of magnitude.

Table 6.1: Average Fe spin moment of bulk Fe_3GeTe_2 with the corresponding lattice parameters. The theory (DFT) results are given for the PBE and LDA exchange correlation functionals where the same lattice parameter as in Ref. [146] was used. The labels "LDA*" and "LDA**" indicate the calculations where the lattice parameters are taken for 3% and 5% isotropic compressive strain, respectively. Experimental values are given for comparison (the numbers in parentheses for Ref. [187] indicate the nominal Fe content per formula unit of two different samples).

Method		a (Å)	c (Å)	$\langle\mu_{Fe}\rangle$ (μ_B)
Theory	PBE	3.991	16.333	2.12
(this work)	LDA	3.991	16.333	1.99
	LDA*	3.871	15.840	1.69
	LDA**	3.791	15.514	1.46
Experiment	Ref. [146]	3.991	16.333	1.20
	Ref. [188]	3.991	16.296	1.80
	Ref. [187] (2.8)	3.956	16.395	1.08
	Ref. [187] (3.0)	4.018	16.334	1.32

6.3.1 Computing A and w from DFT Parameters

The micromagnetic spin stiffness and spiralization vectors

$$A = \frac{1}{2V}\sum_{j>0} R_{0j}^2 J_{0j}\,, \tag{6.5}$$

$$\vec{D} = \frac{1}{V}\sum_{j>0} R_{0j}\vec{D}_{0j}\,, \tag{6.6}$$

where V is the volume per Fe atom, can be calculated from the atomistic exchange parameters [189]. These parameters define the micromagnetic energy functional

$$E[\vec{m}] = \int \mathrm{d}\vec{r}\left[A\left(\dot{\vec{m}}\right)^2 + \vec{D}\cdot\left(\vec{m}\times\dot{\vec{m}}\right) + Km_z^2\right] \tag{6.7}$$

Table 6.2: Exchange stiffness (A), anisotropy (K) and resulting micromagnetic ($w_{\text{micro}} = 2\sqrt{|A/K|}$) and atomistic ($w_{\text{atom}}$) domain-wall widths for bulk Fe_3GeTe_2 with different lattice parameters (cf. Tab. 6.1). The FM/AFM label indicates whether antiferromagnetic or ferromagnetic ordering is found between the FGT layers. w_{atom} is the result of atomistic spin dynamics simulations using the Spirit code with the respective set of exchange coupling parameters.

Method	A (meV nm/Fe)	A (pJ/m)	K (meV/Fe)	K (MJ/m^3)	w_{micro} (nm)	w_{atom} (nm)
LDA (AFM)	3.248	13.859	−0.506	−2.16	5.067	5.489
LDA* (AFM)	2.403	11.237	−0.263	−1.23	6.046	6.094
LDA** (FM)	1.772	8.818	−0.180	−0.897	6.274	5.927

for a continuous magnetization field $\vec{m}[\vec{r}]$ with $\dot{\vec{m}} = \nabla\vec{m}[\vec{r}]$. The crystal symmetries of the FGT layers and the structure of the calculated DMI vectors lead to vanishing spiralization $\vec{D}$. The computed spin stiffness A, the anisotropy K and the resulting micromagnetic domain-wall width (eq. 6.2) are summarized in Tab. 6.2. The parameters are shown for three calculations using the experimental lattice constant as well as for 3% and 5% smaller lattice parameters. One can see that the spin stiffness as well as the anisotropy get smaller with smaller lattice constant which matches the observed decrease in the average Fe moment. The micromagnetic domain-wall width on the other hand increases from 5 to 6.3 nm which is close to the measured domain-wall width of around 7 nm.

They further use the atomistic exchange parameters in spin-dynamics simulations. They consider a $50 \times 5 \times 2$ supercell and find the magnetic ground state starting from random spin orientations (see Methods for details). For the experimental lattice constant and the calculation with 3% compressive strain we find antiferromagnetically coupled FGT layers, in contrast to experimental findings but in agreement with previous theoretical results [175]. Only when the FGT lattice is compressed by 5% we find ferromagnetically coupled FGT layers. They furthermore calculate the domain-wall width by pinning the left and right end of the supercell to point in $\pm z$ direction (i.e. parallel to the surface normal of the FGT layers). This creates a domain wall in the center of the supercell. They fit the resulting domain-wall profile (shown in figure 6.9(c)) using eq. (6.1). The fitted domain-wall width is shown in Tab. 6.2 where they observe that the atomistic domain-wall width agrees well with the micromagnetic parameters and in particular also the experiment.

6.4 Skyrmion in Bulk FGT

Various reports have documented the emergence of various topological spin textures or skyrmions, including Bloch-type [145, 157, 190, 191] and Néel-type [144, 156, 158, 159], within FGT, yet their

origin remains a challenging matter. The presence of Néel-type spin textures in FGT is unexpected, given that their formation typically relies on a positive Dzyaloshinskii-Moriya interaction (DMI), which conflicts with FGT's centrosymmetric space group and implies a zero DMI according to its crystal structure. Furthermore, the stabilization of these textures in the FGT crystal cannot be solely attributed to DMI, as it does not persist in the long-wavelength limit [192].

The origin of DMI in FGT remains a key issue, with recent investigations exploring potential mechanisms for its induction within the FGT crystal and interfaces [156]. It has been suggested that the spontaneously formed oxidized layer on the FGT surface under ambient conditions may trigger interfacial DMI, leading to the formation of Néel-type skyrmions under current pulses [156]. Other critical factors include the thickness of the flake [193, 194], which significantly influences domain configurations, and the applied magnetic field protocol [144], determining different domain structures. Research efforts have primarily focused on stabilizing and manipulating topologically protected magnetic structures, such as skyrmions, driven by their potential applications in spintronic devices and emerging physics. Despite numerous publications on domain formation in FGT, many aspects, including underlying physical mechanisms and conditions for the emergence of non-trivial domain patterns like circular skyrmion-like domains, remain unclear or contradictory.

The out-of-plane domain walls, including their 180° domain walls, essentially form bubble domains [145], where the sense of rotation within the wall remains consistent. Singularities in the form of Bloch lines and cusps in the wall would occur with a change in the sense of rotation [195], which we do not observe. Specifically, the sense of rotation of the 180° domain wall between the central domain of the bubble and its surroundings remains unchanged within the domain wall of the bubble. In this context, the bubble domains are topologically equivalent to skyrmions, carrying a topological charge based on the winding of the magnetization and are protected from transitioning to the trivial, single-domain ferromagnetic state. It's important to note that with SP-STM, we measure only one component of the magnetization (in the z-direction), thus unable to determine the sense of rotation of the wall.

6.4.1 Field-Dependent Skyrmion Size

To explore the topological robustness of bubble domains, we analyzed their response to significant out-of-plane magnetic fields, related to the investigations conducted by Ding et al. using Lorentz transmission electron microscopy on thin FGT flakes [145]. Figure 6.12(a) depicts the transformation of individual and multiple μm-sized bubble domains as the magnetic field compresses them. With increasing magnetic field strength, the initially irregularly shaped bubble domain undergoes

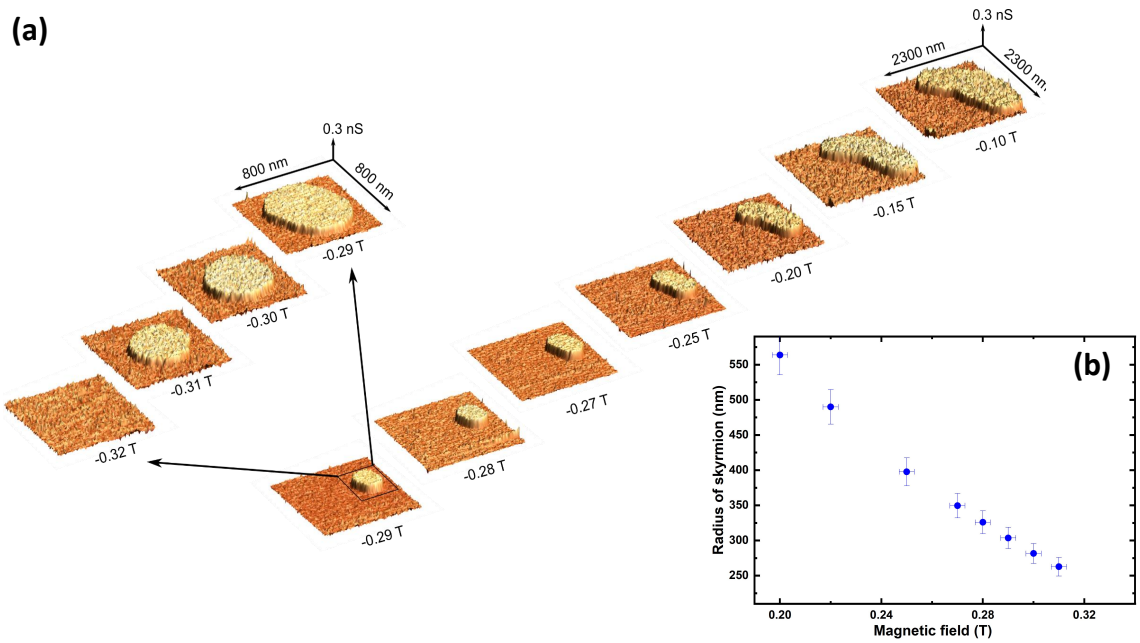

Figure 6.12: (a) Pseudo three-dimensional representation of the dI/dU maps under various of magnetic fields. (b) Radius of the skyrmionic bubble as a function of magnetic fields. Measuring conditions: $U = -500$ mV, $I = 50$ pA, and $U_{mod}^{rms} = 80$ mV.

compression, eventually adopting a circular shape of sub-μm size (at -0.3 T). This compression continues [196–198] until a sudden collapse occurs between 0.31 T and 0.32 T.

6.4.2 Calculation of Critical Annihilation Magnetic Field Value

Simple continuum theory predicts that the lateral size of a topologically protected skyrmion should be proportional to $\frac{1}{B}$ [199, 200]. In Figure 6.12(b), the effective radius r_{eff} of the bubble ($r_{\text{eff}} = \sqrt{\text{area}/\pi}$) is plotted against the magnetic field. It is observed that the effective radius of the bubble monotonically decreases with increasing magnetic fields until it reaches around 262 nm before vanishing. This highlights that relatively large bubbles can be adequately described by a continuum model. They are compressed but do not shrink to atomic sizes before collapsing, indicating that they become energetically unstable rather than collapsing to a singularity. However, their behavior does not adhere strictly to the simple $\frac{1}{B}$ relationship but instead shrinks slower than expected at high fields.

From the paper [198], we have used their method to solve and calculate the critical value of magnetic field at which the magnetic bubble skyrmion annihilated. The magnetic solitons, an another term to represent the magnetic bubble, consists of the topological soliton energy $E_s[\theta(\rho)]$ comprises five terms: exchange energy $E_{exch.}$, anisotropy energy $E_{anis.}$, DMI energy E_{DMI}, demagnetizing

energy $E_{dem.}$, and Zeeman energy E_{zee}.

The equation can be rewritten as:

$$E_s = E_{exch} + E_{anis} + E_{DMI} + E_{zee} + E_{dem} \tag{6.8}$$

$$= \frac{E_0}{\frac{2r}{\pi\Delta} + 1} + 4\sqrt{A_{ex}K_{eff}} \cdot 2\pi rt - \pi D \cdot 2\pi rt + 2\mu_0 M_s H \cdot \pi r^2 t - \mu_0 {M_s}^2 I(d) 2\pi r t^2 \tag{6.9}$$

By following the analytical description of the phase diagram of bubbles and skyrmions by Bernand-Mantel et al. [198] and considering that the Dzyaloshinskii-Moriya Interaction (DMI) in the FGT double layers cancels (or almost cancels), the collapse of the bubbles in a bulk sample is predicted to occur when the Zeeman energy, which destabilizes the bubble, exceeds the long-range dipolar energy that stabilizes domains in the film. This is anticipated when the external magnetic field approaches the demagnetization field. Equation 6.9 predicts bubble collapse for bulk samples (with the radius r of the bubble much smaller than the sample thickness t) to occur at $H = \frac{2M_s}{\pi}$, corresponding to $B = 0.3$ T, which aligns well with the experimental observation. This independently confirms that the DMI in FGT is small compared to other interactions.

This collapse annihilates the topological charge of the bubble domain and is associated with an energetic barrier [197, 201, 202]. It's worth noting that all bubbles collapsed roughly at the same critical field, as reflected in the overall magnetization curve (not shown), which saturates at approximately 0.32 T along the easy magnetic direction.

6.4.3 Creep Behaviour in Skyrmion

"Creep" refers to a phenomenon caused by weak pinning. Pinning refers to the resistance experienced by a moving object when it encounters obstacles in its path. In the case of skyrmions, which are topologically protected magnetic textures in condensed matter systems, creep occurs when the skyrmions move through a medium that offers weak resistance to their motion due to the presence of defects or imperfections. These obstacles act as pinning sites that impede the motion of skyrmions.

However, if the pinning is weak, the skyrmions can still overcome these obstacles and move through the material, although at a slower pace. This effect cause as a gradual and intermittent motion of skyrmions in response to an applied driving force, such as an external magnetic field or an electrical current.

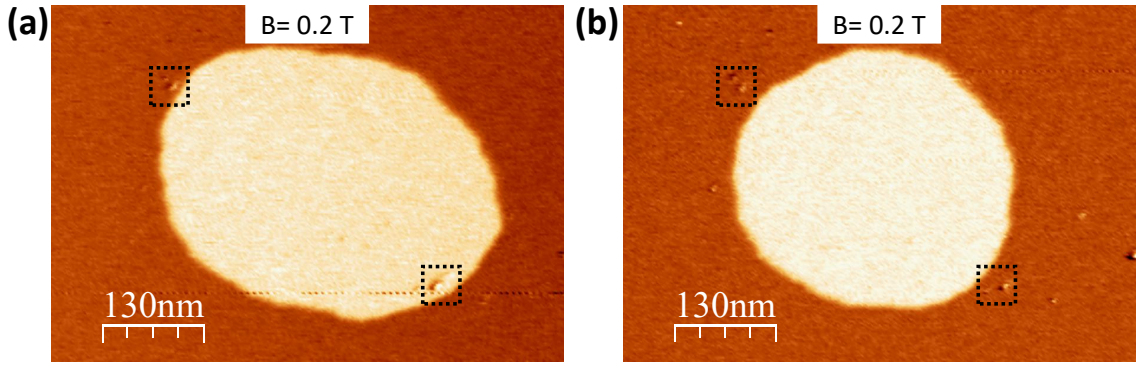

Figure 6.13: (a) Skyrmionic bubble depicted by dI/dU maps under the identical magnetic field of 0.2 T. (b) The corresponding map captured at the same magnetic field after a twelve-hour interval showing a reduction in skyrmion size over time. The square dashed boxes highlight consistent defects observed in the same region, serving as evidence of scans performed in the identical area after a twelve-hour duration. Measuring conditions: $U = -500$ mV, $I = 50$ pA, and $U_{mod}^{rms} = 80$ mV.

The Figure 6.13 displays the evolution of a skyrmionic bubble over a twelve-hour period, as depicted by dI/dU maps taken under an identical magnetic field strength of 0.2 T. Initially, the skyrmion exhibits a certain size and configuration in Figure 6.13(a), yet upon re-imaging the same region after twelve hours in Figure 6.13(b), a noticeable shrinkage in the skyrmion's size becomes apparent. This reduction in size is evident from the comparative analysis of the two maps, where the skyrmion appears to have contracted over time. Notably, the square dashed boxes highlight consistent defects observed within the same region, demonstrating that the scans were performed in identical areas during both imaging sessions. This shrinkage phenomenon is attributed to the creep effect, wherein weak pinning forces gradually lead to the skyrmion's contraction over time.

Understanding creep behavior in skyrmions is crucial for various technological applications, particularly in the field of spintronics and magnetic storage devices, where skyrmions are being considered for use as information carriers or memory elements. By studying creep phenomena, we can gain insights into the underlying mechanisms governing the motion of skyrmions and develop strategies to control and manipulate their movement for practical applications.

6.5 Summary

In summary, we explored a comprehensive examination of FGT through STM, unraveling its intricate topographical features such as steps, atomic resolution, and buckled structures influenced by various factors such as surface properties, sample preparation methods, experimental conditions, and instrument parameters. Furthermore, we employed SP-STM equipped through which we ex-

plored magnetic domains, skyrmions, and associated properties as a function of both magnetic and electric fields. The gradual reduction in the size of bubble domains with the application of a perpendicular magnetic field, counteracting the magnetization within the bubble until reaching a critical field of approximately 0.32 T, beyond which the bubble collapses. These discoveries establish a robust foundation for comprehending the complex magnetism intrinsic to FGT, particularly with regards to employing the material's topologically non-trivial magnetic states in hybrid structures.

Through a collaboration of SP-STM measurements and DFT calculations, we unveil the spin-polarized density of states, enabling a deeper insight into the material's electronic properties. Notably, SP-STM facilitates the attainment of sub-nanometer resolution, allowing for precise measurements of domain-wall width and exchange stiffness which closely matched with the theoretical calculations. Integrating experimental results with atomistic spin-dynamics simulations based on exchange parameters derived from DFT computations enhances our understanding of FGT's intricate properties at the nanoscale level. This holistic approach contributes to a comprehensive elucidation of FGT's behavior and characteristics, paving the way for further advancements in its application and manipulation at the nanoscale.

Chapter 7

Study of Fe_3GeTe_2: Magnon-Phonon Coupling

In this chapter, we delve into the investigation of the dip near the Fermi level observed in DOS spectra, as discussed in Chapter 6. Our primary objective is to uncover the underlying reason for this dip, with a particular focus on exploring the presence of inelastic excitations that may contribute to its incorporation. To this end, we embark on an investigation of the coupling between magnons and acoustic phonons in the 2D ferromagnetic van der Waals material FGT. Here, we utilised laterally resolved inelastic scanning tunneling spectroscopy (ISTS) measurements conducted with STM under ultrahigh vacuum conditions and low temperatures (40 mK). We performed DFT calculations with the aim of identifying the peaks observed in the inelastic spectra of FGT, discerning them as signatures indicative of hybrid magnon-phonon modes. These modes emerge at the crossing points between the magnonic and phononic bands, exhibiting qualitatively distinct behaviors in the low-energy region.

7.1 Introduction

In our investigation, we discern a distinct dip in the differential conductivity dI/dU proximate to the Fermi energy (E_F), as highlighted within the red dotted box of Figure 7.1(a), obtained via STS measurements. This dip is also observed in the spectra extracted from spin-polarized scanning tunneling spectroscopy (SP-STS) measurements for two opposite magnetic domains, as depicted in Figure 7.1(d) and their asymmetry in 7.1(e) which is reported in our work [203].

Several factors could potentially explain the appearance of the dip near E_F, including variations

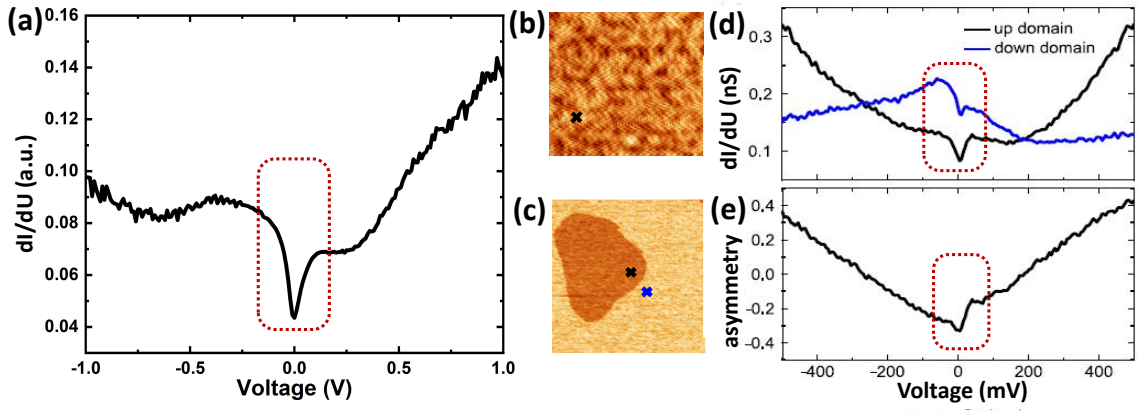

Figure 7.1: (a) dI/dU tunneling spectra acquired at a cross point highlighted within the scan area (20×20 nm^2) as depicted in (b), recorded at 1 V, 1 nA, and U_{mod}^{rms}=10 mV. (d) Tunneling spectra of spin-up (black) and spin-down (blue) domains taken on points as depicted in scan (c). (e) Asymmetry derived from (d). Measuring conditions: (d, e) $B = -0.29$ T, $U = -500$ mV, $I = 50$ pA, and $U_{mod}^{rms} = 10$ mV,

in the density of states (DOS), the presence of the Kondo resonance, or the occurrence of inelastic excitations. In the following section, we will explore each of these possibilities in detail.

7.1.1 Density of States

A potential reason for the dip observed in dI/dU may have been attributed to a corresponding dip in the electronic DOS. However, our collaborator Dr. Lichaun Zhang conducted DFT calculations for the DOS of FGT, as illustrated in Figure 7.2 and further detailed in [203], which contradicts this notion by revealing no dip near E_F. Hence, we are prompted to explore alternative explanations for this phenomenon.

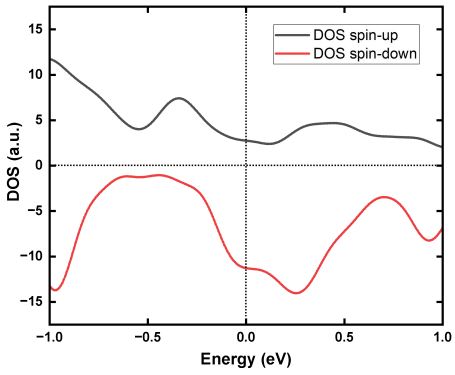

Figure 7.2: Calculated density of states (DOS) plot for FGT, where the black curve represents the spin-up state and the red curve corresponds to the spin-down state.

7.1.2 Kondo Resonance

Notably, similar dips have been documented in the literature [204, 205]. Zhang *et al.* interpret this dip as a Kondo resonance [204], while this interpretation is subject to debate with our reported data [203] and also in [205], primarily due to the ferromagnetic nature of the sample and the significant exchange splitting of the electronic bands [105]. The presence of a Kondo effect typically requires the system to adhere to time reversal symmetry, which is substantially broken in the ferromagnetic ground state. Additionally, the exchange interaction of localized spins is expected to split the Kondo resonance by an energy magnitude comparable to that of the exchange interaction, making the Kondo effect an unlikely source for the observed dip.

7.1.3 Inelastic Excitations

In 2D vdW magnets, the elementary bosonic excitations, including magnons and phonons, inherit the strong symmetry breaking characteristic of 2D materials, such as anisotropic dispersion [98–102] and chirality [103, 104]. The magnetic properties of 2D materials, particularly in magnetic 2D materials, are highly sensitive to strain engineering [105–110] due to the large uniaxial anisotropy and the local interactions of magnetic moments with the crystal field. This sensitivity potentially results in a remarkably high dynamic coupling between magnetic and lattice degrees of freedom in two dimensions, significantly impacting the dynamical properties of 2D magnets. Despite the significant potential, little is currently known about the nature and properties of elementary magnetic and lattice excitations in 2D magnetic materials, necessitating exploration using various techniques.

Among the various 2D magnets, FGT stands out due to its anticipated robust magnetoelastic coupling as predicted in prior research [105]. Previous studies have probed spin-optical phonon coupling in FGT utilizing Raman spectroscopy [206–208]. Hence, FGT emerges as an optimal platform for investigating excitations originating from both magnons and phonons. To validate these phenomena, we employed ISTS technique to quantitatively assess their presence and various associated properties.

7.2 Experimental Details and Discussions

ISTS has evolved into an established technique for locally resolving vibrons in adsorbed molecules [52] and has shown promise in resolving bulk phonons [58, 209], particularly in materials with strong electron-phonon coupling, such as superconductors. Moreover, ISTS has recently been

utilized for the detection of magnons [56, 210–213], further highlighting its potential in studying excitations in 2D magnetic materials.

We initiated the section with topography scans and obtained STS measurements on a flat surface. Subsequently, we delved into the analysis by taking the second derivative of the differential conductance, where we observed hints of inelastic excitations observed as peak-dip pairs in the low-energy regime. To ascertain whether these excitations originated from a magnetic source, we varied the magnetic field to observe the behavior of these ISTS measurements. Following this, we conducted spin-polarized measurements, providing clear evidence of the presence of magnon excitations within the system. Additionally, we presented theoretical calculations such as the DOS of magnons and phonons, along with their band crossings, to complement our experimental findings.

7.2.1 ISTS Measurements

We began our exploration with topographic scans. Our observations led us to a flat region elaborate with atomic step, prominently situated in the top left corner, as illustrated in Figure 7.3(a). Upon identifying a suitable flat area, we proceeded with the ISTS measurements. Figure 7.3(b) illustrates the differential conductivity within a narrow interval around E_F, measured at 40 mK with a small lock-in modulation voltage U_{mod}=0.5 mV, where $U(t) = U + U_{\text{mod}}\cos(ft)$ and f= 3.421 kHz. The choice of U_{mod} balances energy resolution and signal-to-noise ratio. Several steps at different energies are discernible. Meanwhile, in Figure 7.3(d), we delve into the analysis by taking the second derivative of the differential conductance, where we observed the hints of inelastic excitations showed as peak-dip pairs in the low energy regime. The d^2I/dU^2 spectra, obtained simultaneously with dI/dU spectra, exhibit five distinct peaks and dips symmetrically positioned relative to E_F, as depicted in Figure 7.3(d). Figure 7.3(c) illustrates that the inelastic features in the spectrum are not confined to a specific sample spot but are present throughout the sample, indicating that they are a property of the homogeneous sample. Hence, the data in Figure 7.3(b) and Figure 7.3(d) provide clear evidence of inelastic tunneling events.

Notably, at the low energy scale, peaks at 0.3, 0.8, 3.8, and 5.2 meV were observed, along with a double peak at 2.3 (indicated by red arrows), suggesting inelastic excitations arising from phonons or magnons, while plasmons, which have eV-scale energy, can be discarded. It is worth noting that the individual pairs of peaks and dips exhibit varying intensities. While vibron or phonon excitations typically display symmetric intensity, magnons show strong asymmetries due to spin selection rules [211].

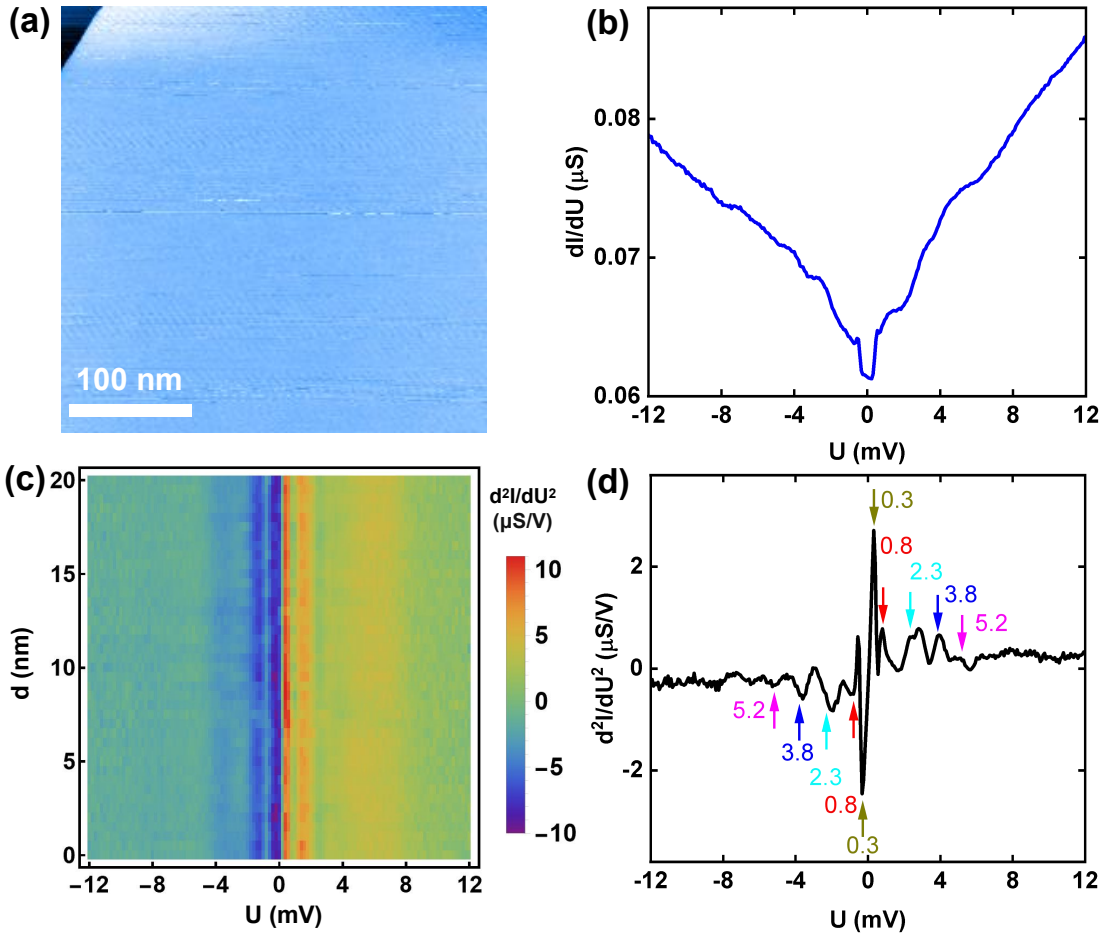

Figure 7.3: (a) Topography of the FGT surface displaying a step at the top left corner. (b) dI/dU spectrum averaged over 121 individual curves in a 4×4 nm^2 area. (d) Simultaneously recorded d^2I/dU^2 spectrum. (c) Averaged d^2I/dU^2 spectra taken along a 20 nm line on a flat surface.

7.2.2 Influence of Magnetic Fields on ISTS Measurements

To delve deeper into the insights provided by the ISTS measurements, we examined the impact of magnetic fields on the observed peak-dip pairs. Our experimental setup involved conducting measurements under a saturating external out-of-plane magnetic field, with variations in field strength ranging from 3 T to 5 T while measurement at 0 T taken as a reference, as illustrated in Figure 7.4.

Analyzing the data obtained from these experiments revealed a notable shift in the positions of the peaks due to the magnetic field strength, suggesting the involvement of magnetic phenomena. In order to gain a better understanding of these magnetic origins, we proceeded to conduct spin-polarized ISTS measurements, the findings of which are elaborated upon in the subsequent section.

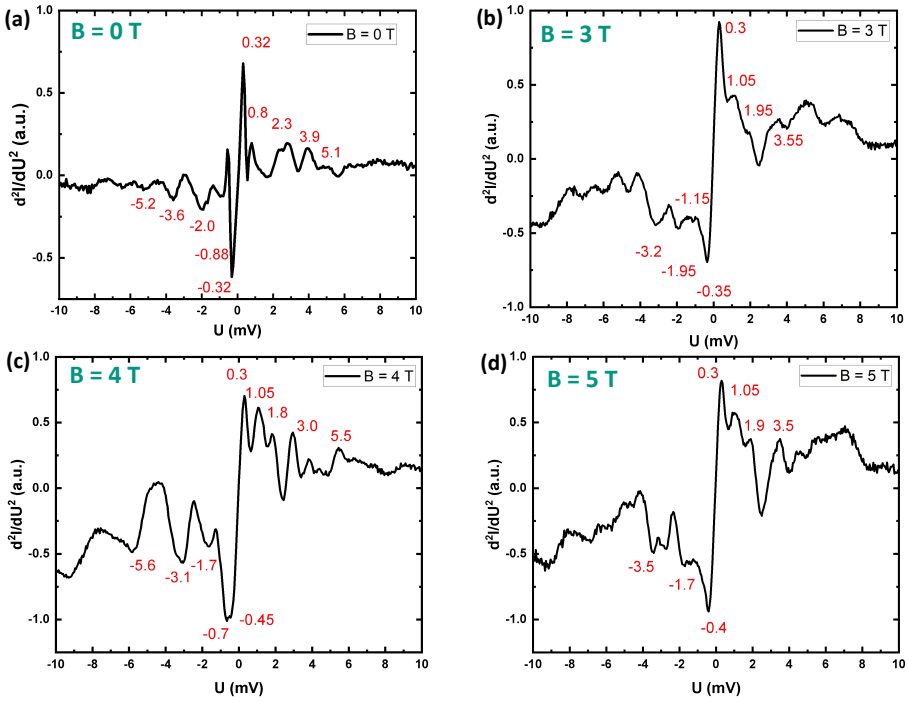

Figure 7.4: ISTS at vaious range of external out-of-plane magnetic fields (a) 0 T, (b) 3 T, (c) 4 T, (d) 5 T.

7.2.3 Spin polarized-ISTS Measurements

To further validate the magnetic origin of these excitations, we employed ISTS using spin-polarized STM. To polarize the tip, approximately 50 monolayers (ML) of chromium (Cr) were deposited onto freshly prepared tungsten (W) tips, followed by gentle annealing [214]. The use of antiferromagnetic tips minimizes the magnetic stray field, thereby exerting a negligible influence on the magnetization of the FGT sample [203]. This setup enables the comparison of inelastic tunneling spectra for parallel and antiparallel orientations of the magnetization of the electrodes, which serves as the standard test for magnetic excitations [210, 215].

In the following analysis, Figure 7.5 depicts the magnetic domains scanned using an SP-tip. Subsequently, SP-ISTS measurements were conducted, capturing d^2I/dU^2 spectra across the magnetic domain wall, as illustrated in Figure 7.6(a).

We depict the position-dependent inelastic tunneling signal for a structure corresponding to that in Figure 7.3(c). Notably, the spectra exhibit no expected variation for a homogeneous sample, alongside a spin-integrating measurement. Conversely, as shown in Figure 7.6(a), recorded with a spin-polarized tip, there is a discernible sudden lateral change in the inelastic signal, coinciding with a 180° magnetic domain wall in SP-STM scans. Figure 7.6(b) illustrates a lateral map of this

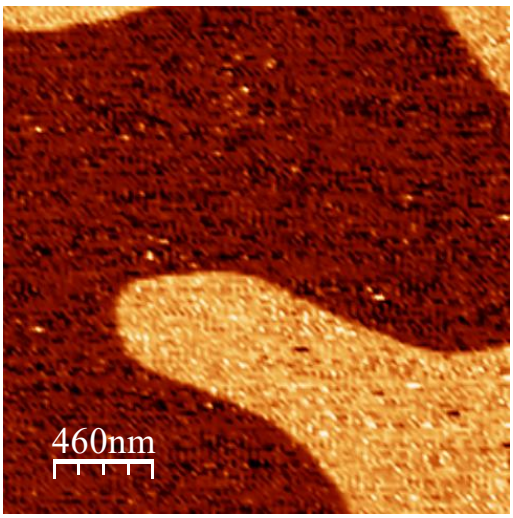

Figure 7.5: Spin polarized dI/dU mapping at 500 mV with Cr-coated W tip.

transition at a bias voltage of 5 mV. Moreover, the measured width of 7 nm aligns with previous assessments of the 180° magnetic domain wall width [203]. Consequently, to the left and right of the domain wall, there is an alteration in the relative orientation between the tip and sample magnetization by 180°, accompanied by an exchange in the relative roles of minority and majority carriers in the sample. Remarkably, at the energies corresponding to the peaks and dips observed in the inelastic spectra, we note an intensity variation at the domain wall owing to spin-polarized tunneling, consistent with the spin selection rules [211]. Specifically, stronger peaks at positive bias on the right side (indicated by redder colors) align with weaker dips at the same but negative bias (depicted in greener color) on the right side. Conversely, both features undergo a change at the domain wall, transitioning to weaker peaks at positive bias (illustrated in green color) and stronger dips at corresponding negative bias (shown in blue color) towards the left side.

The asymmetry in intensity of magnon excitation peaks is related to the spin polarization of the magnetic sample, particularly when using an unpolarized tip. The calculated asymmetry, derived from the data in Figure 7.6(c), approximately -0.1, is comparable to a DFT value for spin-polarization of the bulk states around E_F of approximately -0.36 [203], suggesting a magnetic origin of excitations in FGT. Furthermore, it is observed that using a larger modulation voltage reveals broader peak-dip pairs at energies around 6 meV and beyond. However, this study primarily focuses on the sharp inelastic peaks and dips at low energies. This identification of the peaks as magnetic excitations or magnons, however, does not offer an understanding of their energetics. It's worth noting that the parabolic dispersion of magnons around the zone center typically does not generate a peaked DOS, and magnons usually manifest in a relatively smooth ISTS signal around the Fermi energy.

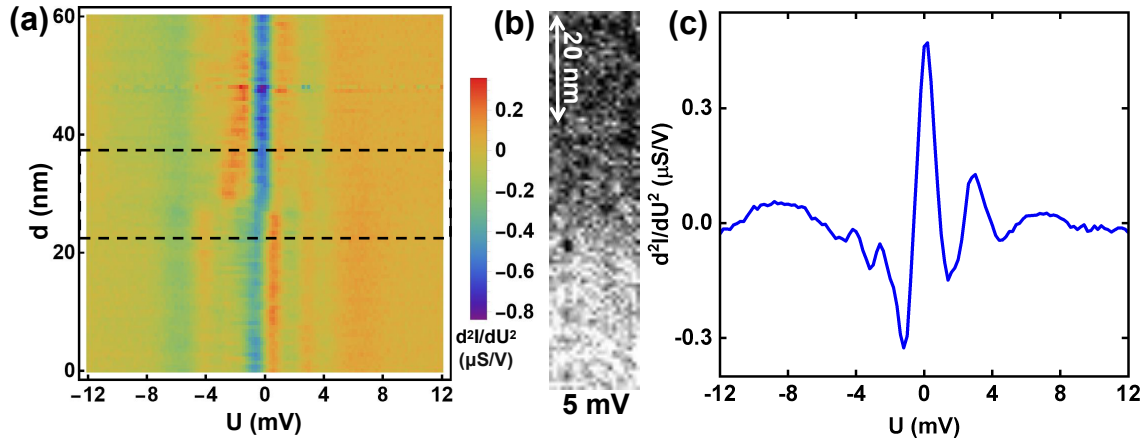

Figure 7.6: (a) Spectra of Spin-Polarized Inelastic Electron Tunneling Spectroscopy (SP-ITS) captured across a magnetic domain wall (U = 20 mV, I = 0.3 nA, and modulation of 1 mV). (b) Mapping of the second derivative of tunneling current with respect to voltage (d^2I/dU^2) at 5 mV under tunneling conditions of U = 5 mV, I = 0.2 nA, and Umod = 2 mV. (c) Variation in d^2I/dU^2 between different domains.

7.3 Theoretical Calculations

To account for the influence of phonons, a comprehensive analysis were conducted by calculating their DOS and dispersion within FGT using ab-initio methods. The computations were carried out by our collaborator team lead by Prof. Dr. Yuriy Mokrousov and Dr. Lichaun Zhang using the Vienna Ab Initio Simulation Package (VASP) under the framework of the Local Density Approximation (LDA) for the exchange correlation potential. The interactions between electrons and nuclei were described using the projector-augmented wave (PAW) method. A kinetic energy cutoff of 600 eV was selected for the plane wave expansion, ensuring accurate representation of the electronic states. Energy convergence was achieved with a threshold of 10^{-9} eV. For Brillouin zone sampling, a $15 \times 15 \times 5$ γ-centered Monkhorst-Pack grid was employed. Structural optimization was performed for each cell, ensuring stability, with maximum force on each atom maintained below 0.001eV/Å. Furthermore, phonon dispersion calculations were conducted using PHONOPY within a $3 \times 3 \times 2$ supercell framework employing the finite displacement method.

7.3.1 DOS of Phonon and Magnon

Phonons serve as pivotal constituents shaping the energy landscape of materials, potentially revealing distinct features like sharp van Hove singularities within the meV range. The phonon DOS is determined through DFT calculations, which offer a comprehensive understanding of the vibra-

tional properties of the material. These calculations enable us to explore the distribution of phonon energies within the system, providing insights into its lattice dynamics and thermal behavior.

The phonon DOS, as illustrated by the blue curve in Figure 7.7, exhibits pronounced peaks between 10 and 15 meV, consistent with observations from inelastic neutron scattering experiments [102, 216]. Intriguingly, the absence of these phonon peaks in the ISTS data depicted in Figure 7.3 hints at a relatively weak electron-phonon coupling within the material.

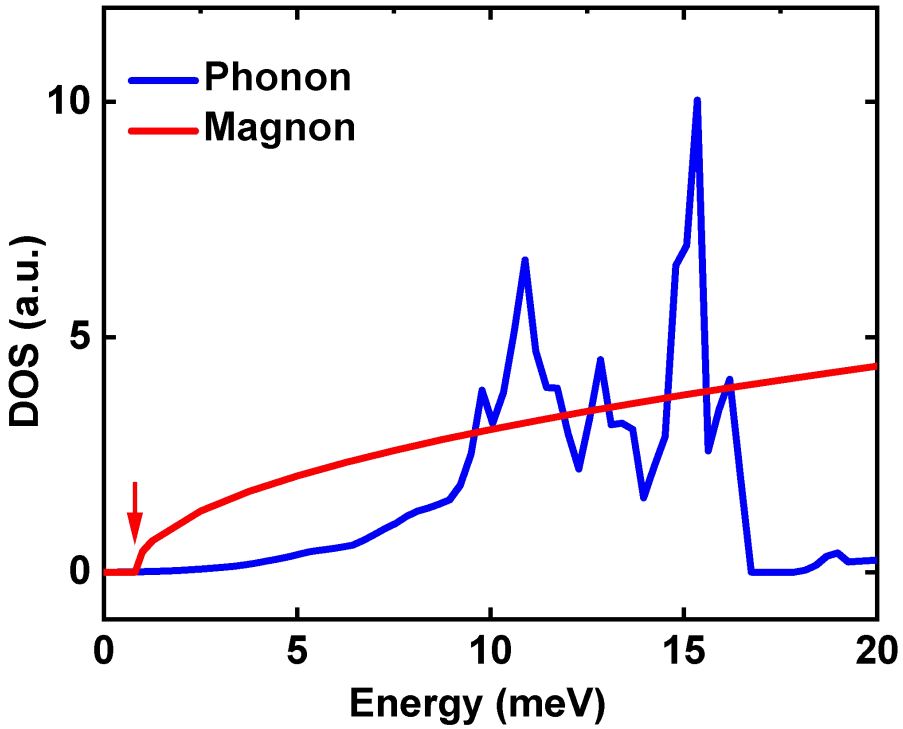

Figure 7.7: Calculated density of states of phonon (blue) and magnon (red). The spin-wave stiffness is taken as 53.6 meVÅ^2 from Ref. [98]. A magnon gap of 0.81 meV is used and is indicated by the red arrow.

Furthermore, below the 5 meV threshold, the phonon DOS exhibits a smooth distribution, indicative of the linear dispersion of the lowest energy bands associated with transversal and longitudinal acoustic phonons within this energy range.

On the other hand, the magnon DOS is derived from three-dimensional dispersions, characterized by their anisotropic and parabolic nature, particularly around the Brillouin zone center. This approach allows us to capture the intricate behavior of magnons within the material, accounting for their momentum-dependent properties and interactions. By analyzing the magnon DOS, we gain crucial information about the magnetic excitations present in the system and their contribution to its overall magnetic behavior.

The spin-wave stiffness, a crucial parameter in describing the collective behavior of magnetic excitations, is sourced from a reliable reference [98], where it is reported as 53.6 meVÅ^2. This value characterizes the energy required to propagate spin waves through the material, providing essential insights into its magnetic properties and dynamics.

Additionally, in our calculations, we incorporate a magnon gap of 0.81 meV, as identified in the literature [98]. This magnon gap, depicted by the red arrow in Figure 7.7, signifies the minimum energy required to excite magnons in the system with a uniaxial magnetic anisotropy. By considering this gap, we can accurately model the energy spectrum of magnons and their contributions to the material's magnetic behavior.

Furthermore, exploring the dispersion bands of phonons and magnons, along with their interplay, significantly influences the behavior of both types of excitations. This interaction results in hybridized modes exhibiting unique characteristics. Through the investigation of these hybrid modes, we can delve deeper into understanding the dynamic behavior of the material, as we elaborate on in the following section.

7.3.2 Phonon and Magnons Band Crossings

Introducing magnon-phonon coupling into the analysis transformed the system's behavior significantly. Specifically, when phonon and magnon bands intersected, the interplay between magnetoelastic coupling (denoted as B×ϵ, where B represented the magnetoelastic coupling and ϵ symbolized the strain tensor [60]) hybridized these distinct modes, leading to an avoided level crossing phenomenon. These regions, commonly referred to as "hot spots" within the Brillouin zone, were characterized by strong interactions between the magnetization and lattice dynamics. Notably, this coupling mechanism contributed significantly to certain aspects of Gilbert damping [217], highlighting its profound influence on the material's overall magnetic behavior.

In essence, the emergence of avoided level crossings at the intersections of phonon and magnon bands signified a pivotal point where the magnetic and lattice degrees of freedom intricately intertwined. These hot spots represented points of heightened interaction between the magnetic and lattice subsystems, exerting a pronounced influence on the material's magnetic properties. Moreover, the magnetoelastic coupling mechanism not only impacted the dynamics of the magnetization but also played a crucial role in shaping the material's response to external stimuli. Therefore, understanding the implications of magnon-phonon coupling and its realization in avoided level crossings was essential for unraveling the intricate behavior of quantum materials under diverse experimental conditions.

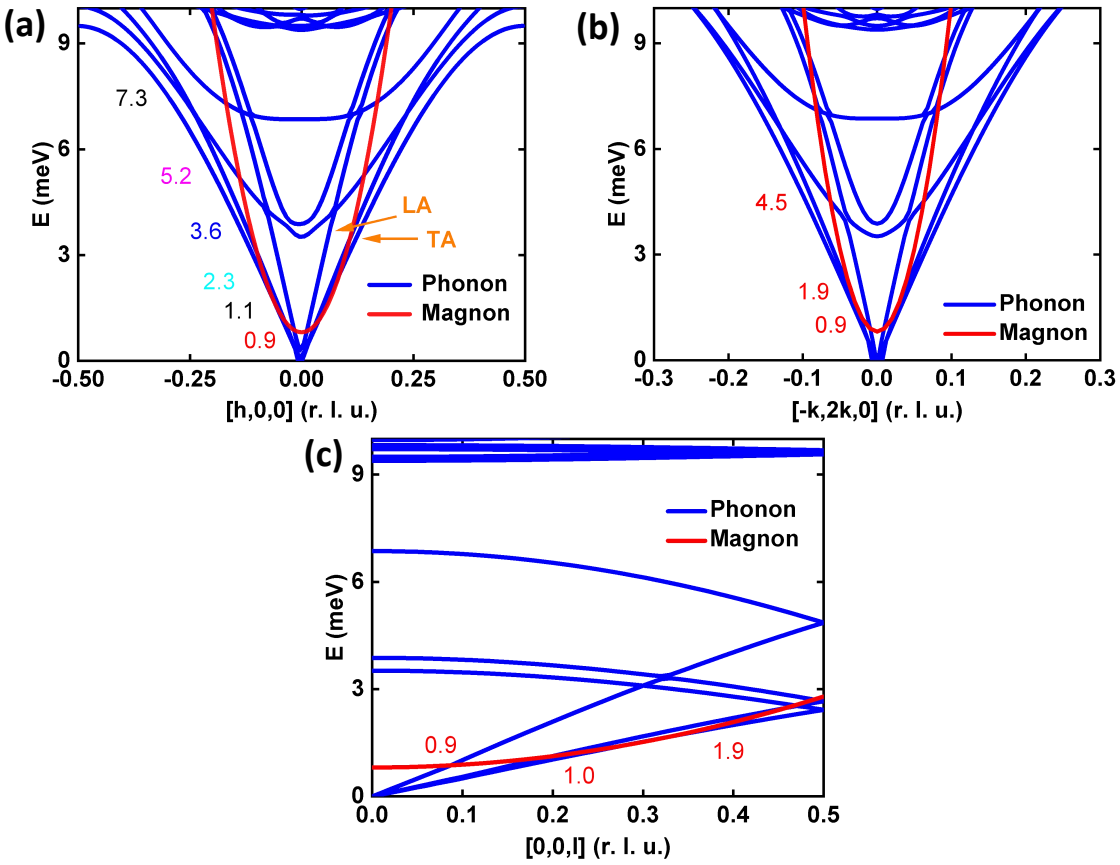

Figure 7.8: (a) Band crossings between magnon and phonon bands along [100]. The spin-wave stiffness is taken at 69.0 meVÅ^2 from Ref. [98]. (b) Crossings between magnon and phonon bands along [$\bar{1}$20]. The spin-wave stiffness is taken as 56.7 meVÅ^2 from Ref. [98]. (c) Crossings between magnon and phonon bands along [001]. The spin-wave stiffness is taken as 53.6 meVÅ^2 from Ref. [98]. In all calculations, a magnon gap of 0.81 meV is used.

In FGT, our analysis revealed the presence of avoided level crossings, characterized by diabolic points, which resulted in a notable increase in the DOS due to hybrid excitations. Figure 7.8(a) illustrates the phonon dispersion of FGT obtained from ab-initio calculations, juxtaposed with experimental magnon dispersion curves obtained from neutron scattering experiments [98]. Through neutron scattering measurements, we determined the spin-wave stiffness to be approximately 69.0 meVÅ^2 along the [100]-direction. Additionally, employing Kittel's formula, which incorporates uniaxial anisotropy (K_u) and saturation magnetization (M_s), we calculated a spin-wave gap of 0.81 meV for FGT [154]. Importantly, this calculation required no fitting parameters, enhancing the reliability of our predictions.

The plotted data revealed band crossings between the linearly dispersive acoustic phonons and the parabolic magnon spectrum, occurring near the Γ-point at an energy of 0.9 meV across all directions (see Figure 7.8(b)). These intersections were consistent with the observed peak and

dip patterns in the inelastic spectrum. Furthermore, as the magnon dispersion exhibited quadratic behavior, additional crossings were anticipated to emerge along various directions. Notably, the anisotropic nature of the magnon dispersion meant that weak exchange along the [001]-direction, perpendicular to the van der Waals layers, precluded second crossings with all but the lowest phonon band (see Figure 7.8(c)). Conversely, along the high-symmetry [100]-direction, we expected second crossings at energies of 2.3, 3.6, and 5.2 meV, aligning closely with theoretical predictions. Along the lower symmetry [$\bar{1}$20]-direction, lower spectral weight was anticipated for the crossings, resulting in less pronounced peaks. Consequently, the corresponding features were not clearly resolved in the spectra, suggesting either weak hybridization or no hybridization at all along these directions.

7.4 Comparative Analysis of Experimental Data and Theoretical Calculations

The theoretically expected crossing points as shown in Figure 7.9(a) aligned remarkably well with the positions of the experimental inelastic peaks and dips, as depicted in Figure 7.9(b).

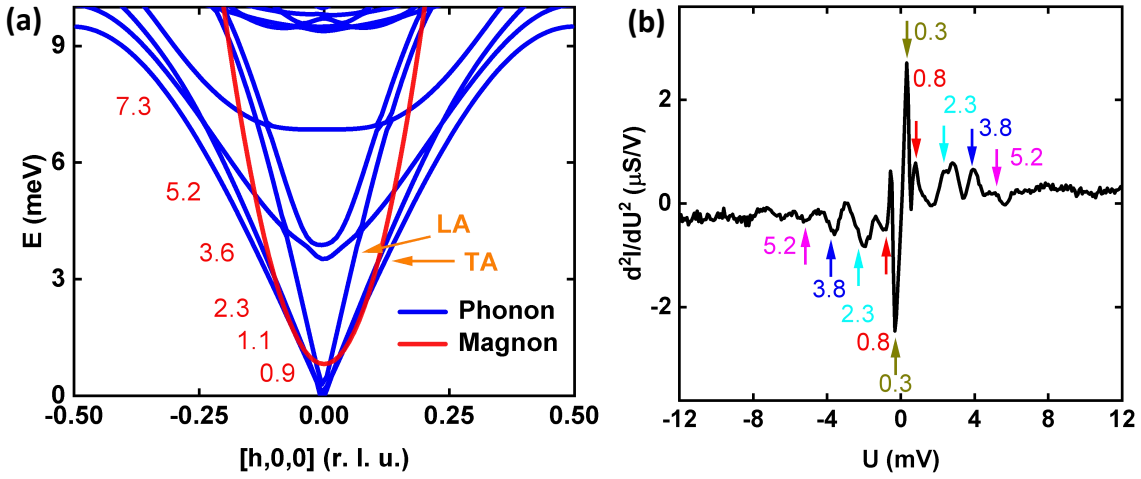

Figure 7.9: Comparison between (a) Phonon and magnon dispersion band crossing points (in blue and red respectively), and (b) Energy points corresponding to peak-dip pairs observed in experimental ISTS measurements.

This alignment provided clear evidence for the presence of robust magnon-phonon coupling within one of the most significant 2D materials. It's worth noting that the lowest energy peak and dip pair observed at 0.3 meV was unlikely to be attributed to magnon-phonon coupling. Instead, this phenomenon, observed at very low temperatures across various samples, was interpreted as a dynamical Coulomb blockade effect [58, 218–220]. This effect stems from the prolonged lifetimes

of quasiparticles within Fermi liquids near the Fermi energy and at low temperatures, hindering a second low-energy electron from tunneling into the same state until the first one is scattered. This peculiar behavior has been observed in noble metals at low temperatures as well [220], manifesting as a dip at zero bias in dI/dU with a width of roughly twice U_{mod}^{rms} or as a peak-dip feature in d^2I/dU^2 at approximately $\pm U_{mod}^{rms}$.

Interestingly, optical phonons also intersected the magnon dispersion at higher energies, where neutron scattering data indicated a significant damping of the magnon dispersion [98, 101, 102]. However, magnon-phonon coupling involving optical phonons has been identified using Raman spectroscopy [206, 208].

7.5 Summary

In summary, our investigation has unveiled the distinctive peak-dip pairs observed in the inelastic spectra of FGT, representing hybrid magnon-phonon modes. These intriguing modes displayed at the crossing of magnonic and phononic bands, exhibiting unique behaviors at low energies. Our exploration underscores the significance of FGT and other 2D magnetic materials as intriguing platforms for delving into the complexities of low-energy magnon-phonon hybrid modes. These findings not only shed light on potential hybrid magnon-phonon topologies but also offer promising insights for informed material design, particularly in fostering dynamic magnon-phonon coupling within the two-dimensional realm.

Furthermore, our ISTS investigations have yielded compelling evidence of strong magnon-phonon coupling, especially near the Zone center where acoustic phonon dispersion intersects with magnon dispersion. Spin-polarized measurements have validated the magnetic nature of these hybrid excitations, affirming the intricate interplay between magnetism and lattice vibrations. Notably, our ISTS technique has enabled the precise resolution of domain walls within the inelastic signal, providing valuable insights into the spatial distribution of magnetic features. With ISTS's capability to probe confined modes within structured samples, there lies vast potential for exploring phenomena like magnon localization in bulk or single-layer FGT, potentially facilitating the design of magnon waveguides. Additionally, magnetic domain walls may serve as platforms for phonon localization, enabling precise control over lattice dynamics. Moreover, the emergence of hybrid bosonic excitations hints at the prospect of imparting chirality to phonons, paving the way for manipulating angular momentum transport within the lattice. These findings not only enrich our understanding of magnon-phonon interactions but also hold promise for advancing spintronic and phononic devices in the future.

Chapter 8

Summary and Outlook

In the framework of this thesis, our primary objective was to delve into the magnetism of 2D transition metal dichalcogenide (TMD) materials. We initiated our investigation with the well-known 2D TMD VSe_2, aiming to explore its magnetic properties. We grew high quality of ML of VSe_2 on HOPG using MBE technique. However, our experiments revealed that the presence of charge density wave (CDW) phenomena suppressed the magnetism within these systems.

After that, we redirected our focus to another prominent 2D material: ferromagnetic van der Waals material FGT (Fe_3GeTe_2). Here, we conducted an in-depth examination of its topographical features, including steps, atomic resolution, and buckled structures. These features were influenced by various factors such as surface properties, sample preparation methods, experimental conditions, and instrument parameters. Employing SP-STM, we explored magnetic domains, skyrmions, and related properties under different magnetic and electric fields.

Our investigations into FGT unveiled intriguing phenomena, such as the gradual reduction in the size of magnetic bubble domains with the application of a perpendicular magnetic field until a critical field is reached, causing the collapse of the bubble. Collaborative efforts involving SP-STM measurements and DFT calculations enabled us to uncover the spin-polarized density of states, providing deeper insights into FGT's electronic properties. This comprehensive approach, integrating experimental results with atomistic spin-dynamics simulations, significantly enhanced our understanding of FGT's intricate properties at the nanoscale level, laying the groundwork for further advancements in its manipulation and application.

Subsequently, we turned our attention to investigating a dip observed near the Fermi level in the STS measurements. Through ISTS measurements, we explored the underlying causes of this

dip, revealing distinctive peak-dip pairs representing hybrid magnon-phonon modes. Our findings underscored the significance of FGT and other 2D magnetic materials as platforms for exploring low-energy magnon-phonon hybrid modes. Additionally, our ISTS investigations provided compelling evidence of strong magnon-phonon coupling, especially near the zone center where acoustic phonon dispersion intersects with magnon dispersion.

The precise resolution of domain walls within the inelastic signal offered valuable insights into the spatial distribution of magnetic features, paving the way for exploring phenomena such as magnon localization and phonon manipulation in FGT. Furthermore, the emergence of hybrid bosonic excitations hinted at the prospect of manipulating angular momentum transport within the lattice, offering promising avenues for advancing spintronic and phononic devices in the future.

List of Figures

List of Tables

Bibliography

[1] K.S. Novoselov, A.K. Geim, S.V. Morozov, D.e. Jiang, Y. Zhang, S.V. Dubonos, I.V. Grigorieva, A.A. Firsov, Science **306**, 666 (2004).

[2] A.C. Neto, F. Guinea, N.M. Peres, K.S. Novoselov, A.K. Geim, Rev. Mod. Phys. **81**, 109 (2009).

[3] S.Z. Butler, S.M. Hollen, L. Cao, Y. Cui, J.A. Gupta, H.R. Gutiérrez, T.F. Heinz, S.S. Hong, J. Huang, A.F. Ismach, et al., ACS nano **7**, 2898 (2013).

[4] K.S. Novoselov, D. Jiang, F. Schedin, T. Booth, V. Khotkevich, S. Morozov, A.K. Geim, Proc. Natl. Acad. Sci. **102**, 10451 (2005).

[5] A. Splendiani, L. Sun, Y. Zhang, T. Li, J. Kim, C.Y. Chim, G. Galli, F. Wang, Nano Lett. **10**, 1271 (2010).

[6] K.F. Mak, C. Lee, J. Hone, J. Shan, T.F. Heinz, Phys. Rev. Lett. **105**, 136805 (2010).

[7] A.K. Geim, Science **324**, 1530 (2009).

[8] A.K. Geim, Rev. Mod. Phys. **83**, 851 (2011).

[9] K. Novoselov, Rev. Mod. Phys. **83**, 837 (2011).

[10] K. Novoselov, A. Mishchenko, A. Carvalho, A. Castro Neto, Science **353**, aac9439 (2016).

[11] L. Li, E. O'Farrell, K. Loh, G. Eda, B. Özyilmaz, A. Castro Neto, Nature **529**, 185 (2016).

[12] Y. Cao, V. Fatemi, S. Fang, K. Watanabe, T. Taniguchi, E. Kaxiras, P. Jarillo-Herrero, Nature **556**, 43 (2018).

[13] Z.Y. Rong, P. Kuiper, Phys. Rev. B **48**, 17427 (1993).

[14] R. Bistritzer, A.H. MacDonald, Proc. Natl. Acad. Sci. **108**, 12233 (2011).

[15] C. Woods, L. Britnell, A. Eckmann, R. Ma, J. Lu, H. Guo, X. Lin, G. Yu, Y. Cao, R.V. Gorbachev, et al., Nat. Phys. **10**, 451 (2014).

[16] W. Han, R.K. Kawakami, M. Gmitra, J. Fabian, Nat. Nanotechnol. **9**, 794 (2014).

[17] M. Gmitra, J. Fabian, Phys. Rev. B **92**, 155403 (2015).

[18] S. Manzeli, D. Ovchinnikov, D. Pasquier, O.V. Yazyev, A. Kis, Nat. Rev. Mater. **2**, 1 (2017).

[19] J.G. Park, J. Condens. Matter Phys. **28**, 301001 (2016).

[20] K.S. Burch, D. Mandrus, J.G. Park, Nature **563**, 47 (2018).

[21] C. Gong, X. Zhang, Science **363**, eaav4450 (2019).

[22] M. Gibertini, M. Koperski, A.F. Morpurgo, K.S. Novoselov, Nat. Nanotechnol. **14**, 408 (2019).

[23] S. Wolf, D. Awschalom, R. Buhrman, J. Daughton, v.S. von Molnár, M. Roukes, A.Y. Chtchelkanova, D. Treger, Science **294**, 1488 (2001).

[24] A. Kirilyuk, A.V. Kimel, T. Rasing, Rev. Mod. Phys. **82**, 2731 (2010).

[25] T. Jungwirth, X. Marti, P. Wadley, J. Wunderlich, Nat. Nanotechnol. **11**, 231 (2016).

[26] V. Baltz, A. Manchon, M. Tsoi, T. Moriyama, T. Ono, Y. Tserkovnyak, Rev. Mod. Phys. **90**, 015005 (2018).

[27] P. Němec, M. Fiebig, T. Kampfrath, A.V. Kimel, Nat. Phys. **14**, 229 (2018).

[28] B. Radisavljevic, A. Radenovic, J. Brivio, V. Giacometti, A. Kis, Nat. Nanotechnol. **6**, 147 (2011).

[29] M. Acerce, D. Voiry, M. Chhowalla, Nat. Nanotechnol. **10** (2015).

[30] Y.P. Feng, L. Shen, M. Yang, A. Wang, M. Zeng, Q. Wu, S. Chintalapati, C.R. Chang, Wiley Interdiscip. Rev. Comput. Mol. Sci. **7**, e1313 (2017).

[31] R. Wiesendanger, Rev. Mod. Phys. **81**, 1495 (2009).

[32] G. Binnig, H. Rohrer, C. Gerber, E. Weibel, Phys. Rev. Lett. **49**, 57 (1982).

[33] R. Wiesendanger, H.J. Güntherodt, G. Güntherodt, R.J. Gambino, R. Ruf, Phys. Rev. Lett. **65**, 247 (1990).

[34] W. Wulfhekel, J. Kirschner, Annu. Rev. Mater. Sci. **37**, 69 (2007).

[35] T. Balashov, Ph.D. thesis (2009).

[36] G. Binnig, H. Rohrer, Rev. Mod. Phys. **59**, 615 (1987).

[37] C.J. Chen, vol. 69 (Oxford University Press, USA, 2021).

[38] G. Binnig, H. Rohrer, C. Gerber, E. Weibel, Phys. Rev. Lett. **49**, 57 (1982).

[39] B. Voigtländer, (Springer, 2015).

[40] J. Bardeen, Phys. Rev. Lett. **6**, 57 (1961).

[41] J. Tersoff, D.R. Hamann, Phys. Rev. B **31**, 805 (1985).

[42] P.K. Hansma, J. Tersoff, Journal of Applied Physics **61**, R1 (1987).

[43] G. Binnig, D.P. Smith, Rev. Sci. Instrum. **57**, 1688 (1986).

[44] F. Hooge, T. Kleinpenning, L.K. Vandamme, Rep. Prog. Phys. **44**, 479 (1981).

[45] J. Tersoff, D.R. Hamann, Phys. Rev. B **31**, 805 (1985).

[46] M. Bode, Rep. Prog. Phys. **66**, 523 (2003).

[47] R.C. Jaklevic, J. Lambe, Phys. Rev. Lett. **17**, 1139 (1966).

[48] E.L. Wolf, vol. 152 (OUP Oxford, 2011).

[49] W. Olejniczak, Z. Klusek, M. Bieniecki, Applied Physics A: Materials Science & Processing **66** (1998).

[50] L. Vitali, M. Schneider, K. Kern, L. Wirtz, A. Rubio, Phys. Rev. B **69**, 121414 (2004).

[51] T. Balashov, A.F. Takács, W. Wulfhekel, J. Kirschner, Phys. Rev. Lett. **97**, 187201 (2006).

[52] B.C. Stipe, M.A. Rezaei, W. Ho, Science **280**, 1732 (1998).

[53] A.J. Heinrich, J.A. Gupta, C.P. Lutz, D.M. Eigler, Science **306**, 466 (2004).

[54] T. Balashov, T. Schuh, A. Takács, A. Ernst, S. Ostanin, J. Henk, I. Mertig, P. Bruno, T. Miyamachi, S. Suga, et al., Phys. Rev. Lett. **102**, 257203 (2009).

[55] T. Schuh, T. Miyamachi, S. Gerstl, M. Geilhufe, M. Hoffmann, S. Ostanin, W. Hergert, A. Ernst, W. Wulfhekel, Nano Lett. **12**, 4805 (2012).

[56] C.L. Gao, A. Ernst, G. Fischer, W. Hergert, P. Bruno, W. Wulfhekel, J. Kirschner, Phys. Rev. Lett. **101**, 167201 (2008).

[57] T. Balashov, A.F. Takács, M. Däne, A. Ernst, P. Bruno, W. Wulfhekel, Phys. Rev. B **78**, 174404 (2008).

[58] M. Schackert, T. Märkl, J. Jandke, M. Hölzer, S. Ostanin, E.K. Gross, A. Ernst, W. Wulfhekel, Phys. Rev. Lett. **114**, 047002 (2015).

[59] P.K. Hansma, Phys. Rep. **30**, 145 (1977).

[60] C. Kittel, Phys. Rev. **110**, 836 (1958).

[61] A. Jayakumar, A. Surendranath, P. Mohanan, Int. J. Pharm. **551**, 309 (2018).

[62] Y. Ma, Y. Dai, M. Guo, C. Niu, Y. Zhu, B. Huang, ACS Nano **6**, 1695 (2012).

[63] S. Lebègue, T. Björkman, M. Klintenberg, R.M. Nieminen, O. Eriksson, Phys. Rev. X **3**, 031002 (2013).

[64] W.Y. Tong, S.J. Gong, X. Wan, C.G. Duan, Nat. Commun. **7**, 13612 (2016).

[65] R.G. Dickinson, L. Pauling, J. ACS **45**, 1466 (1923).

[66] J.A. Wilson, A. Yoffe, Adv. Phys. **18**, 193 (1969).

[67] R. Frindt, A. Yoffe, Proceedings of the Royal Society of London. Series A. Mathematical and Physical Sciences **273**, 69 (1963).

[68] P. Joensen, R. Frindt, S.R. Morrison, Materials research bulletin **21**, 457 (1986).

[69] P.A. Lee, N. Nagaosa, X.G. Wen, Rev. Mod. Phys. **78**, 17 (2006).

[70] A. Kitaev, Annals of Physics **321**, 2 (2006).

[71] L. Onsager, Physical Review **65**, 117 (1944).

[72] V. Berezinskii, Sov. Phys. JETP **32**, 493 (1971).

[73] J.M. Kosterlitz, D.J. Thouless, (CRC Press, 2018), pp. 493–515.

[74] N.D. Mermin, H. Wagner, Phys. Rev. Lett. **17**, 1133 (1966).

[75] F. Hellman, A. Hoffmann, Y. Tserkovnyak, G.S. Beach, E.E. Fullerton, C. Leighton, A.H. MacDonald, D.C. Ralph, D.A. Arena, H.A. Dürr, et al., Rev. Mod. Phys. **89**, 025006 (2017).

[76] J.G. Park, arXiv preprint arXiv:1604.08833 (2016).

[77] R. Roldán, A. Castellanos-Gomez, E. Cappelluti, F. Guinea, J. Condens. Matter Phys. **27**, 313201 (2015).

[78] D. Zhong, K.L. Seyler, X. Linpeng, R. Cheng, N. Sivadas, B. Huang, E. Schmidgall, T. Taniguchi, K. Watanabe, M.A. McGuire, et al., Sci. Adv. **3**, e1603113 (2017).

[79] B. Huang, G. Clark, E. Navarro-Moratalla, D.R. Klein, R. Cheng, K.L. Seyler, D. Zhong, E. Schmidgall, M.A. McGuire, D.H. Cobden, et al., Nature **546**, 270 (2017).

[80] C. Gong, L. Li, Z. Li, H. Ji, A. Stern, Y. Xia, T. Cao, W. Bao, C. Wang, Y. Wang, et al., Nature **546**, 265 (2017).

[81] J. Xu, W.A. Phelan, C.L. Chien, Nano Lett. **19**, 8250 (2019).

[82] M. Kim, P. Kumaravadivel, J. Birkbeck, W. Kuang, S.G. Xu, D. Hopkinson, J. Knolle, P.A. McClarty, A. Berdyugin, M. Ben Shalom, et al., Nat. Electron. **2**, 457 (2019).

[83] Y. Deng, Y. Yu, M.Z. Shi, Z. Guo, Z. Xu, J. Wang, X.H. Chen, Y. Zhang, Science **367**, 895 (2020).

[84] Z. Wang, T. Zhang, M. Ding, B. Dong, Y. Li, M. Chen, X. Li, J. Huang, H. Wang, X. Zhao, et al., Nat. Nanotechnol. **13**, 554 (2018).

[85] S. Jiang, J. Shan, K.F. Mak, Nat. Mater. **17**, 406 (2018).

[86] T. Song, X. Cai, M.W.Y. Tu, X. Zhang, B. Huang, N.P. Wilson, K.L. Seyler, L. Zhu, T. Taniguchi, K. Watanabe, et al., Science **360**, 1214 (2018).

[87] W. Xing, Y. Chen, P.M. Odenthal, X. Zhang, W. Yuan, T. Su, Q. Song, T. Wang, J. Zhong, S. Jia, et al., 2D Materials **4**, 024009 (2017).

[88] R. Zhu, W. Zhang, W. Shen, P.K.J. Wong, Q. Wang, Q. Liang, Z. Tian, Y. Zhai, C.w. Qiu, A.T. Wee, Nano Lett. **20**, 5030 (2020).

[89] B. Huang, G. Clark, E. Navarro-Moratalla, D.R. Klein, R. Cheng, K.L. Seyler, D. Zhong, E. Schmidgall, M.A. McGuire, D.H. Cobden, W. Yao, D. Xiao, P. Jarillo-Herrero, X. Xu, Nature **546**, 270 (2017).

[90] C. Gong, L. Li, Z. Li, H. Ji, A. Stern, Y. Xia, T. Cao, W. Bao, C. Wang, Y. Wang, Z.Q. Qiu, R.J. Cava, S.G. Louie, J. Xia, X. Zhang, Nature **546**, 265 (2017).

[91] K.S. Burch, D. Mandrus, J.G. Park, Nature **563**, 47 (2018).

[92] B. Shabbir, M. Nadeem, Z. Dai, M.S. Fuhrer, Q.K. Xue, X. Wang, Q. Bao, Appl. Phys. Rev. **5**, 041105 (2018).

[93] M. Gibertini, M. Koperski, A.F. Morpurgo, K.S. Novoselov, Nat. Nanotechnol. **14**, 408 (2019).

[94] C. Gong, X. Zhang, Science **363**, eaav4450 (2019).

[95] H. Li, S. Ruan, Y.J. Zeng, Adv. Mater. **31**, 1900065 (2019).

[96] M.C. Wang, C.C. Huang, C.H. Cheung, C.Y. Chen, S.G. Tan, T.W. Huang, Y. Zhao, Y. Zhao, G. Wu, Y.P. Feng, H.C. Wu, C.R. Chang, Ann. Phys. **532**, 1900452 (2020).

[97] Q.H. Wang, A. Bedoya-Pinto, M. Blei, A.H. Dismukes, A. Hamo, S. Jenkins, M. Koperski, Y. Liu, Q.C. Sun, E.J. Telford, H.H. Kim, M. Augustin, U. Vool, J.X. Yin, L.H. Li, A. Falin, C.R. Dean, F. Casanova, R.F.L. Evans, M. Chshiev, A. Mishchenko, C. Petrovic, R. He, L. Zhao, A.W. Tsen, B.D. Gerardot, M. Brotons-Gisbert, Z. Guguchia, X. Roy, S. Tongay, Z. Wang, M.Z. Hasan, J. Wrachtrup, A. Yacoby, A. Fert, S. Parkin, K.S. Novoselov, P. Dai, L. Balicas, E.J.G. Santos, ACS Nano **16**, 6960 (2022).

[98] S. Bao, W. Wang, Y. Shangguan, Z. Cai, Z.Y. Dong, Z. Huang, W. Si, Z. Ma, R. Kajimoto, K. Ikeuchi, et al., Phys. Rev. X **12**, 011022 (2022).

[99] E. Samuelsen, R. Silberglitt, G. Shirane, J. Remeika, Phys. Rev. B **3**, 157 (1971).

[100] A.R. Wildes, B. Roessli, B. Lebech, K.W. Godfrey, J. Phys. Condens. Matter . **10**, 6417 (1998).

[101] S. Calder, A.I. Kolesnikov, A.F. May, Phys. Rev. B **99**, 094423 (2019).

[102] X. Bai, F. Lechermann, Y. Liu, Y. Cheng, A.I. Kolesnikov, F. Ye, T.J. Williams, S. Chi, T. Hong, G.E. Granroth, A.F. May, S. Calder, Phys. Rev. B **106**, L180409 (2022).

[103] M. Costa, N.M. Peres, J. Fernández-Rossier, A.T. Costa, Phys. Rev. B **102**, 014450 (2020).

[104] T. Yin, K.A. Ulman, S. Liu, A. Granados del Águila, Y. Huang, L. Zhang, M. Serra, D. Sedmidubsky, Z. Sofer, S.Y. Quek, Q. Xiong, Adv. Mater. **33**, 2101618 (2021).

[105] H.L. Zhuang, P. Kent, R.G. Hennig, Phys. Rev. B **93**, 134407 (2016).

[106] L. Webster, J.A. Yan, Phys. Rev. B **98**, 144411 (2018).

[107] I. Khan, J. Hong, Nanotechnology **31**, 195704 (2020).

[108] Y. Wang, C. Wang, S.J. Liang, Z. Ma, K. Xu, X. Liu, L. Zhang, A.S. Admasu, S.W. Cheong, L. Wang, M. Chen, Z. Liu, B. Cheng, W. Ji, F. Miao, Adv. Mater. **32**, 2004533 (2020).

[109] X. Hu, Y. Zhao, X. Shen, A.V. Krasheninnikov, Z. Chen, L. Sun, ACS Appl. Mater. Interfaces **12**, 26367 (2020).

[110] D.L. Esteras, A. Rybakov, A.M. Ruiz, J.J. Baldoví, Nano Lett. **22**, 8771 (2022).

[111] T.H.R. Skyrme, Nucl. Phys. **31**, 556 (1962).

[112] A. Bogdanov, U. Rößler, Phys. Rev. Lett. **87**, 037203 (2001).

[113] J.P. Liu, Z. Zhang, G. Zhao, (CRC Press, 2016).

[114] N. Nagaosa, Y. Tokura, Nat. Nanotechnol. **8**, 899 (2013).

[115] A. Bocdanov, A. Hubert, physica status solidi (b) **186**, 527 (1994).

[116] U.K. Roessler, A. Bogdanov, C. Pfleiderer, Nature **442**, 797 (2006).

[117] A.N. Bogdanov, D. Yablonskii, Zh. Eksp. Teor. Fiz **95**, 178 (1989).

[118] A. Fert, P.M. Levy, Phys. Rev. Lett. **44**, 1538 (1980).

[119] C. Back, V. Cros, H. Ebert, K. Everschor-Sitte, A. Fert, M. Garst, T. Ma, S. Mankovsky, T. Monchesky, M. Mostovoy, et al., J. Phys. D: Appl. Phys. **53**, 363001 (2020).

[120] F. Jonietz, S. Mühlbauer, C. Pfleiderer, A. Neubauer, W. Münzer, A. Bauer, T. Adams, R. Georgii, P. Böni, R.A. Duine, et al., Science **330**, 1648 (2010).

[121] N.S. Kiselev, A. Bogdanov, R. Schäfer, U. Rößler, J. Phys. D: Appl. Phys. **44**, 392001 (2011).

[122] J. Sampaio, V. Cros, S. Rohart, A. Thiaville, A. Fert, Nat. Nanotechnol. **8**, 839 (2013).

[123] A. Fert, N. Reyren, V. Cros, Nat. Rev. Mater. **2**, 1 (2017).

[124] T. Nozaki, Y. Jibiki, M. Goto, E. Tamura, T. Nozaki, H. Kubota, A. Fukushima, S. Yuasa, Y. Suzuki, Appl. Phys. Lett. **114** (2019).

[125] C. Ma, X. Zhang, J. Xia, M. Ezawa, W. Jiang, T. Ono, S. Piramanayagam, A. Morisako, Y. Zhou, X. Liu, Nano Lett. **19**, 353 (2018).

[126] A.C. Hewson, (Cambridge university press, 1997).

[127] L. Zhang, T. Miyamachi, T. Tomanić, R. Dehm, W. Wulfhekel, Rev. Sci. Instrum. **82** (2011).

[128] F. Pobell, vol. 2 (Springer, 2007).

[129] O. Lounasmaa, Journal of Physics E: Scientific Instruments **12**, 668 (1979).

[130] D.S. Betts, (Cambridge University Press, 1989).

[131] T. Balashov, M. Meyer, W. Wulfhekel, Rev. Sci. Instrum. **89** (2018).

[132] H. Ibach, vol. 12 (Springer, 2006).

[133] M. Bonilla, S. Kolekar, Y. Ma, H.C. Diaz, V. Kalappattil, R. Das, T. Eggers, H.R. Gutierrez, M.H. Phan, M. Batzill, Nat. Nanotechnol. **13**, 289 (2018).

[134] P.K.J. Wong, W. Zhang, F. Bussolotti, X. Yin, T.S. Herng, L. Zhang, Y.L. Huang, G. Vinai, S. Krishnamurthi, D.W. Bukhvalov, et al., Adv. Mater. **31**, 1901185 (2019).

[135] G. Chen, S.T. Howard, A.B. Maghirang III, K.N. Cong, R.A.B. Villaos, L.Y. Feng, K. Cai, S.C. Ganguli, W. Swiech, E. Morosan, et al., Phys. Rev. B **102**, 115149 (2020).

[136] J. Feng, D. Biswas, A. Rajan, M.D. Watson, F. Mazzola, O.J. Clark, K. Underwood, I. Markovic, M. McLaren, A. Hunter, et al., Nano Lett. **18**, 4493 (2018).

[137] W. Zhang, L. Zhang, P.K.J. Wong, J. Yuan, G. Vinai, P. Torelli, G. van der Laan, Y.P. Feng, A.T. Wee, ACS nano **13**, 8997 (2019).

[138] K. Zakeri, D. Rau, J. Jandke, F. Yang, W. Wulfhekel, C. Berthod, ACS nano **17**, 9575 (2023).

[139] J. Jandke, F. Yang, P. Hlobil, T. Engelhardt, D. Rau, K. Zakeri, C. Gao, J. Schmalian, W. Wulfhekel, Phys. Rev. B **100**, 020503 (2019).

[140] S. Jiang, L. Li, Z. Wang, K.F. Mak, J. Shan, Nat. Nanotechnol. **13**, 549 (2018).

[141] Y. Deng, Y. Yu, Y. Song, J. Zhang, N.Z. Wang, Z. Sun, Y. Yi, Y.Z. Wu, S. Wu, J. Zhu, J. Wang, X.H. Chen, Y. Zhang, Nature **563**, 94 (2018).

[142] Z. Fei, B. Huang, P. Malinowski, W. Wang, T. Song, J. Sanchez, W. Yao, D. Xiao, X. Zhu, A.F. May, et al., Nat. Mater. **17**, 778 (2018).

[143] K. Kim, J. Seo, E. Lee, K.T. Ko, B.S. Kim, B.G. Jang, J.M. Ok, J. Lee, Y.J. Jo, W. Kang, J.H. Shim, C. Kim, H.W. Yeom, B. Il Min, B.J. Yang, J.S. Kim, Nat. Mater. **17**, 794 (2018).

[144] G.D. Nguyen, J. Lee, T. Berlijn, Q. Zou, S.M. Hus, J. Park, Z. Gai, C. Lee, A.P. Li, Phys. Rev. B **97**, 014425 (2018).

[145] B. Ding, Z. Li, G. Xu, H. Li, Z. Hou, E. Liu, X. Xi, F. Xu, Y. Yao, W. Wang, Nano Lett. **20**, 868 (2019).

[146] H.J. Deiseroth, K. Aleksandrov, C. Reiner, L. Kienle, R.K. Kremer, Eur. J. Inorg. Chem. **2006**, 1561 (2006).

[147] B. Chen, J. Yang, H. Wang, M. Imai, H. Ohta, C. Michioka, K. Yoshimura, M. Fang, J. Phys. Soc. Japan **82**, 124711 (2013).

[148] A. Hubert, R. Schäfer, (Springer, 2000).

[149] J.M. Coey, (Cambridge university press, 2010).

[150] H.J. Deiseroth, K. Aleksandrov, C. Reiner, L. Kienle, R.K. Kremer (2006).

[151] J.X. Zhu, M. Janoschek, D. Chaves, J. Cezar, T. Durakiewicz, F. Ronning, Y. Sassa, M. Mansson, B. Scott, N. Wakeham, et al., Phys. Rev. B **93**, 144404 (2016).

[152] K. Kim, J. Seo, E. Lee, K.T. Ko, B. Kim, B.G. Jang, J.M. Ok, J. Lee, Y.J. Jo, W. Kang, et al., Nat. Mater. **17**, 794 (2018).

[153] Y. Wang, C. Xian, J. Wang, B. Liu, L. Ling, L. Zhang, L. Cao, Z. Qu, Y. Xiong, Phys. Rev. B **96**, 134428 (2017).

[154] N. León-Brito, E.D. Bauer, F. Ronning, J.D. Thompson, R. Movshovich, J. Appl. Phys. **120**, 083903 (2016).

[155] J. Yi, H. Zhuang, Q. Zou, Z. Wu, G. Cao, S. Tang, S. Calder, P. Kent, D. Mandrus, Z. Gai, 2D Materials **4**, 011005 (2016).

[156] T.E. Park, L. Peng, J. Liang, A. Hallal, F.S. Yasin, X. Zhang, K.M. Song, S.J. Kim, K. Kim, M. Weigand, et al., Phys. Rev. B **103**, 104410 (2021).

[157] H. Wang, C. Wang, Z.A. Li, H. Tian, Y. Shi, H. Yang, J. Li, Appl. Phys. Lett. **116** (2020).

[158] M.J. Meijer, J. Lucassen, R.A. Duine, H.J. Swagten, B. Koopmans, R. Lavrijsen, M.H. Guimarães, Nano Lett. **20**, 8563 (2020).

[159] Y. Wu, S. Zhang, J. Zhang, W. Wang, Y.L. Zhu, J. Hu, G. Yin, K. Wong, C. Fang, C. Wan, et al., Nat. commun. **11**, 3860 (2020).

[160] I. Horcas, R. Fernández, J.M. Gómez-Rodríguez, J. Colchero, J. Gómez-Herrero, A.M. Baro, Rev. Sci. Instrum. **78**, 13705 (2007).

[161] J.M. Kim, C. Cho, E.Y. Hsieh, S. Nam, J. Mater. Res. **35**, 1369 (2020).

[162] B. Deng, Z. Pang, S. Chen, X. Li, C. Meng, J. Li, M. Liu, J. Wu, Y. Qi, W. Dang, et al., ACS nano **11**, 12337 (2017).

[163] J. Mao, S.P. Milovanović, M. Anđelković, X. Lai, Y. Cao, K. Watanabe, T. Taniguchi, L. Covaci, F.M. Peeters, A.K. Geim, et al., Nature **584**, 215 (2020).

[164] J.W. Jiang, Acta Mechanica Solida Sinica **32**, 17 (2019).

[165] S. Zhu, H.T. Johnson, Nanoscale **10**, 20689 (2018).

[166] J.R. Jain, A. Hryciw, T.M. Baer, D.A. Miller, M.L. Brongersma, R.T. Howe, Nat. Photonics **6**, 398 (2012).

[167] A. High, J. Leonard, M. Remeika, L. Butov, M. Hanson, A. Gossard, Nano Lett. **12**, 2605 (2012).

[168] A. Castellanos-Gomez, R. Roldán, E. Cappelluti, M. Buscema, F. Guinea, H.S. Van Der Zant, G.A. Steele, Nano Lett. **13**, 5361 (2013).

[169] J.S. Moodera, J. Nowak, R.J.M. van de Veerdonk, Phys. Rev. Lett. **80**, 2941 (1998).

[170] A. Wachowiak, J. Wiebe, M. Bode, O. Pietzsch, M. Morgenstern, R. Wiesendanger, Science **298**, 577 (2002).

[171] M. Julliere, Phys. Lett. **54A**, 225 (1975).

[172] R. Wiesendanger, Rev. Mod. Phys. **81**, 1495 (2009).

[173] W. Wulfhekel, J. Kirschner, Annu. Rev. Mater. Res. **37**, 69 (2007).

[174] M. Menzel, Y. Mokrousov, R. Wieser, E. Jessica, E. Vedmedenko, S. Bl, S. Heinze, J.E. Bickel, E. Vedmedenko, S. Blu, R. Wiesendanger, S. Heinze, K.V. Bergmann, Phys. Rev. Lett. **108**, 197204 (2012).

[175] M. Zhu, Y. You, G. Xu, J. Tang, Y. Gong, F. Xu, Intermetallics **131**, 107085 (2021).

[176] M.R. Scheinfein, J. Unguris, J.L. Blue, K.J. Coakley, D.T. Pierce, R.J. Celotta, P.J. Ryan, Phys. Rev. B **43**, 3395 (1991).

[177] U. Schlickum, W. Wulfhekel, J. Kirschner, Appl. Phys. Lett. **83**, 2016 (2003).

[178] (2012). In SpringerMaterials (https://materials.springer.com/isp/crystallographic/docs/sd_1420956).

[179] The JuKKR developers (2021). Https://jukkr.fz-juelich.de.

[180] H. Ebert, D. Ködderitzsch, J. Minár, Rep. Prog. Phys. **74**, 096501 (2011).

[181] N. Stefanou, H. Akai, R. Zeller, Comput. Phys. Commun. **60**, 231 (1990).

[182] N. Stefanou, R. Zeller, J. Condens. Matter Phys. **3**, 7599 (1991).

[183] S.H. Vosko, L. Wilk, M. Nusair, Can. J. Phys. **58**, 1200 (1980).

[184] J.P. Perdew, K. Burke, M. Ernzerhof, Phys. Rev. Lett. **77**, 3865 (1996).

[185] A. Liechtenstein, M. Katsnelson, V. Antropov, V. Gubanov, J. Magn. Magn. Mater. **67**, 65 (1987).

[186] L. Udvardi, L. Szunyogh, K. Palotás, P. Weinberger, Phys. Rev. B **68**, 104436 (2003).

[187] A.F. May, S. Calder, C. Cantoni, H. Cao, M.A. McGuire, Phys. Rev. B **93**, 014411 (2016).

[188] B. Chen, J. Yang, H. Wang, M. Imai, H. Ohta, C. Michioka, K. Yoshimura, M. Fang, J. Phys. Soc. Japan. **82**, 124711 (2013).

[189] B. Schweflinghaus, B. Zimmermann, M. Heide, G. Bihlmayer, S. Blügel, Phys. Rev. B **94**, 024403 (2016).

[190] J. Macy, D. Ratkovski, P.P. Balakrishnan, M. Strungaru, Y.C. Chiu, A. Flessa Savvidou, A. Moon, W. Zheng, A. Weiland, G.T. McCandless, et al., Appl. Phys. Rev. **8** (2021).

[191] B. Ding, X. Li, Z. Li, X. Xi, Y. Yao, W. Wang, NPG Asia Mater. **14**, 74 (2022).

[192] S. Laref, K.W. Kim, A. Manchon, Phys. Rev. B **102**, 060402 (2020).

[193] S. Yin, L. Zhao, C. Song, Y. Huang, Y. Gu, R. Chen, W. Zhu, Y. Sun, W. Jiang, X. Zhang, et al., Chinese Physics B **30**, 027505 (2021).

[194] L. Cai, C. Yu, L. Liu, W. Xia, H.A. Zhou, L. Zhao, Y. Dong, T. Xu, Z. Wang, Y. Guo, et al., Appl. Phys. Lett. **117** (2020).

[195] M.G. Han, J.A. Garlow, Y. Liu, H. Zhang, J. Li, D. DiMarzio, M.W. Knight, C. Petrovic, D. Jariwala, Y. Zhu, Nano Lett. **19**, 7859 (2019).

[196] N. Romming, A. Kubetzka, C. Hanneken, K. von Bergmann, R. Wiesendanger, Phys. Rev. Lett. **114**, 177203 (2015).

[197] S. Rohart, J. Miltat, A. Thiaville, Phys. Rev. B **93**, 214412 (2016).

[198] A. Bernand-Mantel, L. Camosi, A. Wartelle, N. Rougemaille, M. Darques, L. Ranno, SciPost Phys. **4**, 027 (2018).

[199] A.N. Bogdanov, A. Hubert, J. Magn. Magn. Mater. **138**, 255 (1994).

[200] M.N. Wilson, A.B. Butenko, A.N. Bogdanov, T.L. Monchesky, Phys. Rev. B **89**, 094411 (2014).

[201] A. Leonov, T.L. Monchesky, N. Romming, A. Kubetzka, A.N. Bogdanov, R. Wiesendanger, New J. Phys. **18**, 065003 (2016).

[202] L. Mougel, P.M. Buhl, R. Nemoto, T. Balashov, M. Hervé, J. Skolaut, T.K. Yamada, B. Dupé, W. Wulfhekel, Appl. Phys. Lett. **116**, 262406 (2020).

[203] H.H. Yang, N. Bansal, P. Rüßmann, M. Hoffmann, L. Zhang, D. Go, Q. Li, A.A. Haghighirad, K. Sen, S. Blügel, et al., 2D Mater. **9**, 025022 (2022).

[204] Y. Zhang, H. Lu, X. Zhu, S. Tan, W. Feng, Q. Liu, W. Zhang, Q. Chen, Y. Liu, X. Luo, et al., Sci. Adv. **4**, eaao6791 (2018).

[205] C. Trainer, O.R. Armitage, H. Lane, L.C. Rhodes, E. Chan, I. Benedičič, J.A. Rodriguez-Rivera, O. Fabelo, C. Stock, P. Wahl, Phys. Rev. B **106**, L081405 (2022).

[206] L. Du, J. Tang, Y. Zhao, X. Li, R. Yang, X. Hu, X. Bai, X. Wang, K. Watanabe, T. Taniguchi, D. Shi, G. Yu, X. Bai, T. Hasan, G. Zhang, Z. Sun, Adv. Funct. Mater. **29**, 1904734 (2019).

[207] X. Kong, T. Berlijn, L. Liang, Adv. Electron. Mater. **7**, 2001159 (2021).

[208] Q. Cai, Y. Zhang, D. Luong, C.A. Tulk, B.P.T. Fokwa, C. Li, Advanced Physics Research p. 2200089 (2023).

[209] J. Jandke, P. Hlobil, M. Schackert, W. Wulfhekel, J. Schmalian, Phys. Rev. B **93**, 060505 (2016).

[210] T. Balashov, A. Takács, W. Wulfhekel, J. Kirschner, Phys. Rev. Lett. **97**, 187201 (2006).

[211] T. Balashov, A. Takács, M. Däne, A. Ernst, P. Bruno, W. Wulfhekel, Phys. Rev. B **78**, 174404 (2008).

[212] T. Balashov, P. Buczek, L. Sandratskii, A. Ernst, W. Wulfhekel, J. Phys. Condens. Matter. **26**, 394007 (2014).

[213] A. Spinelli, B. Bryant, F. Delgado, J. Fernández-Rossier, A.F. Otte, Nat. Mater. **13**, 782 (2014).

[214] A. Kubetzka, M. Bode, O. Pietzsch, R. Wiesendanger, Phys. Rev. Lett. **88**, 057201 (2002).

[215] S. Zhang, P.M. Levy, A.C. Marley, S.S.P. Parkin, Phys. Rev. Lett. **79**, 3744 (1997).

[216] S. Bao, W. Wang, Y. Shangguan, Z. Cai, Z.Y. Dong, Z. Huang, W. Si, Z. Ma, R. Kajimoto, K. Ikeuchi, S.i. Yano, S.L. Yu, X. Wan, J.X. Li, J. Wen, Phys. Rev. X **12**, 011022 (2022).

[217] R.D. McMichael, A. Kunz, J. Appl. Phys. **91**, 8650 (2002).

[218] C.R. Ast, B. Jäck, J. Senkpiel, M. Eltschka, M. Etzkorn, J. Ankerhold, K. Kern, Nat. Commun. **7**, 13009 (2016).

[219] J. Senkpiel, J.C. Klockner, M. Etzkorn, S. Dambach, B. Kubala, W. Belzig, A.L. Yeyati, J.C. Cuevas, F. Pauly, J. Ankerhold, C.R. Ast, K. Kern, Phys. Rev. Lett. **124**, 156803 (2020).

[220] T. Esat, M. Ternes, R. Temirov, F.S. Tautz, Phys. Rev. Res. **5**, 033200 (2023).

Publications

Published (Included in thesis)

1. Hung-Hsiang Yang, Namrata Bansal[1], Philipp Rüßmann, Markus Hoffmann, Lichuan Zhang, Dongwook Go, Qili Li, Amir-Abbas Haghighirad, Kaushik Sen, Stefan Blügel, Matthieu Le Tacon, Yuriy Mokrousov and Wulf Wulfhekel. *"Magnetic domain walls of the van der Waals material Fe_3GeTe_2"*, **2D Mater. 9 025022 (2022)**

Submitted to arXiv

1. Namrata Bansal, Qili Li[2], Paul Nufer, Lichuan Zhang, Amir-Abbas Haghighirad, Yuriy Mokrousov and Wulf Wulfhekel. *"Magnon-Phonon coupling in Fe_3GeTe_2"*, **arXiv:2308.10774 (2023)**

Conferences contributions

A. Oral presentations

1. "*Probing magnetic domains in two dimensional Fe_3GeTe_2 using spin-polarized scanning tunneling microscopy*",
   Namrata Bansal, Hung-Hsiang Yang, Philipp Rüßmann, Markus Hoffmann, Lichuan Zhang, Dongwook Go, Qili Li, Amir-Abbas Haghighirad, Kaushik Sen, Stefan Blügel, Matthieu Le Tacon, Yuriy Mokrousov and Wulf Wulfhekel.
   Novel 2D materials explored via scanning probe microscopy and spectroscopy (2D SPM conference). June 20^{th}-24^{th}, 2022. Donostia/San Sebastián, Spain

2. "*Magnetic domains in Fe_3GeTe_2 detected with spin polarized STM*",,
   Namrata Bansal, Hung-Hsiang Yang, Philipp Rüßmann, Markus Hoffmann, Lichuan Zhang,

Dongwook Go, Qili Li, Amir-Abbas Haghighirad, Kaushik Sen, Stefan Blügel, Matthieu Le Tacon, Yuriy Mokrousov and Wulf Wulfhekel.
Solitons and Skyrmion Magnetism (Sol-skymag 2022) conference, 27th June-1st July 2022, Donostia/San Sebastián, Spain

3. "*Spin-polarized scanning tunneling microscopy for investigating magnetic domains of Fe_3GeTe_2*", Namrata Bansal, Hung-Hsiang Yang, Philipp Rüßmann, Markus Hoffmann, Lichuan Zhang, Dongwook Go, Qili Li, Amir-Abbas Haghighirad, Kaushik Sen, Stefan Blügel, Matthieu Le Tacon, Yuriy Mokrousov and Wulf Wulfhekel.
24th International Colloquium on Magnetic Films and Surfaces (ICMFS-2022), July 10th-15th, 2022, Okinawa, Japan (hybrid mode)

4. "*Detection of magnetic domains in two dimensional Fe_3GeTe_2 using spin-polarized scanning tunneling microscopy*",
Namrata Bansal, Hung-Hsiang Yang, Philipp Rüßmann, Markus Hoffmann, Lichuan Zhang, Dongwook Go, Qili Li, Amir-Abbas Haghighirad, Kaushik Sen, Stefan Blügel, Matthieu Le Tacon, Yuriy Mokrousov and Wulf Wulfhekel.
2022 Joint European Magnetic Symposia (JEMS 2022). 24th-29th July, 2022, Warshaw, Poland (hybrid mode)

5. "*Investigation of magnetic domains of Fe_3GeTe_2 by out-of-plane spin-polarized scanning tunneling microscopy*",
Namrata Bansal, Hung-Hsiang Yang, Philipp Rüßmann, Markus Hoffmann, Lichuan Zhang, Dongwook Go, Qili Li, Amir-Abbas Haghighirad, Kaushik Sen, Stefan Blügel, Matthieu Le Tacon, Yuriy Mokrousov and Wulf Wulfhekel.
DPG-Frühjahrstagung (DPG Spring) Meeting 2022. Regensberg, Germany

6. "*Investigation of magnon-phonon coupling in two dimensional ferromagnetic Fe_3GeTe_2*",
Namrata Bansal, Qili Li, Paul Nufer, Lichuan Zhang, Amir-Abbas Haghighirad, Yuriy Mokrousov and Wulf Wulfhekel.
DPG-Frühjahrstagung (DPG Spring) Meeting 2023. Dresden, Germany

7. "*Unveiling magnon-phonon coupling in two-dimensional ferromagnetic Fe_3GeTe_2*",
Namrata Bansal, Qili Li, Paul Nufer, Lichuan Zhang, Amir-Abbas Haghighirad, Yuriy Mokrousov and Wulf Wulfhekel.
International Conference on Magnetic Materials and Applications (ICMAGMA-2023), 4th-6th December, 2023, Hyderabad, India

8. "*Unraveling the magnon-phonon hybridization in Fe_3GeTe_2*",
   Namrata Bansal, Qili Li, Paul Nufer, Lichuan Zhang, Amir-Abbas Haghighirad, Yuriy Mokrousov and Wulf Wulfhekel.
   DPG-Frühjahrstagung (DPG Spring) Meeting 2024. Berlin, Germany

B. Poster presentations

1. "*Investigating magnetic domains of Fe_3GeTe_2 by spin-polarized scanning tunneling microscopy*",
   Namrata Bansal, Hung-Hsiang Yang and Wulf Wulfhekel.
   MSCA QUSTEC EUCOR Summer School 2021. September 14^{th}-17^{th}, 2021, Engelberg, Switzerland

2. "*Observation of magnetic skyrmions in bulk Fe_3GeTe_2 by spin-polarized scanning tunneling microscopy*",
   Namrata Bansal, Hung-Hsiang Yang, Philipp Rüßmann, Markus Hoffmann, Lichuan Zhang, Dongwook Go, Qili Li, Amir-Abbas Haghighirad, Kaushik Sen, Stefan Blügel, Matthieu Le Tacon, Yuriy Mokrousov and Wulf Wulfhekel.
   2022 European School on Magnetism. September 11^{th}-23^{th}, 2022, Saarbrücken, Germany

3. Best Poster Award "*Observation of magnon-phonon coupling in two dimensional ferromagnetic Fe_3GeTe_2*",
   Namrata Bansal, Qili Li, Paul Nufer, Lichuan Zhang, Amir-Abbas Haghighirad, Yuriy Mokrousov and Wulf Wulfhekel.
   68th Annual Conference on Magnetism and Magnetic Materials (MMM 2023), October 30^{th}-November 4^{th}, 2023, Dallas, Texas, USA

Acknowledgements

I am immensely grateful for the enriching experience that my PhD journey has been, marking one of the most cherishing periods of my academic career. Undertaking my doctoral studies in Germany, has not only allowed me to delve into the knowledge of Physics but also provided me with invaluable insights into life as an international student. It has been a journey of discovery, where I have had the privilege of immersing myself in a diverse cultural values and advancing meaningful connections. Throughout this journey, I have had the pleasure of crossing paths with numerous remarkable individuals whose guidance, support, and generosity have been essential in shaping my academic and personal growth. Their presence has made this journey truly memorable and rewarding. I extend my heartfelt gratitude to everyone who has contributed to making this experience not only easier but also incredibly fulfilling.

First and foremost, I extend my deepest gratitude to **Prof. Dr. Wulf Wulfhekel**, whose guidance and mentorship have been invaluable throughout my journey. His profound knowledge, discipline, and genuine compassion have made him not just a supervisor, but a source of inspiration and support. His dedication to his students and colleagues, coupled with his boundless kindness and respect, have created a nurturing environment where growth and learning flourish. I am highly grateful for his support and encouragement, which extends beyond the limit of academia to every aspect of life. His willingness for being a helping hand, even in the face of personal challenges, describes a lot about his generosity of kind heart. Moreover, his remarkable ability to balance professional responsibilities with his passion for astronomy and his love for maintaining his beautiful garden is truly admirable. From the moment I joined his group, he has gone above and beyond to make me feel welcomed and cared for, particularly knowing that I am far from my family. His paternal nature and genuine concern for the well-being of his students have created a sense of belonging that I cherish deeply. I am profoundly grateful for his fatherly guidance and constant support, which have made my PhD journey not only fulfilling but also immensely enriching. In Prof. Wulfhekel, I have found not just a supervisor, but a role model, whose integrity, compassion, and dedication serve as a constant source of inspiration. I am truly blessed and honored to have him as a father-like supervisor in my life.

I extend my heartfelt gratitude to **Prof. Dr. Markus Garst** for graciously agreeing to be my PhD mentor. His constant support and guidance throughout my doctoral journey have been invaluable. I deeply appreciate his respectful behaviour and kindness during our meetings, where his theoretical insights greatly helpful to understand our experimental work. It is an honor to learn from his expertise in the field, and I am sincerely thankful for his mentorship to my academic development.

I extend my sincere gratitude to our esteemed theory collaborator team, under the leadership of **Prof. Dr. Yuriy Makrousov**, for their invaluable contributions in executing DFT calculations and providing exceptional support with theoretical insights. I would like to offer special thanks to **Dr. Lichaun Zhang, Dr. Philipp Rüssmann, Markus Hoffmann, Dr. Dongwook Go**, and **Prof. Dr. Stefan Blügel**. Their expertise and dedication have been instrumental in our understanding of the experimental results, emphasizing the critical role of DFT calculations and related theoretical analyses in our research endeavors.

I extend my sincere gratitude to the crystal grower team, under the guidance of **Prof. Dr. Matthieu Le Tacon**, for their invaluable contributions to this work. I am grateful to **Dr. Amir-Abbas Haghighirad** for his outstanding efforts in providing us with high-quality FGT crystals and for his enthusiastic engagement during our discussions. Additionally, I would like to acknowledge **Dr. Kaushik Sen** for the execution of various magnetic measurements, which have greatly facilitated our experiments.

I would like to extend my heartfelt appreciation to **Dr. Hung-Hsiang Yang** for his exceptional mentorship and guidance throughout my learning journey with the STM setup. As a newcomer with limited knowledge of STM, I was fortunate to have him patiently imparting his expertise, explaining every minute detail of the measurements with care and diligence. His nurturing behaviour not only earned him respect but also encouraged a positive and conducive atmosphere in the lab. His mentorship has been invaluable, and I am sincerely grateful for his support.

I extend my heartfelt gratitude to **Dr. Qili Li** for his invaluable guidance and support. His wealth of knowledge coupled with his humble and gracious behaviour has made him an invaluable mentor. Throughout our experiments, I have learned immensely from his expertise and insightful advice. His kindness and willingness to assist have been truly commendable. Additionally, I cherish the wonderful times we shared as neighbors at KIT's guest house, where I had the pleasure of meeting his lovely wife. Their warm hospitality added to the richness of my experience, and I am truly grateful for their support.

I extend my gratitude to the **ELASTO-Q-MAT SFB TRR288**, the **Deutsche Forschungsgemeinschaft** (DFG, German Research Foundation), and **KIT** for their financial support during my PhD journey.

I extend my sincere appreciation to **Mr. Michael Meyer** and the entire mechanical workshop team for their constant support and assistance. Mr. Meyer's genuine and respectful nature, coupled with the team's willingness to help under any circumstance, has been invaluable to me.

I would also like to express my gratitude to **Mr. Jannis Ret** and the electronics workshop team for their invaluable assistance during our experiments. Their expertise and willingness to help have been invaluable. I would like to thank **Mr. Michael Pfirrmann** for his organised assistance at the helium station.

I extend my heartfelt gratitude to **Mrs. Claudia Alaya** for her exceptional organizational skills and her assistance with administrative tasks. Her helpful and kind behaviour, coupled with her cheerful nature, has made working with her a pleasure. Beyond our professional interactions, I am grateful for her friendship, and I cherish the moments we spend together. I extend my gratitude to **Mrs. Steffi Baatz** for her outstanding assistance in administration. Her kindness and willingness to help, making her an invaluable asset to our team.

I extend my heartfelt appreciation to all my lab members for creating a warm and supportive environment throughout my research journey. Special thanks to **Anika**, whose assistance in securing accommodation during the early stages of my PhD was invaluable. I am grateful to both past and present members for their continuous support and for maintaining a joyful atmosphere in the lab. This includes **Vera, Qili, Hongyan, Soroush, Charanpreet, Lukas, Simon, Luisa, Michael, Thomas, Hung-Hsiang, Paul, Qing, Loïc, Timo, Lei, Vibhuti, Julian, Philip, Mirjam, Gabriel, Adrian, Jacob, Marie, Nola, Miyako, Eugenio, Hiroki, Haruto** and **Haoran**. Thank you everyone for giving me unforgettable memories.

I am grateful to my students whom I had the privilege to assist during practical sessions. It was a rewarding experience to engage in discussions with them and provide guidance during their measurements. I extend my appreciation to the organizers of the practical sessions, led by **Dr. Christoph Sürgers** and **Mrs. Carmen Huck**. I thank to **Mrs. Kornelia Hugle** for conducting safety briefings for the MAX-praktikum users. Additionally, I would like to express my gratitude to **Aljoscha Auer** for his kind guidance and support when I used the setup for the first time.

I am deeply grateful to my dear friend **Rishita Patel**, who has been a pillar of support and a source of strength since the day we met. Our bond goes beyond friendship; she is like a sister to me. Her unwavering support, kindness, and understanding have been invaluable to me throughout our journey together. I am grateful to my friend **Himanshu** for his constant support and encouragement throughout my PhD journey. I extend my heartfelt thanks to my friends: **Kurnika, Harshita, Riya, Deeksha, Akash, Rohit, Karthikeyan, Lukas, Ashwini, Annapoorna, Shraddha, Nirmala, Vera,** and **Saheli**. Their friendship has been a constant source of joy and support, and I am truly grateful for their presence in my life. I would like to express my gratitude to my **Salsa class**

friends, whose companionship have enriched my experience in Karlsruhe. I extend my gratitude to **all the friends I made during the conferences and summer schools** I attended throughout my PhD journey. Their friendship has added a special dimension to my memories.

I express my heartfelt gratitude to my extended family like friends whom I had the pleasure of meeting in Karlsruhe. **Jyoti, Dillip, Rajesh, Smriti, Kiran, Gaurav, Ankit, Pranav, Khushboo and Neha** along with their adorable kids **Aarnav, Ziya, Prisha** and **Aahana**, have brought immense joy into my life. The memories we've created together hold a special place in my heart, and their unwavering support has been invaluable throughout my Ph.D. journey. I am truly blessed to have them by my side, and I will forever cherish the moments we've shared.

I extend my heartfelt gratitude to **my family members**, including uncles, aunts, especially **Mukesh Gupta** and **Preeti Gupta**, as well as my cousins, for their blessings and support throughout my journey.

I express my sincere appreciation to the advancements in technology, particularly the availability of video calling facilities, which played a pivotal role in keeping me connected with my friends and family members.

I am deeply grateful to my late brother, **Apoorv Bansal**, whose unwavering support continues to inspire me even after his passing during my Bachelors. His memory serves as a constant source of strength and encouragement in my life journey. Additionally, I would like to express my heartfelt gratitude to my beloved grandmother, **Mrs. Birma Gupta**, who I lost during my second year of PhD. Her enduring love, care, and guidance have always been a beacon of light for me. I carry her lessons and blessings with me, cherishing them as invaluable treasures in my heart.

Finally, I extend my heartfelt gratitude to two of the most significant individuals in my life: my mother, **Madhu Gupta**, and my father, **Raj Kumar Bansal**. Their constant support, boundless love, and enduring encouragement have been pillars of strength throughout my PhD journey. Their blessings have been instrumental in my achievements, and I am deeply grateful for their presence in my life.